

**Complex structures, disorder and low dimensionality -
Treatment of oxides and semiconductors by a relativistic
Korringa-Kohn-Rostoker Green function method**

Dissertation

zur Erlangung des Doktorgrades der Naturwissenschaften
(Dr. rer. nat.)

der

Naturwissenschaftlichen Fakultät II
Chemie, Physik und Mathematik

der Martin-Luther-Universität
Halle-Wittenberg

vorgelegt von

Richard Matthias Geilhufe, M.Sc.
geboren am 15.11.1986, in Halle (Saale)

Tag der Verteidigung
17. Dezember 2015

Gutachter:

- 1 PD Dr. Arthur Ernst, Max-Planck-Institut für Mikrostrukturphysik
- 2 Prof. Dr. Steffen Trimper, Martin-Luther-Universität Halle-Wittenberg
- 3 Prof. Dr. László Szunyogh, Budapesti Műszaki és Gazdaságtudományi Egyetem

Abstract: The thesis describes the implementation of the fully-relativistic KORRINGA-KOHN-ROSTOKER GREEN function method within the full-potential approximation. In contrast to previous implementations the single-site scattering problem is obtained by a direct solution of a system of ordinary differential equations. The choice of this approach is motivated from an extensive numerical investigation of the problem. Furthermore, the relativistic KKR method is used to investigate the tuning of band inversion in $\text{Pb}_x\text{Sn}_{1-x}\text{Te}$ alloys. Additionally, a scalar relativistic approximation was applied to study the low temperature magnetostructure of PrMnO_3 and CaMnO_3 . With the help of the *Mathematica* group theory package *GTPack* single Ho atoms on a Pt(111) surface are investigated within the framework of crystal field theory.

Zusammenfassung: Diese Arbeit beschreibt die Implementierung einer vollrelativistischen KORRINGA-KOHN-ROSTOKER-GREEN-Funktionsmethode in der Näherung des vollen Zellpotentials. Im Unterschied zu vorhergehenden Implementierungen wird die Lösung des Einzelstreuproblems auf direktem Wege, durch Lösen eines Systems gewöhnlicher Differentialgleichungen gewonnen. Die Wahl dieses Ansatzes wird durch intensive numerische Untersuchungen motiviert. Des weiteren wird die relativistische KKR methode verwendet, um das Anpassen der Bandinversion in $\text{Pb}_x\text{Sn}_{1-x}\text{Te}$ -Legierungen zu untersuchen. Zusätzlich wird eine skalarrelativistische Variante verwendet um die magnetische Struktur von PrMnO_3 und CaMnO_3 bei niedrigen Temperaturen zu erforschen. Mit Hilfe des *Mathematica* Gruppentheorie-Pakets *GTPack* werden einzelne Ho Atome auf einer Pt (111) Oberfläche im Rahmen der Kristallfeldtheorie untersucht.

Contents

Symbols	V
1. Introduction	1
I. Application of non-relativistic methods to complex materials	5
2. The non-relativistic Korringa-Kohn-Rostoker Green function method	7
2.1. The main formalism in a nutshell	7
2.2. The treatment of disorder using the coherent potential approximation	12
2.3. The HEISENBERG Hamiltonian and the magnetic force theorem	13
3. Ab-initio investigation of PrMnO₃ and CaMnO₃	15
3.1. Why study manganites?	15
3.2. Structure of PrMnO ₃ and CaMnO ₃	17
3.3. Computational methods	18
3.4. Electronic structure	19
3.5. Magnetic structure	22
4. Application of group theoretical methods to magnetic states of Ho on Pt(111)	25
4.1. Introduction	25
4.2. Qualitative discussion	26
4.3. Quantitative discussion	27
4.3.1. Crystal field Hamiltonian	27
4.3.2. Solution of the eigenvalue equation	28
II. Relativistic extension of the Korringa-Kohn-Rostoker Green function method	33
5. Dirac equation and Green function	35
5.1. DIRAC equation	35
5.2. GREEN function	37

5.3. Relativistic free space Green function	37
5.4. The Dyson and Lippmann-Schwinger equation	38
6. Relativistic scattering theory	41
6.1. Introduction	41
6.2. The radial DIRAC equation for an arbitrary single-site scattering potential	42
6.3. Treatment of the non-spherical potential	44
6.3.1. Shape-truncation function	44
6.3.2. The potential matrix	46
6.4. Solution of the free DIRAC equation and matching conditions	48
6.5. Numerical solution of the single-site scattering problem	50
6.5.1. Transformation of the differential equations	52
6.5.2. Initial conditions for the regular scattering solution	53
6.5.3. Normalization of regular scattering solutions and single-site t-matrix	55
6.6. Initial conditions for the irregular scattering solution	57
6.7. Implementation	57
6.8. Left-hand side solution	58
6.9. Multiple scattering Green Function	60
6.10. The LLOYD equation	61
III. Tests of the relativistic extension	63
7. The relativistic Coulomb problem	65
7.1. Introduction	65
7.2. Asymptotic behaviour	66
7.3. Exact solution	69
7.4. Numerical accuracy	72
8. The relativistic Mathieu problem	77
8.1. Introduction	77
8.2. Expansion of the MATHIEU potential into spherical harmonics	78
8.3. Numerical accuracy	79
8.4. Band structure	82
9. The electronic structure of PbTe and SnTe	85
9.1. Introduction	85
9.2. Crystal structure	85
9.3. Computational methods	86

9.4. Electronic structure	86
9.5. Influence of alloying and hydrostatic pressure on band inversion	88
9.6. Influence of uniaxial strain on band inversion	90
10. Summary	93
IV. Appendix	95
A. Density functional theory	97
B. The Mathematica package GTPack	101
Theses and publications	105
Bibliography	107
Acknowledgements	125
Eidesstattliche Erklärung / Declaration under oath	127
Curriculum vitae	129

Symbols

The following mathematical symbols are used throughout the text.

$\tilde{A}, \tilde{B}, \dots$	matrices
\hat{A}, \hat{B}, \dots	operators
$\mathbf{a}, \mathbf{b}, \dots$	vectors
$\mathcal{A}, \mathcal{B}, \dots$	sets
i	imaginary unit, $i^2 = -1$
$\hat{\mathbf{r}}$	represents the azimuthal angle ϑ and the polar angle φ of the vector $\mathbf{r} = (r, \vartheta, \varphi)$
$\Re A$	real part of A
$\Im A$	imaginary part of A
$\text{Tr } \tilde{A} = \sum_i A_{ii}$	denotes the trace of the matrix \tilde{A}

1. Introduction

The KORRINGA-KOHN-ROSTOKER GREEN function method which is applied to calculate material properties in the solid state has had a long tradition going back to the early work of KORRINGA [1] as well as KOHN and ROSTOKER [2] in 1947 and 1954, respectively. The technological demand for functional materials as well as the description of new physical effects during the past decades offered challenging problems and lead to still ongoing extensions of the original band structure method [3]. Two very prominent extensions are: first, the inclusion of spin-orbit coupling, achieved by solving the DIRAC equation instead of the SCHRÖDINGER equation [4, 5, 6] and, second, the consideration of the non-spherical part of the crystal field and the shape of the WIGNER-SEITZ cell at each atomic position, which is denoted as the full-potential approach within the literature [7, 8].

The discussion of spin-orbit coupling in semiconductor physics has a long tradition [9, 10]. However, especially on surfaces spin-orbit coupling driven effects gave new perspectives to solid-state physics during the past 20 years. Examples are the investigation of the RASHBA-splitting on metallic surfaces [11, 12] and the description of topological insulators [13, 14, 15, 16]. Spin-orbit coupling is proportional to the gradient of the electrostatic potential. Therefore, it becomes prominent if heavy elements are taken into account.

The full-potential approach is necessary for the study of elastic properties [17], for the relaxation of crystal structures [18], and especially for the study of systems with large crystallographic anisotropy, as it occurs again on surfaces and interfaces. The investigation of surfaces and interfaces of oxides has become very important in Halle, due to the *collaborative research centre SFB 762: Functionality of Oxide Interfaces*. Oxides represent a large class of materials, which can be tuned to offer certain electric and magnetic properties with high technological relevance. One example is provided by zinc oxide which can be forced to become a semiconducting ferromagnet by introducing impurities or vacancies [19, 20].

The computer code *Hutsepot* [21, 22], which is based on the KKR method, has been used successfully for the investigation of oxides and their magnetic properties [23, 24], the treatment of strongly correlated electrons [25, 26] and magnetic excitations [27, 28, 29] during the past years. Up to now, a fully-relativistic full-potential implementation of the KKR method like used in other codes [30, 31] was still missing, but has been developed during the work of this thesis.

However, before one can start the discussion of relativistic extensions, results ob-

tained by the non-relativistic KKR method are presented in Part I. Following a short introduction of the non-relativistic KKR method in Chapter 2, a theoretical investigation of the electronic and magnetic structure of PrMnO_3 and CaMnO_3 is presented in Chapter 3. Due to their complex structure and their sensitive response to structural or magnetic perturbations, the study of manganites is very challenging and has attracted the attention of the research community during the past two decades [32, pp. 2-4]. In addition to the relativistic KKR method, a *Mathematica* [33] group theory package *GTPack* has been developed, which will be published in a book in the near future [Ge1]. According to an experimental observation, where it was found that magnetic moments of single holmium atoms on a highly conductive metallic substrate can reach lifetimes of the order of minutes [Ge6], the application of group theoretical methods in terms of crystal field theory to such problems is presented in Chapter 4.

In Part II of the thesis an implementation of the fully-relativistic full-potential KKR method for the code *Hutsepot* will be discussed. The central point of the implementation is the solution of the single-site scattering problem. After the successful implementation of a non-relativistic full-potential method of DRITTLER [7], where this part was solved using the LIPPMANN-SCHWINGER equation, it was shown by HUHNE *et al.* [30] that the same approach can also be used to solve the DIRAC equation for a non-spherical scattering potential. For the non-relativistic full-potential problem, ZABLOUDIL *et al.* [34, p. 76] compared the solution by means of the LIPPMANN-SCHWINGER equation with the direct solution of the differential equations and illustrated that large deviations between both solutions were found. However, a multitude of efficient and highly accurate numerical methods for the solution of coupled ordinary differential equations with various underlying properties has been developed during the past century [35]. Therefore, in contrast to previous implementations [7, 30], a solver based on the direct solution of the underlying differential equations was developed.

After the theory has been explained in Part II, tests of the implementation [Ge2] are discussed in Part III. For spherically symmetric screened atomic potentials, it was found that the asymptotic behaviour of the irregular scattering solutions in the non-relativistic limit $c \rightarrow \infty$ does not fit to the expected asymptotic behavior of the non-relativistic irregular scattering solutions close to the origin $r \ll 1$. To understand this phenomenon a complete discussion of the COULOMB problem for irregular scattering solutions in Chapter 7 and a proof of the correctness of this behavior by using an elegant transformation of the DIRAC equation for spherically symmetric potentials, as suggested by SWAINSON and DRAKE [36], will be given. Afterwards the numerical solution of the fully-relativistic single-site scattering problem for the non-spherical MATHIEU-potential will be discussed in Chapter 8 by means of integral and differential equations. Since the spherically symmetric component of the MATHIEU-potential is in the same order of magnitude as the non-spherical compo-

nents it can be seen, first, as a test of the implementation for highly anisotropic potentials and, second, as a good approximation for empty spheres as they are required in the application of the KKR method to oxides. It will be shown that the underlying differential equations are non-stiff and can be solved by applying the ADAMS-BASHFORTH-MOULTON predictor-corrector method [34, pp. 60-61].

Finally, in Chapter 9 fully-relativistic band structure calculations for the investigation of tin and lead telluride alloys $\text{Sn}_x\text{Pb}_{1-x}\text{Te}$ will be presented. Such materials played a significant role during the 1960s and 1970s [37] as infrared sensors. However, tellurides attracted attention a second time, since they are prominent candidates for the realization of topological insulators [38, 39]. For instance for SnTe, the reason for that is an inversion of the band characteristic at the L -point in the BRILLOUIN zone. It is shown that besides the size of the band gap, also the band inversion can be tuned by alloying, by applying hydrostatic pressure or by applying uniaxial strain.

Part I.

Application of non-relativistic methods to complex materials

2. The non-relativistic Korringa-Kohn-Rostoker Green function method

2.1. The main formalism in a nutshell

Within this section a basic overview about the non-relativistic KORRINGA-KOHN-ROSTOKER GREEN function method is given. The description is shortened as much as possible since a lot of principles are similar to the relativistic version which will be explained in detail in Part II. More detailed descriptions of the non-relativistic KKR method can be found within the literature [7, 40, 41, 42].

The reformulation of the original KKR band structure method [1] in terms of a GREEN function method [2] has a lot of advantages. For example, the GREEN function allows the analytical treatment of perturbations (see Section 5.4). Furthermore, physical quantities like the charge density and the magnetization density can be calculated if the GREEN function of a system is known. The formalism can be embedded into the framework of density functional theory (see Appendix A), where the ground state properties of the many particle system can be calculated from the electron density. The electron density is not calculated by solving a many particle SCHRÖDINGER equation (or DIRAC equation) but self-consistently by the solution of an effective one particle KOHN-SHAM equation.

The approach via multiple-scattering theory is based on the decomposition of a perfect crystal into distinct scattering centres [3]. Considering a perfect crystal, concentrating on one single atom and substituting all other atoms with vacuum at each lattice site, it is possible to think about a single-site scattering problem, where an initial plane wave excites a spherical wave at the atomic site (see Figure 2.1). Imagine that it is possible to construct the WIGNER-SEITZ cell Ω around the atom and to define the effective potential $V(\mathbf{r})$ such that it is non-zero in the inside and zero in the outside of the cell. Due to the influence of the neighbouring atoms and the non-spherical shape, the effective potential at each atomic site is non-spherical in general. By using atomic RYDBERG units, the KOHN-SHAM equation at each site can be formulated as follows

$$(-\nabla^2 + V(\mathbf{r}) - E) \psi_{lm}(\mathbf{r}) = 0. \quad (2.1)$$

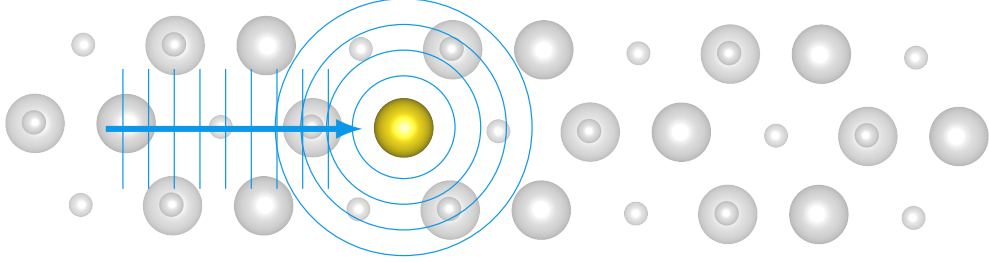


Figure 2.1.: Illustration of a single-site scattering event.

According to DRITTLER [7, p. 17], by transforming to spherical polar coordinates and by expanding the effective potential $V(\mathbf{r})$ and the wave function $\psi_{lm}(\mathbf{r})$ into spherical harmonics,

$$\psi_{lm}(\mathbf{r}) = \sum_{l'm'} \frac{1}{r} \phi_{l'm',lm}(r) Y_l^m(\hat{\mathbf{r}}), \quad (2.2)$$

equation (2.1) can be reformulated in the following way,

$$\sum_{l''} \sum_{m=-l''}^{l''} \left[\left(-\frac{d}{dr^2} + \frac{l(l+1)}{r^2} - E \right) \delta_{ll''} \delta_{mm''} + V_{lm,l''m''}(r) \right] \phi_{l''m'',l'm'} = 0. \quad (2.3)$$

Here, the orthogonality relation of the spherical harmonics was used and $V_{lm,l''m''}(r)$ denotes the matrix element

$$V_{lm,l''m''}(r) = \int d\hat{\mathbf{r}} Y_l^m(\hat{\mathbf{r}})^* Y_{l''}^{m''}(\hat{\mathbf{r}}) V(\mathbf{r}). \quad (2.4)$$

Whereas equation (2.1) is a partial differential equation in three coordinates, equation (2.3) is an infinitely large system of coupled ordinary differential equations. From equation (2.1) it is possible to obtain two linear independent solutions $\psi_{lm}^1(\mathbf{r})$ and $\psi_{lm}^2(\mathbf{r})$, which are called regular and irregular scattering solution, respectively. In the following $\psi_{lm}^1(\mathbf{r})$ and $\psi_{lm}^2(\mathbf{r})$ will be denoted by $R_{lm}(\mathbf{r})$ and $H_{lm}(\mathbf{r})$.

Since the potential is zero outside of the WIGNER-SEITZ cell, the solution of (2.3) in this region is given by a linear combination of the spherical BESSEL function $\mathcal{J}_{lm}(\mathbf{r}) = j_l(\sqrt{E}r) Y_l^m(\hat{\mathbf{r}})$ and the spherical HANKEL function of the first kind $\mathcal{H}_{lm}(\mathbf{r}) = h_l(\sqrt{E}r) Y_l^m(\hat{\mathbf{r}})$. In general, inside of the WIGNER-SEITZ cell the regular and irregular solutions have to be found numerically, where the boundary conditions are given by matching conditions with the free regular and irregular solutions at the

boundary of the WIGNER-SEITZ cell $\bar{\Omega}$ [7, pp. 18-23],

$$R_{lm}(\mathbf{r}_B) = \mathcal{J}_{lm}(\mathbf{r}_B) - i\sqrt{E} \sum_{l'm'} \mathcal{H}_{l'm'}(\mathbf{r}_B) t_{l'm',lm}. \quad (2.5)$$

and

$$H_{lm}(\mathbf{r}_B) = \mathcal{H}_{lm}(\mathbf{r}_B), \quad \mathbf{r}_B \in \bar{\Omega}. \quad (2.6)$$

In the above equation, $t_{l'm',lm}$ denote a matrix element of the single-site t-matrix. For a spherically symmetric potential, the single-site scattering t-matrix is a diagonal matrix $t_{lm,l'm'} = \delta_{ll'}\delta_{mm'}t_{lm}$ and can be related to the phase shift η_{lm} [43, p. 36] via

$$t_{lm} = -\frac{1}{\sqrt{E}} \sin(\eta_{lm}) \exp(i\eta_{lm}). \quad (2.7)$$

The phase shift η_{lm} quantifies the shift between a free solution and a scattering solution for a spatially bounded scattering potential (see Figure 2.2).

In contrast to the single-site scattering event, which was discussed so far, Figure 2.3 illustrates a multiple scattering event, where an initial wave excites several spherical waves at distinct scattering centres along all possible paths. With the help of the single-site solutions $R_{lm}^i(\mathbf{r})$ and $H_{lm}^i(\mathbf{r})$ at certain scattering sites i it is possible to construct the retarded multiple-scattering GREEN function [44] according to

$$G(\mathbf{r} + \mathbf{R}_i, \mathbf{r}' + \mathbf{R}_j, z) = \sum_{lm} \sum_{l'm'} R_{lm}^i(\mathbf{r}, z) G_{lm'l'm'}^{ij}(z) R_{lm}^j(\mathbf{r}', z) + \delta_{ij} \sum_{lm} R_{lm}^i(\mathbf{r}_{<}, z) H_{lm}^j(\mathbf{r}_{>}, z), \quad \mathbf{r} \in \Omega_i, \mathbf{r}' \in \Omega_j. \quad (2.8)$$

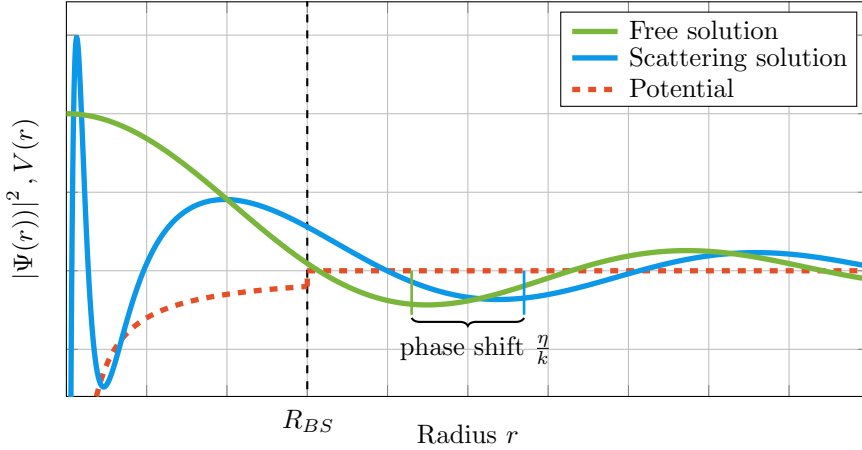


Figure 2.2.: Illustration of the phase shift η , describing the shift between a scattering solution outside of a spatially bounded scattering potential and a free solution.

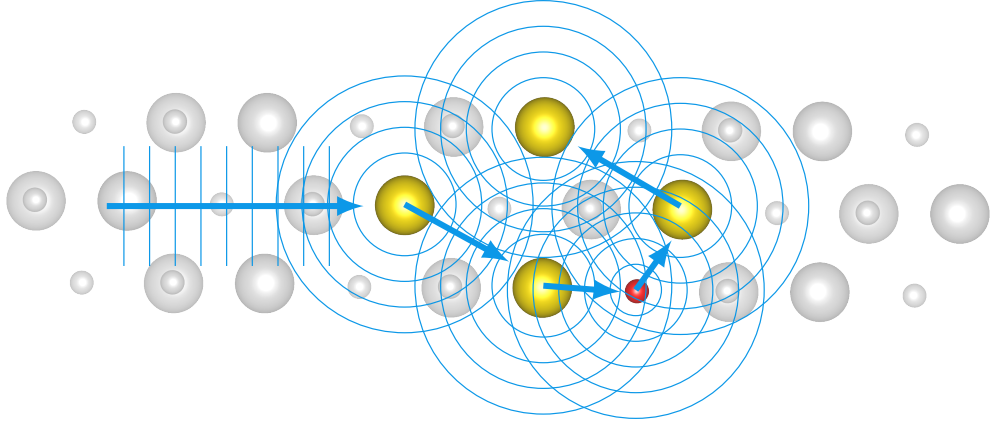


Figure 2.3.: Illustration of a multiple scattering event along a certain path.

Here, z denotes the complex energy $z = E + i\delta$ and $\mathbf{r}_<$ and $\mathbf{r}_>$ are an abbreviation for the one vector of \mathbf{r} and \mathbf{r}' with the smaller and the larger absolute value, respectively. Whereas the second term on the right hand side of equation (2.8) represents the single-site scattering contribution of a certain site i , the first one combines regular scattering solutions of the sites i and j and hence represents the multiple-scattering contribution. $\tilde{G} = \{G_{lm'l'm'}^{ij}\}$ is called structural GREEN function matrix. Combining all single-site t-matrices of N scattering sites to a matrix \tilde{T} ,

$$\tilde{T} = \begin{pmatrix} \tilde{t}^1 & \dots & \tilde{0} \\ \vdots & \ddots & \tilde{0} \\ \tilde{0} & \tilde{0} & \tilde{t}^N \end{pmatrix}, \quad (2.9)$$

the structural GREEN function matrix can be obtained self-consistently by means of \tilde{T} and the structure constants \tilde{G}^0 via the algebraic DYSON equation

$$\tilde{G} = \tilde{G}^0 + \tilde{G}^0 \tilde{T} \tilde{G}^0 + \tilde{G}^0 \tilde{T} \tilde{G}^0 \tilde{T} \tilde{G}^0 + \dots = \tilde{G}^0 \left[\tilde{I} - \tilde{T} \tilde{G}^0 \right]^{-1}. \quad (2.10)$$

The analytic form of the structure constants can be found i.e. in the book of ZABLOUDIL *et al.* [34, pp. 24-25]. The convergence of the KKR method can be improved by using so-called screened structure constants, which are discussed in the work of ZELLER *et al.* [44] and SZUNYOGH *et al.* [45].

If the GREEN function is known, it is possible to calculate the density of states as well as the charge density from the imaginary part of the retarded GREEN function,

$$n(E) = -\frac{1}{\pi} \Im \int d\mathbf{r} G(\mathbf{r}, \mathbf{r}, E + i\delta) \quad \text{and} \quad \rho(\mathbf{r}) = -\frac{1}{\pi} \Im \int_{\underline{}} d z G(\mathbf{r}, \mathbf{r}, z). \quad (2.11)$$

Instead of calculating the band structure directly, which might be very cumbersome, it is possible to obtain the so called BLOCH spectral function via FOURIER transformation of the GREEN function for periodic systems. The imaginary part of the \mathbf{k} resolved GREEN function gives a band structure like result [46, p. 128],

$$A_B(\mathbf{k}, W) = -\frac{1}{\pi} \text{Im Tr} \left[\sum_{\mathbf{R}_j \in \mathcal{L}} e^{i\mathbf{k} \cdot \mathbf{R}_j} \int d^3 r_j G(\mathbf{r}_j, \mathbf{r}_j + \mathbf{R}_j, W) \right]. \quad (2.12)$$

The summation in the last expression extends over all vectors \mathbf{R}_j of the lattice denoted by \mathcal{L} . In the framework of density functional theory the charge density can be used to construct a new effective potential and, furthermore, to calculate the total energy of the electron gas [47, p. 61] via

$$E[\rho(\mathbf{r})] = T_s[\rho(\mathbf{r})] + \int d\mathbf{r} V(\mathbf{r})\rho(\mathbf{r}) + V_H[\rho(\mathbf{r})] + E_{xc}[\rho(\mathbf{r})]. \quad (2.13)$$

Here, T_s denotes the functional for the kinetic energy, V_H denotes the HARTREE functional, which takes into account the electron-electron interaction, and last but not least E_{xc} denotes the exchange-correlation functional.

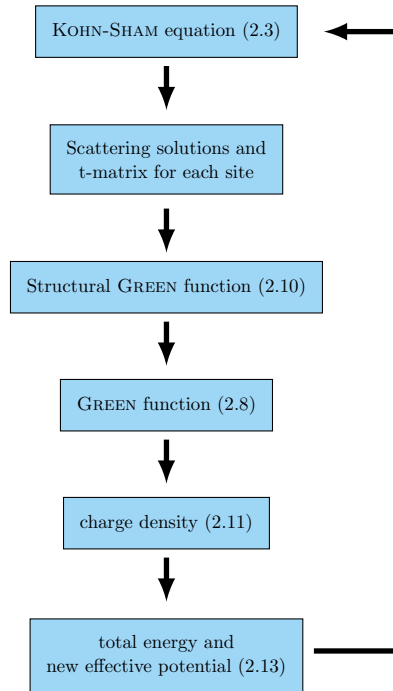


Figure 2.4.: Illustration of the self-consistency cycle of the KKR method.

Whereas in the many particle SCHRÖDINGER equation the potential is known explicitly, the effective potential of the one-particle KOHN-SHAM equation is not. In practice, this effective potential is obtained self-consistently by starting with a trial potential. For the trial potential, it is possible to solve the differential equation (2.3) and to construct the GREEN function according to (2.8). Afterwards the charge density can be calculated from equation (2.11). In turn, the charge density can be used to calculate the total energy and a new trial potential. This scheme is repeated, until the change of the total energy between two cycles becomes reasonably small. An illustration of the self-consistency cycle of the KKR method can be found in Figure 2.4.

2.2. The treatment of disorder using the coherent potential approximation

The possibility of alloying materials allows to design technologically relevant properties. For example, the alloy $\text{GaAs}_x\text{P}_{1-x}$ is widely used in optoelectronics for the fabrication of light emitting diodes (LEDs). The colour of the emitted light varies with increasing amount x of arsenic from red to yellow [48, 49]. The colour of the LED, which is determined by the size of the band gap can be tuned even more by adding a fourth component, as it is possible in $\text{Ga}_y\text{In}_{1-y}\text{As}_x\text{P}_{1-x}$ [50]. Here, a second concentration y occurs.

For the computation of such materials it is necessary to apply techniques which allow a proper treatment of chemical disorder. A straightforward way is given by constructing large super cells, substituting certain atoms and averaging the possible configurations. Even though this procedure was already applied successfully [51] it has the disadvantage that it is restricted to concentrations that can be represented by stoichiometric compounds. The development of mean field theories opened a second approach to the problem. Regarding a binary alloy A_xB_{1-x} , the simplest approximation for an electronic structure calculation is the introduction of an hypothetical element with the average potential $V(\mathbf{r}) = xV_A(\mathbf{r}) + (1-x)V_B(\mathbf{r})$, which is denoted as the virtual crystal approximation [52, 53].

A more reliable GREEN function method was suggested by SOVEN in 1967 [54], which is called the single-site coherent potential approximation (CPA). A somehow similar approach was communicated by VELICKÝ, KIRKPATRICK and EHRENREICH in 1968 [55]. In both approaches an effective mean field medium is introduced. Later, the method was simplified by Gyorffy [56]. Considering an alloy with N components, where each component has the concentration x_i and the sum over all concentrations is restricted by $\sum_i x_i = 1$. It is hypothesised that the total scattering of electrons at different atomic sites in the effective medium should be equal to the electron

scattering at averaged atoms within the effective medium,

$$\sum_{i=1}^N x_i \tilde{\tau}^{i,nn'}(E) = \tilde{\tau}_{\text{CPA}}^{nn'}(E). \quad (2.14)$$

Here, the scattering path operator $\tilde{\tau}$ is introduced, which is given by

$$\tilde{\tau}^{nn'}(E) = \delta_{nn'} \tilde{t}^n(E) + \sum_{m \neq n} \tilde{t}^m(E) G^{0,n}(E) \tilde{\tau}^{mn'}(E). \quad (2.15)$$

The single site scattering t-matrix \tilde{t}_{CPA}^n of the CPA medium at a certain site n is defined implicitly from the scattering path operator $\tilde{\tau}_{\text{CPA}}^{nn'}$ via equation (2.15) and has to be found self-consistently by starting with a reasonable trial matrix $\tilde{t}_{\text{CPA}}^{n,0}$ [3].

Solving the single-site scattering problem for each component and using the component projected scattering matrix $\tilde{\tau}^{i,nn'}$ to construct the multiple scattering GREEN function $G^i(\mathbf{r}, \mathbf{r}', E)$, the averaged GREEN function of the effective medium can be approximated by summation [57, 3],

$$G(\mathbf{r}, \mathbf{r}', E) = \sum_{i=1}^N x_i G^i(\mathbf{r}, \mathbf{r}', E). \quad (2.16)$$

The coherent potential approximation is implemented within *Hutsepot* and will be used later on during this thesis, e.g. in Chapter 9.

2.3. The Heisenberg Hamiltonian and the magnetic force theorem

In collinear magnetic systems (ferromagnetic, antiferromagnetic or ferrimagnetic) the magnetic moments of the atoms within a crystal are either parallel or anti-parallel to the global magnetization axis. Presuming the existence of permanent, localized moments interacting with each other via a direct or an indirect exchange mechanism, it is possible to formulate a semi-classical effective many particle Hamiltonian, called the HEISENBERG Hamiltonian [58],

$$\hat{H}^{\text{eff}} = - \sum_{i,j} J_{ij} \mathbf{e}_i \cdot \mathbf{e}_j. \quad (2.17)$$

Here, the vectors \mathbf{e}_i denote the unit vectors pointing into the direction of the spins \mathbf{S}_i . The name refers to the early work about the theory of ferromagnetism by HEISENBERG in 1928 [59]. Since the equilibrium magnetic ordering can be found by minimizing the energy of the HEISENBERG Hamiltonian, the magnetic moments of the atoms tend towards a parallel alignment (ferromagnetism) for exchange parameters $J_{ij} > 0$

and towards an anti-parallel alignment (antiferromagnetism) for exchange parameters $J_{ij} < 0$. Especially for the description of magnetic insulators the HEISENBERG model can be applied successfully [60]. For the relativistic case, the HEISENBERG model can be extended and additional terms like the DZYALOSHINSKII-MORIYA interaction [61, 62, 63] occur.

The HEISENBERG exchange parameters J_{ij} can be calculated via the magnetic force theorem and the approach of LIECHTENSTEIN *et al.* [64], where the exchange parameters are determined from the rotation energy of two spin moments at sites i and j on opposite angles $\pm\theta/2$,

$$\delta E_{ij} = (1 - \cos \theta) \approx \frac{1}{2} J_{ij} \theta^2. \quad (2.18)$$

With the help of the LLOYDS formula (see Section 6.10) the energy difference is expressed using the single-site scattering t-matrices $\tilde{t}_{i\sigma}$ at site i for the spin direction σ as well as the scattering path operator $\tilde{\tau}^{ij}$ (see equation (2.15)). Then the exchange parameters J_{ij} are calculated by means of the following equation [64, 3],

$$J_{ij} = -\frac{1}{4\pi} \Im \int_{-\infty}^{E_F} dE \operatorname{Tr} \left[\left(\tilde{t}_{i\uparrow}^{-1} - \tilde{t}_{i\downarrow}^{-1} \right) \tilde{\tau}_{\uparrow}^{ij} \left(\tilde{t}_{j\uparrow}^{-1} - \tilde{t}_{j\downarrow}^{-1} \right) \tilde{\tau}_{\downarrow}^{ji} \right]. \quad (2.19)$$

The above presented concepts of this chapter are applied to the investigation of PrMnO₃ and CaMnO₃ within the next chapter.

3. Ab-initio investigation of PrMnO₃ and CaMnO₃

3.1. Why study manganites?

During the past two decades the study of manganites has become more and more prominent within the condensed matter community. For the increasing interest at least three reasons can be emphasized [32, pp. 2-4]. First, manganites tend to show “colossal magnetoresistance”, where the resistivity increases by many orders of magnitude upon the application of small magnetic fields. Materials with notable magnetotransport properties are technologically relevant for instance in the development of hard disk drives with large storage capacity [65]. Second, some manganites are intrinsically inhomogeneous with coexisting clusters of different phases, mostly ferromagnetic and antiferromagnetic clusters. As an example, SVEDBERG *et al.* [66] found coexisting spin-glass and ferromagnetic phases for Pr_{0.9}Ca_{0.1}MnO₃ thin films at low temperatures. Third, manganites show rich phase diagrams with unusual spin, charge, lattice, and orbital order. Phase diagrams of manganites were discussed by TOKURA and TOMIOKA [67]. An illustration for Pr_{1-x}Ca_xMnO₃ alloys with a calcium content between 0% and 50% can be found in Figure 3.1. Whereas Pr_{1-x}Ca_xMnO₃ remains insulating within the whole range, the magnetic ordering changes a lot. Starting from an A-type antiferromagnetic structure for $x = 0$, where a ferromagnetic inter-plane and an antiferromagnetic intra-plane coupling of manganese atoms is present, manganese moments are slightly canted for low concentrations $x < 0.15$, which is denoted as the spin-canted insulating phase (CI). Then, between $x = 0.15$ and $x = 0.3$ a ferromagnetic phase (FI) is observed for low temperatures. In the range of $x = 0.3, \dots, 0.5$ the material becomes antiferromagnetic again, with successive magnetic transitions between an antiferromagnetic phase (AFI) and a canted antiferromagnetic phase (CAFI).

A theoretical study of manganites is challenging as can be verified within the literature [68, 69]. Again three main reasons can be pointed out. First, driven by the fact that manganites are intrinsically inhomogeneous one needs a microscopic description to understand the mechanisms behind a certain phase combined with a mesoscopic method to understand their interplay. Second, by focusing on the microscopic description, density functional theory based methods are facing problems caused by highly localized d and f electrons leading to strong correlations [70, 71]. To

achieve reasonable results one can either improve the exchange correlation functional by climbing up the “Jacob’s ladder of density functional approximations” [72] to generalized gradient approximations or higher or by applying explicit correlation corrections like the self-interaction correction [73, 25] or the so-called HUBBARD-U method [74]. Third, if one is interested in the description of phase diagrams one needs to take into account temperature. On the one hand ground state calculations can be extended by smoothening the occupation of states by means of the FERMI-DIRAC distribution function [75] or by mean-field methods like the disordered local moment method [76, 77]. On the other hand dynamical excitations like lattice vibrations have to be taken into account where the resulting electron-phonon coupling has to be included [78].

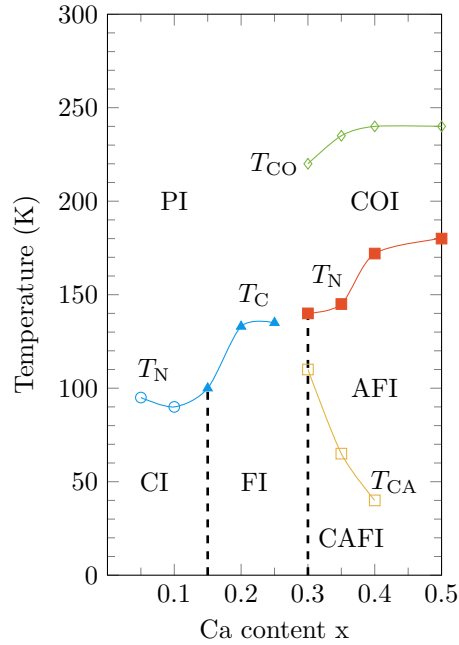


Figure 3.1.: Phase diagram of $\text{Pr}_{1-x}\text{Ca}_x\text{MnO}_3$ (illustration adopted from [67]). The abbreviations denote paramagnetic insulator (PI), ferromagnetic insulator (FI), antiferromagnetic insulator (AI), spin-canted insulator (CI), charge-ordered insulator (COI), and canted-antiferromagnetic insulator (CAFI).

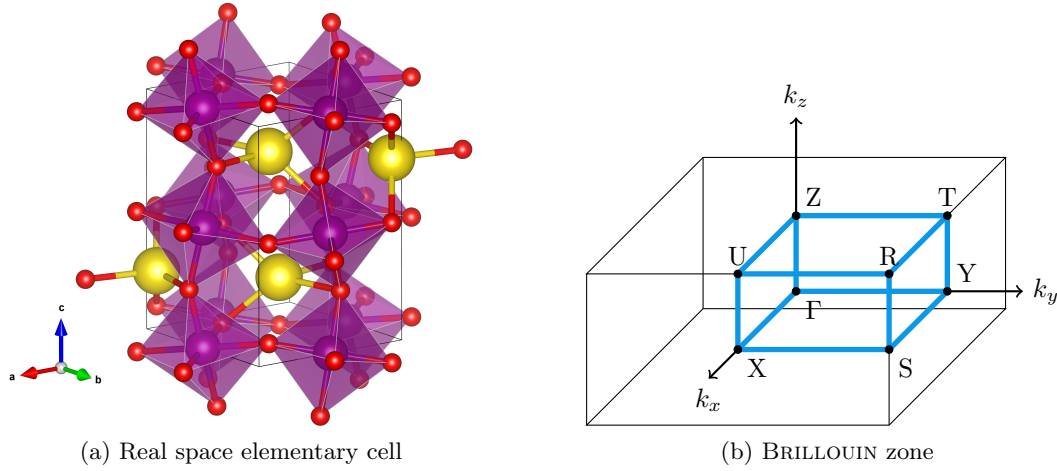


Figure 3.2.: Real space orthorhombic crystal structure and BRILLOUIN zone with high symmetry points of PrMnO_3 and CaMnO_3 . In the picture of the real space elementary cell oxygen atoms are illustrated in red and manganese atoms in purple. Yellow atoms are representing praseodymium and calcium, respectively [80].

3.2. Structure of PrMnO_3 and CaMnO_3

The manganites PrMnO_3 and CaMnO_3 are crystalizing in an orthorhombic crystal structure with the space groups $pbnm$ and $pnma$. Both space groups share the same space group index 62. The real-space structure of both materials is illustrated in Figure 3.2a. The BRILLOUIN zone of the orthorhombic unit cell is shown in Figure 3.2b. A summary of the lattice constants and atomic positions that were used during the calculations can be found in Table 3.1.

As can be verified in Figure 3.2a, the manganese atoms are surrounded by six oxygen atoms forming a slightly distorted octahedron. Each praseodymium and calcium atom is surrounded by eight of such octahedra, which are canted into the crystallographic a and b direction. For a perfect octahedron the manganese d states would split into a threefold degenerate state T_{2g} and a twofold degenerate state E_g , as can be verified with the help of the *Mathematica* group theory package *GTPack* [Ge4]. However, for PrMnO_3 and CaMnO_3 it is favoured to decrease the symmetry furthermore leading to a splitting of the T_{2g} and E_g states into states with lower degeneracy [32, pp. 57-69]. As a result the occupied levels are lower in energy and hence also the total energy of the system is decreased. This phenomenon, which is known as JAHN-TELLER distortion, was initially described by JAHN and TELLER in 1937 [79].

Cell (PrMnO₃)			
Space group	PBNM (62)		
Lattice constants [Å]	5.5326(2)	5.6176(2)	7.8513(3)
Angles	90.00000	90.00000	90.00000
WYCKOFF positions			
Pr (4c)	0.992(1)	0.0350(8)	0.250
Mn (4b)	0.5	0	0
O (4c)	0.0762(7)	0.4825(7)	0.250
O (8d)	0.7126(5)	0.2970(4)	0.0416(3)
Cell (CaMnO₃)			
Space group	PNMA (62)		
Lattice constants [Å]	5.28930	7.45644	5.27074
Angles	90.00000	90.00000	90.00000
WYCKOFF positions			
Ca (4c)	0.0198(17)	0.25000	-0.004(4)
Mn (4b)	0.00000	0.00000	0.50000
O (4c)	0.493(2)	0.25000	0.0658(20)
O (8d)	0.2882(10)	0.0362(9)	-0.2917(10)

Table 3.1.: Experimental structure data of PrMnO₃ [81] and CaMnO₃ [82]. The data was used for the construction of the unit cell for the calculations.

3.3. Computational methods

The following results were obtained from calculations using a screened scalar-relativistic KORRINGA-KOHN-ROSTOCKER GREEN function method [83, 84], as implemented in *Hutsepot* [21]. The electron density was calculated by means of a multipole expansion, taking into account the shape of the VORONOI polyhedra around each atom within the unit cell [85, 86]. For the integration of the imaginary part of the GREEN function over the energy to calculate the electron density (see equation (2.11)), a semi-circular energy contour was chosen, consisting of 24 points. The expansion of the GREEN function into spherical harmonics was restricted to a maximal angular momentum of 3.

The unit cell was constructed according to the data of Table 3.1, where four manganese atoms, four praseodymium or calcium atoms and 12 oxygen atoms are present. To achieve better convergence for the self-consistent calculations, ten additional empty spheres were added at non-occupied crystallographic sites using the

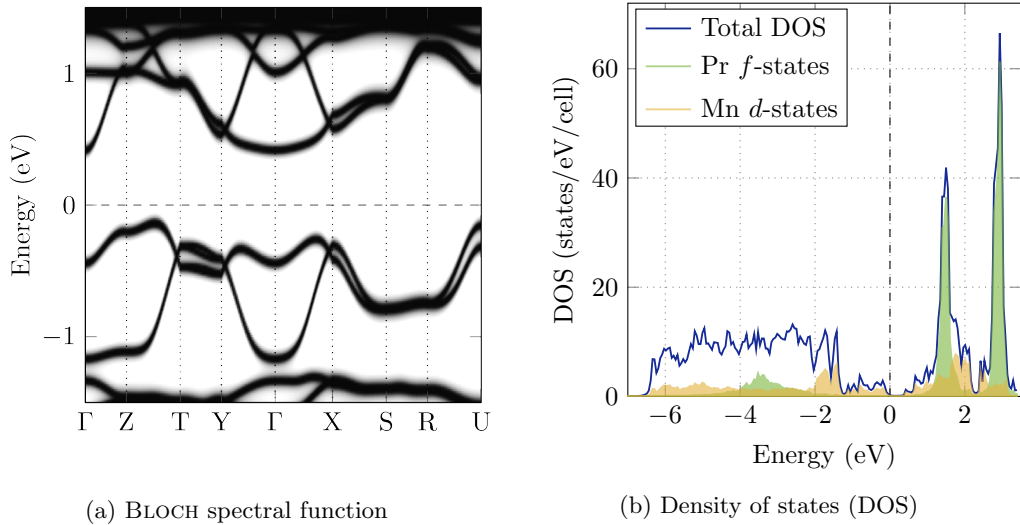
Stuttgart TB-LMTO program [87]. Due to the large unit cell a mesh of $8 \times 8 \times 4$ points was sufficient for integration in \mathbf{k} -space. As an approximation for the exchange-correlation functional the revised generalized gradient approximation PBE-SOL was used [88], as it is implemented within the *LibXC* database [89]. To treat the strongly correlated electrons the HUBBARD-U method (or GGA+U method) was applied to manganese d states and praseodymium f states with values of $U_d = 1 - 1.25$ eV and $U_f = 5$ eV, respectively. The HEISENBERG exchange parameters J_{ij} were calculated by means of the magnetic force theorem, according to equation (2.19). The obtained exchange parameters were used to calculate the critical temperature by means of a Monte-Carlo method implemented by FISCHER [40].

Furthermore, results for PrMnO_3 with and without relaxation of the unit cell, were compared to each other. The relaxation of the unit cell was obtained by using the *Vienna ab initio simulation package* (VASP) [90]. Analogously to SATHYANARAYANA, a Γ centred $6 \times 6 \times 6$ \mathbf{k} -point mesh was applied [91]. Calculations were done using the high performance mode and a plane wave energy cut-off of 400 eV. The relaxation was restricted to that of the lattice parameters whereas the positions of the atoms and the cell shape were fixed. The minimum was found by using a conjugate-gradient algorithm [92, pp 413-417]. In accordance with the KKR calculations the generalized gradient approximation was used and a HUBBARD-U was applied to manganese d states (1 eV) and praseodymium f states (5 eV). It was found that the unit cell volume decreases slightly, but the general results, such as the density of states or the HEISENBERG exchange parameters, are not affected.

3.4. Electronic structure

Both materials, PrMnO_3 as well as CaMnO_3 , are semiconductors with experimental band gap energies of ≈ 0.83 eV [93] and ≈ 1.55 eV [94], respectively. Due to correlation effects, this property is not reproduced within a calculation using the generalized gradient approximation only. Therefore, the HUBBARD-U method was applied. The choice of an appropriate value of U is crucial, since physical quantities like the size of the band gap, the magnetic moment of manganese and praseodymium, the HEISENBERG exchange parameters J_{ij} , the magnetic ordering and the critical temperature are sensitive to the magnitude of U . For PrMnO_3 the HUBBARD-U was applied to praseodymium f -states (U_f) and manganese d -states (U_d). Calculations were performed for $U_f = 3, 4, 5, 6$ eV and $U_d = 0, 1, \dots, 4$ eV. The best agreement with experimental values for the band gap and the critical temperature [95] was achieved for $U_f = 5$ eV and $U_d = 1$ eV.

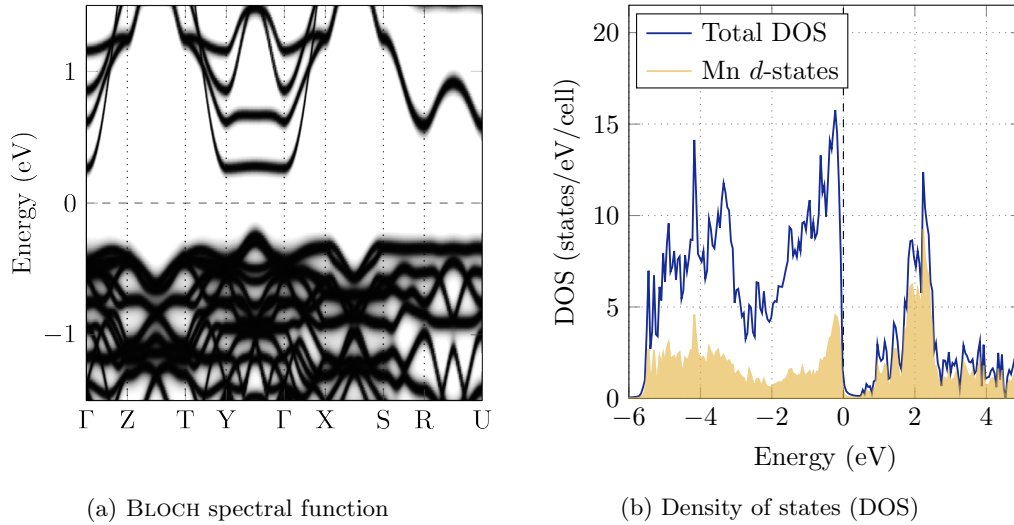
According to the BLOCH spectral function (see Figure 3.3a) it can be verified that PrMnO_3 is an indirect semiconductor, where the valence band maximum can be found at U and the conduction band minimum at the Γ point in the BRILLOUIN

Figure 3.3.: Electronic structure of PrMnO₃.

zone. The band gap is slightly underestimated and shows a value of ≈ 0.5 eV which is also reflected in the density of states in Figure 3.3b. From the density of states it can be verified that the valence band maximum as well as the valence band minimum is dominated by manganese *d*-states. Beyond the FERMI energy two sharp peaks can be seen, which belong to non-occupied praseodymium *f*-states. The range between -7 eV and -2 eV is dominated by oxygen *p*-states.

For CaMnO₃ the best agreement with experimental values (such as magnetic moment, band gap, etc.) was obtained for a slightly increased value of $U_d = 1.25$ eV. Analogously to PrMnO₃, CaMnO₃ is an indirect semiconductor as well, as can be verified from Figure 3.4a where the valence band maximum is located along the path $Y\Gamma$ and the conduction band minimum at Γ and Y . Again, the size of the band gap is about 0.5 eV. In contrast to PrMnO₃, the manganese *d*-states are hybridizing with oxygen *p*-states for CaMnO₃ in the whole range of the valence band between -6 eV and 0 eV, as can be seen in the density of states illustrated in Figure 3.4b. The conduction band is dominated mainly by manganese *d*-states.

For PrMnO₃ and CaMnO₃ a change of the oxidation state of manganese can be observed. The electron configuration of manganese is given by $[\text{Ar}] 3d^5 4s^2$. Due to the two *s*- and five *f*-electrons, possible oxidation states for manganese in compounds are between +2 and +7. Since calcium belongs to the group of alkaline earth metals it carries two *s*-electrons in the outermost shell leading to an oxidation number of +2 in CaMnO₃. Together with the oxidation state of -2 for oxygen, manganese is forced to have an oxidation state of +4. According to HUND's rule the remaining *d*-electrons are occupying different *d*-orbitals with a parallel spin alignment leading

Figure 3.4.: Electronic structure of CaMnO_3 .

to a magnetic moment of $3 \mu_B$. Corresponding to JIRÁK *et al.* [96], a slightly lower magnetic moment of $2.66 \mu_B$ was measured in neutron diffraction experiments. Nevertheless, this value is in very good agreement to the present calculations, where a magnetic moment of $2.7 \mu_B$ was observed on each manganese atom. For PrMnO_3 the calculated magnetic moment is given by $3.6 \mu_B$ leading to the conclusion that the oxidation state of manganese has decreased. Again, the experimental value of $3.54 \mu_B$ is in very good agreement [96] with the calculation. Anyway, since the experimental as well as the calculated manganese magnetic moments are non-integer values it is very likely that mixed configurations of manganese +4 and +3 as well as manganese +3 and +2 are present in PrMnO_3 and CaMnO_3 , respectively. Regarding the electron configuration of praseodymium, which is given by $[\text{Xe}] 4f^3 6s^2$ an oxidation state of +3 will give a magnetic moment of $2 \mu_B$ which results from the occupation of two distinct f -orbitals of the remaining two $4f$ electrons with parallel spin alignment. In accordance, the computational value for the magnetic moment of praseodymium in PrMnO_3 was found to be exactly $2 \mu_B$. However, this value stays in contrast to the experimental value of JIRÁK *et al.* who suggested a magnetic moment of $0.5 \mu_B$ [96]. Nevertheless, in recent neutron diffraction experiments [97], the present theoretical prediction of the praseodymium high-spin state $2 \mu_B$ was used to fit the experimental

results and was found to be more likely than the previous result of JIRÁK *et al.* [96].

3.5. Magnetic structure

To obtain information about the magnetic structure the magnon spectrum of PrMnO₃ and CaMnO₃ was calculated. Assuming collinear magnets and the adiabatic approximation, the magnon spectrum can be found from the eigenvalues of the torque matrix [41, pp. 31-34]. According to Figure 3.5a, the minimum of the magnon spectra for PrMnO₃ is located at the Z point in the BRILLOUIN zone. Furthermore the spectrum is symmetric, regarding positive and negative energies. Hence, the magnon spectrum does not show a ferromagnetic behaviour, which is in agreement with the literature [96]. It was suggested by JIRÁK *et al.* that PrMnO₃ is an A-type antiferromagnet [96, 69], meaning that the intra-plane coupling is ferromagnetic while the inter-plane coupling is antiferromagnetic. The antiferromagnetic ordering can be verified by regarding the HEISENBERG exchange parameters J_{ij} (see Figure 3.6a). The results of the calculations show large and positive HEISENBERG exchange parameters between manganese atoms within the *a-b*-plane ($J=9.4$ meV), which cause the in-plane ferromagnetic ordering. The coupling between praseodymium and manganese tends to be ferromagnetic ($J\approx 1-2$ meV). For the magnetic coupling between two manganese planes, positive exchange parameters can be found for the coupling between Mn1 and Mn3 ($J=3.8$ meV), whereas negative exchange parameters can be observed for the interaction between Mn1 and Mn4 ($J=-1.2$ meV). Even though the absolute value

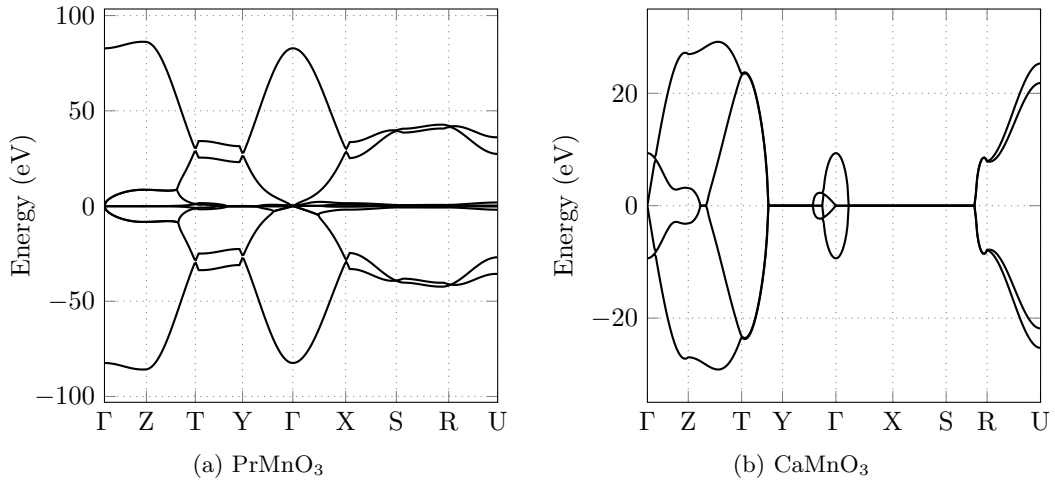


Figure 3.5.: Magnon spectra of PrMnO₃ and CaMnO₃ calculated using the torque matrix formalism in the framework of adiabatic spin-dynamics [98].

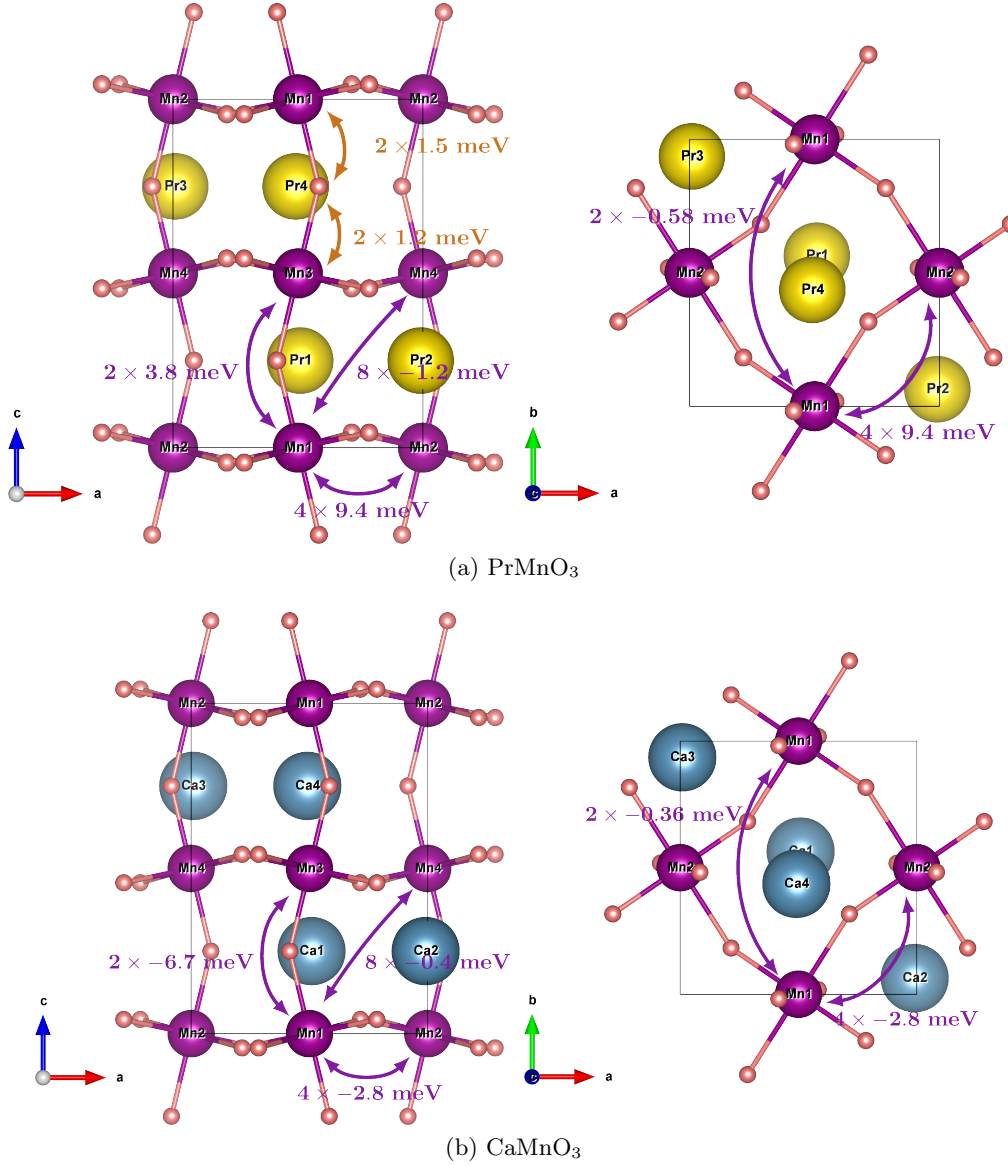


Figure 3.6.: Calculated HEISENBERG exchange parameters J_{ij} for PrMnO₃ and CaMnO₃. 8×-1.2 meV for instance denotes that 8 equivalent atoms and hence 8 equivalent exchange parameters are present.

of -1.2 meV is smaller than 3.8 meV, Mn4 occurs eight times in the neighbourhood of Mn1 whereas Mn3 only occurs 2 times. Furthermore, the calculated HEISENBERG exchange parameters were used to confirm the magnetic ordering by means

of a Monte Carlo method (for details of the method see [40, pp. 34-35]), where the antiferromagnetic structure was clearly revealed and a transition temperature of ≈ 120 K could be found. However, the system seems to be at the border between antiferromagnetism and ferromagnetism and therefore it reacts very sensitive with respect to small perturbations.

For CaMnO₃, WOLLAN and KOEHLER [99] found a G-type antiferromagnetic ordering using neutron diffraction experiments, where both intra-plane and inter-plane coupling are antiferromagnetic. This type of antiferromagnetic coupling agrees well with the calculated values for the HEISENBERG exchange parameters in Figure 3.6b. Since calcium is non-magnetic, the HEISENBERG exchange parameters J_{ij} for CaMnO₃ only describe coupling between manganese atoms. According to the results, all parameters are negative and hence both inter- and intra-plane coupling tends to be antiferromagnetic. The calculated critical temperature of 91 K is slightly lower than the experimental critical temperature of 110 K.

4. Application of group theoretical methods to magnetic states of Ho on Pt(111)

4.1. Introduction

Within the past decades, the data storage capacity of memory devices has increased rapidly [100]. In magnetic data storage, where ferromagnetic materials are used, this trend has led to a decrease of the size of magnetic islands, in which each bit is stored. To keep their magnetization in a specific direction against thermal fluctuations materials with high magnetic anisotropy are needed. In recent years, magnetic anisotropy

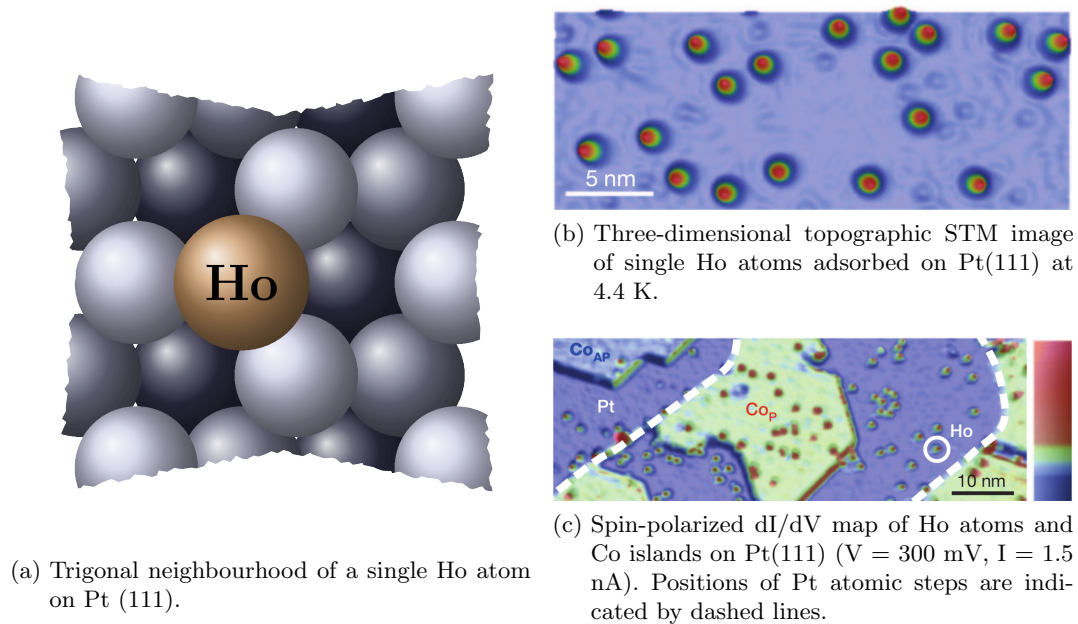


Figure 4.1.: Illustration of Ho on a Pt(111) surface. The pictures in (b) and (c) were obtained by MIYAMACHI *et al.* using scanning tunneling microscopy [Ge6].

measurements were performed using scanning tunnelling microscopy for a wide range of substrates and atoms [101, 102, 103]. A first breakthrough was achieved by the work of HIRJIBEHEDIN *et al.* [104] who discovered a large anisotropy for iron and manganese atoms on a thin layer of copper nitride.

A major reason for unstable magnetic moments on surfaces is seen by the interaction with scattering electrons. Since f electrons are strongly localized the interaction of f -electrons and surface electrons is weaker in comparison to systems where the valency electrons are d -electrons. Since f -electrons are causing large magnetic moments in single-atoms, promising candidates for single-bit data storage devices are rare earth atoms. In cooperation with the experimental group of WULFHEKEL (at KIT Karlsruhe), magnetic excitations of gadolinium atoms on platinum (111) and copper (111) surfaces [Ge7] as well as holmium atoms on a platinum (111) surface [Ge6] were investigated (see Figure 4.1). Surprisingly it could be observed that the magnetic excitations in single holmium atoms on high conducting surfaces can reach lifetimes of the order of minutes.

Besides a description via *ab initio* methods, group theoretical methods in the framework of crystal field theory were developed [Ge4] and implemented within the *Mathematica* group theory package *GTPack* [Ge1]. During this chapter it will be explained, how such methods can be applied to describe the large magnetic anisotropy as well as the long lifetimes of magnetic excitations in single holmium atoms on a platinum (111) surface.

4.2. Qualitative discussion

At first, a qualitative discussion of the level splitting for a single holmium atom on a platinum (111) surface will be given. For the electronic structure of holmium it is assumed that 10 electrons occupy the $4f$ state [105]. Due to spin orbit coupling the 14-fold degenerate $4f$ state (spin is taken into account) splits into a 6-fold degenerate state $4f_{5/2}$ and an 8-fold degenerate state $4f_{7/2}$. Since $4f_{5/2}$ is lower in energy [106] four electrons occupy $4f_{7/2}$ which leads to a total angular momentum of $J = 8$.

For $J = 8$ it is possible to construct 17 basis vectors $|8m\rangle$ ($m = -8, \dots, 8$) belonging to the irreducible representation D^8 . Representation matrices of proper rotations of D^8 are given by the WIGNER-D-matrices of each group element of the group $SO(3)$ and can be calculated using *Mathematica*. For improper rotations a factor $(-1)^J$ has to be multiplied. From the matrix element theorem [107, pp. 130-134] it is known that each irreducible representation leads to an energy level of which the degeneracy is equal to the dimension of the irreducible representation.

For a single holmium atom on a platinum (111) surface the local symmetry is decreased by the crystal field of the surface and the associated point group is given by C_{3v} (see Figure 4.1a). For the point group C_{3v} the representation given by matrices

of D^8 is reducible. The number of times an irreducible representation occurs within a reducible representation can be calculated from

$$n_p = \frac{1}{g} \sum_T [\chi^p(T)]^* \chi(T), \quad (4.1)$$

which can be derived from the orthogonality theorem for characters [Ge1]. Here, g is the order of the group and the characters $\chi(T)$ are given by the trace of the representation matrix of the element T . To calculate the characters of the irreducible representations the BURNSIDE algorithm [108] was implemented in the *Mathematica* group theory package *GTPack*. From equation (4.1) it is possible to verify that D^8 is reducible according to

$$D^8 \sim 3A_1 \oplus 6E \oplus 2A_2. \quad (4.2)$$

In the equation above, the MULLIKEN notation is used [109, 110], where A_1 and A_2 are the symmetric and the antisymmetric one-dimensional irreducible representations and E the two-dimensional irreducible representation of C_{3v} . The character table of C_{3v} can be found in Table 4.1.

	\mathcal{C}_1	\mathcal{C}_2	\mathcal{C}_3	
A_1	1	1	1	$\mathcal{C}_1 = \{E\}$
A_2	1	1	-1	$\mathcal{C}_2 = \{C_{3z}, C_{3z}^{-1}\}$
E	2	-1	0	$\mathcal{C}_3 = \{IC_{2y}, IC_{2C}, IC_{2D}\}$

Table 4.1.: Character table and classes of the point group C_{3v} , calculated with *GTPack* [Ge1]. Symmetry elements are denoted in SCHÖNFLIES notation.

4.3. Quantitative discussion

In connection to the qualitative analysis of the splitting of holmium energy levels in a trigonal crystal field, it will be described in this section how the strength of the splitting can be approximated in the framework of linear perturbation theory. First, it will be explained how the crystal field Hamiltonian can be achieved if the point group is known and second it will be shown how the eigenvalue equation can be solved in an efficient way.

4.3.1. Crystal field Hamiltonian

In the following, it is assumed that the solution of a reference Hamiltonian \hat{H}_0 is known and the influence of the crystal field is small enough to treat it as a perturbation. The Hamiltonian of the perturbed system is given by $\hat{H} = \hat{H}_0 + V_{\text{cr}}$. The

crystal field can be expanded into tesseral harmonics (real spherical harmonics) S_k^q ,

$$V_{\text{cr}}(\theta, \phi) = \sum_{k=0}^{\infty} \sum_{q=-k}^k B_k^q S_k^q(\theta, \phi), \quad (4.3)$$

where the radial part of the crystal field is included in the coefficients B_k^q . The crystal field has a certain symmetry reflected in the point group \mathcal{G} . Since the Hamiltonian is an irreducible tensor operator belonging to the identity representation Γ_1 of \mathcal{G} , it has to be invariant under the application of the character projection operator \hat{P}^{Γ_1} ,

$$\hat{P}^{\Gamma_1} V_{\text{cr}}(\theta, \phi) = \frac{1}{g} \sum_{T \in \mathcal{G}} \hat{P}(T) V_{\text{cr}}(\theta, \phi) = V_{\text{cr}}(\theta, \phi). \quad (4.4)$$

The tesseral harmonics S_k^q are a real space representation of the $(2k+1)$ -dimensional basis belonging to the irreducible representation D^k . Hence, every transformation can be expressed via $\hat{P}(T) S_k^q = \sum_{q'=-k}^k D_{q'q}^k(T) S_k^{q'}$. Using the expansion of the crystal field (4.3) together with (4.4) it is possible to obtain a system of equations for B_k^q by comparison of coefficients,

$$B_k^q = \frac{1}{g} \sum_{T \in \mathcal{G}} \sum_{q'} B_k^{q'} D_{q'q}^k(T). \quad (4.5)$$

Of course, (4.5) can not be solved for all B_k^q but it can be verified which coefficients depend on each other and which coefficients vanish. For the point group C_{3v} , which is the point group of the crystal field of a single holmium atom on a platinum (111) surface, the crystal field expansion is given by

$$V_{\text{cr}}(\theta, \phi) = B_0^0 S_0^0(\theta, \phi) + B_2^0 S_2^0(\theta, \phi) + B_4^0 S_4^0(\theta, \phi) + \\ + B_4^3 S_4^3(\theta, \phi) + B_6^0 S_6^0(\theta, \phi) + B_6^3 S_6^3(\theta, \phi) + B_6^6 S_6^6(\theta, \phi) + \dots \quad (4.6)$$

In the following it will be shown, how the crystal field expansion can be used to calculate the level splitting explicitly.

4.3.2. Solution of the eigenvalue equation

In the linear perturbation theory [111, pp. 203-207], the energy difference of the perturbed and the unperturbed system can be calculated from the eigenvalues of the matrix \tilde{A} with elements

$$A_{mm'} = \langle Jm | V_{\text{cr}} | Jm' \rangle. \quad (4.7)$$

It was the idea of STEVENS [112] to generalize the crystal field expansion (4.3) and to replace the tesseral harmonics S_k^q by associated operators \hat{O}_k^q acting on the vectors

$|Jm\rangle$. The operators \hat{O}_k^q can be expressed in terms of \hat{J}_z and the ladder operators \hat{J}_+ and \hat{J}_- , where the well known equations

$$\hat{J}_z |Jm\rangle = m |Jm\rangle, \quad \text{and} \quad \hat{J}_\pm |Jm\rangle = \sqrt{(J \mp m)(J \pm m + 1)} |Jm \pm 1\rangle \quad (4.8)$$

hold. Tables of the operators \hat{O}_k^q can be found in the literature, e.g. [113]. Instead of applying the operators \hat{O}_k^q , it was proposed by RYABOV [114] to directly calculate the matrix elements $\langle Jm | \hat{O}_k^q | Jm' \rangle$ using the equation

$$\begin{aligned} \langle Jm | \hat{O}_k^q | Jm' \rangle = & \frac{\alpha}{2F_{k,q}} \sum_{n=0}^{k-q} \left(\delta_{m',m+q} \left[\frac{(J-m)!(J+m+q)!}{(J+m)!(J-m-q)!} \right]^{1/2} + \right. \\ & \left. + \delta_{m',m-q} (-1)^{k-q-n} \left[\frac{(J+m)!(J-m+q)!}{(J-m)!(J+m-q)!} \right]^{1/2} \right) m^n a(k, q, n). \end{aligned} \quad (4.9)$$

Here, $F_{k,q}$ is given by the greatest common divisor of the coefficients $a(k, q, 0), \dots, a(k, q, q)$. Furthermore, $\alpha = 1$ for all q if k is an odd integer. If k is even, then $\alpha = 1$ or $\alpha = 1/2$ for even and odd q , respectively. In case that $q + n > k$ all coefficients $a(k, q, n)$ are equal to zero. For $q = k$ they are $a(k, k, 0) = 1$. The values of $a(k, q, n)$ have to be calculated recursively by

$$\begin{aligned} a(k, q-1, n) = & (2q+n-1)a(k, q, n-1) + \left[q(q-1) - \frac{m(m+1)}{2} \right] a(k, q, n) + \\ & + \sum_{\nu=1}^{k-q-n} (-1)^\nu \left[\binom{n+\nu}{n} J(J+1) - \binom{n+\nu}{n-1} - \binom{n+\nu}{n-2} \right] a(k, q, n+\nu). \end{aligned} \quad (4.10)$$

For the application of RYABOV's method three major advances can be pointed out. First, an exact representation of $|Jm\rangle$ is used and hence, the method can be applied easily for many electron systems. Second, in comparison to the classical method, no integration of wave functions is needed and hence, the method is much faster for large J . Third, the equations are exact and can be evaluated algebraically. Using (4.9) the $(2J+1)$ dimensional matrix of the Hamiltonian can be calculated via

$$H_{mm'} = \sum_{k=0}^{2J} \sum_{q=-k}^k B_k^q \langle Jm | \hat{O}_k^q | Jm' \rangle. \quad (4.11)$$

For a single holmium atom on platinum (111), the values of B_k^q were calculated from first principles by means of *Hutsepot* and can be found in Table 4.2. Details of the method are explained within the thesis of HOFFMANN [115]. Since $J = 8$ the Hamiltonian is represented by a 17×17 matrix. The eigenvalues and eigenvectors can

304. *Application of group theoretical methods to magnetic states of Ho on Pt(111)*

coefficients	value
B_2^0	-239 μeV
B_4^0	86 neV
B_4^3	293 neV
B_6^0	0.187 neV
B_6^3	-1.968 neV
B_6^6	0.630 neV

Table 4.2.: Crystal field parameters for a single holmium atom on a platinum (111) surface [Ge6, suppl. inf.].

be found using *Mathematica*. From the eigenvectors \mathbf{a}^i ($i = 1, \dots, 17$) it is possible calculate the expectation value $\langle J_z \rangle$ via

$$\langle J_z \rangle = \sum_{m=1}^{2J+1} |a_m^i|^2 \langle Jm | \hat{J}_z | Jm \rangle. \quad (4.12)$$

According to Figure 4.2, a large level splitting of ≈ 44.76 meV can be observed. By assigning the energy eigenvalues as well as the basis functions to a certain irreducible representation of C_{3v} , the prediction (4.1) can be confirmed. The ground state belongs to the irreducible representation E offering two states with $\langle J_z \rangle \approx +8$ and $\langle J_z \rangle \approx -8$, respectively.

To discuss the transition probability, the time-reversal operator \hat{T} can be taken into account, which commutes with the Hamiltonian \hat{H} , since no external magnetic field is applied. Moreover, it anti-commutes with the components of the angular momentum operator

$$\hat{H}\hat{T} - \hat{T}\hat{H} = 0 \quad \text{and} \quad \hat{J}_i\hat{T} + \hat{T}\hat{J}_i = 0. \quad (4.13)$$

The time-reversal operator is an anti-unitary operator, i.e.

$$\langle \phi | \psi \rangle = \langle \hat{T}\psi | \hat{T}\phi \rangle = \langle \hat{T}\phi | \hat{T}\psi \rangle^*. \quad (4.14)$$

Furthermore, an even number of electrons is discussed and it follows that $\hat{T}^2 = \hat{1}$. Denoting the two degenerate ground-states by $|\Psi_8\rangle$ and $|\Psi_{-8}\rangle$, it can be verified that

$$\langle \Psi_8 | \hat{J}_i | \Psi_{-8} \rangle = - \langle \hat{T}\Psi_8 | \hat{J}_i \hat{T} | \Psi_{-8} \rangle^* = - \langle \Psi_8 | \hat{J}_i | \Psi_{-8} \rangle^* = - \langle \Psi_{-8} | \hat{J}_i | \Psi_8 \rangle. \quad (4.15)$$

Hence, $\langle \Psi_8 | \hat{J}_i | \Psi_{-8} \rangle = 0$ and a direct transition between the two ground states is forbidden. Since a direct transition is forbidden, it follows that under real conditions, where $T > 0$ K, a long lifetime for staying in one of the two states $|\Psi_{-8}\rangle$ or $|\Psi_8\rangle$

E (meV)	$\langle J_z \rangle$	Γ
0.	7.9999	E^1
0.	-7.9999	E^1
7.7066	7.0000	E^2
7.7066	-7.0000	E^2
16.3256	0.	A_2^1
16.3259	0.	A_1^1
24.5807	4.9988	E^3
24.5807	-4.9988	E^3
31.7344	3.9967	E^4
31.7344	-3.9967	E^4
37.3103	0.	A_1^2
37.5407	0.	A_2^2
41.5094	1.9952	E^5
41.5094	-1.9952	E^5
43.9529	0.9973	E^6
43.9529	-0.9973	E^6
44.7653	0.	A_1^3

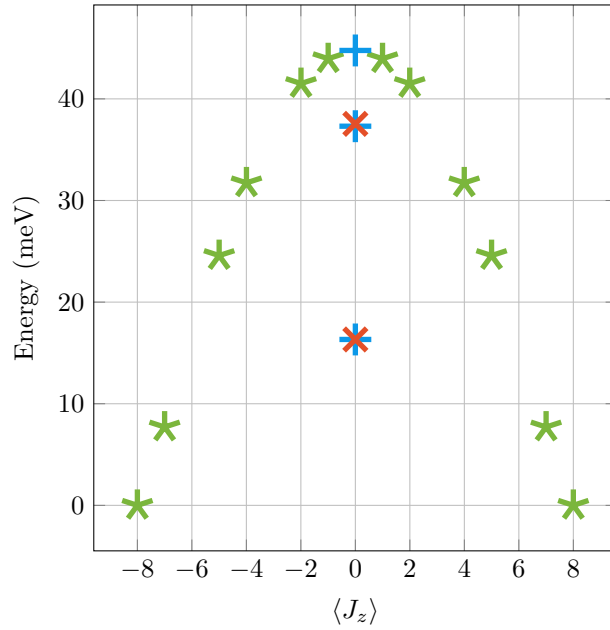


Figure 4.2.: Splitting of the $4f_{7/2}$ four particle state ($J = 8$) of a single holmium atom on a platinum (111) surface according to the crystal field. The colours identify the different irreducible representations of C_{3v} (blue $\equiv A_1$, red $\equiv A_2$, green $\equiv E$).

can be expected. This idea was proved within the experiment, where a lifetime of $\tau = (729 \pm 12)\text{s}$ was measured [Ge6]. Thus, it is possible to magnetize a single-holmium atom e.g. with a magnetic moment out of plane, which is related to the storage of one bit. Due to the long lifetime, this information will last for some minutes. Therefore, a single holmium atom on a platinum (111) surface can be seen as a single-bit data storage device.

324. Application of group theoretical methods to magnetic states of Ho on Pt(111)

Part II.

Relativistic extension of the Korringa-Kohn-Rostoker Green function method

5. Dirac equation and Green function

5.1. Dirac equation

With the formulation of the SCHRÖDINGER equation in 1926 [116, 117, 118, 119], a basic equation for the description of non-relativistic quantum systems was found. Nevertheless, the SCHRÖDINGER equation is not suitable for the description of electrons in heavy elements and furthermore for the description of spin and spin-orbit coupling. A differential equation for the investigation of electrons in relativistic quantum systems (including spin-orbit coupling) was proposed by DIRAC in 1928 [120],

$$i\hbar\frac{\partial}{\partial t}\Psi(\mathbf{r},t) = \left(c\tilde{\boldsymbol{\alpha}}\cdot\hat{\boldsymbol{\pi}} + \tilde{\beta}mc^2 + v(\mathbf{r},t)\right)\Psi(\mathbf{r},t). \quad (5.1)$$

The vector operator $\hat{\boldsymbol{\pi}} = \hat{\mathbf{p}} - e\mathbf{A}(\mathbf{r},t)$ is the commonly used combination of the momentum operator $\hat{\mathbf{p}} = -i\hbar\nabla$ and the vector potential $\mathbf{A}(\mathbf{r},t)$. The operator $\hat{H} = \left(c\tilde{\boldsymbol{\alpha}}\cdot\hat{\boldsymbol{\pi}} + \tilde{\beta}mc^2 + v(\mathbf{r},t)\right)$ is called HAMILTON operator, the potential $v(\mathbf{r},t)$ is the scalar potential and the abbreviations c and \hbar denote the speed of light as well as the PLANCK constant. Furthermore, the pseudo-vector $\tilde{\boldsymbol{\alpha}}$ consists of the matrices $\tilde{\alpha}_i$, which will be explained later within this section. For stationary problems, $\mathbf{A}(\mathbf{r},t) = \mathbf{A}(\mathbf{r})$ and $v(\mathbf{r},t) = v(\mathbf{r})$, the solution of the DIRAC equation can be written as $\Psi(\mathbf{r},t) = e^{-\frac{i}{\hbar}Wt}\phi(\mathbf{r})$. The four component spinor function $\phi(\mathbf{r})$ can be found by solving the stationary DIRAC equation

$$W\phi(\mathbf{r}) = \left(c\tilde{\boldsymbol{\alpha}}\cdot\hat{\boldsymbol{\pi}} + \tilde{\beta}mc^2 + v(\mathbf{r})\right)\phi(\mathbf{r}). \quad (5.2)$$

The problems investigated within this thesis are stationary, and hence the term DIRAC equation will be used for equation (5.2) in the following. For a classical free particle ($\mathbf{A}(\mathbf{r}) = 0$ and $v(\mathbf{r}) = 0$), the relativistic energy-momentum relation holds, which is given by

$$W^2 = c^2\mathbf{p}^2 + m^2c^4. \quad (5.3)$$

In analogy to classical relativistic mechanics, equation (5.3) can be taken into account to postulate a similar relation for the free HAMILTON operator,

$$\left(c\tilde{\boldsymbol{\alpha}}\cdot\hat{\mathbf{p}} + \tilde{\beta}mc^2\right)\left(c\tilde{\boldsymbol{\alpha}}\cdot\hat{\mathbf{p}} + \tilde{\beta}mc^2\right)\phi(\mathbf{r}) = W^2\phi(\mathbf{r}) = (c^2\hat{\mathbf{p}}^2 + m^2c^4)\phi(\mathbf{r}). \quad (5.4)$$

Hence, to ensure that equation (5.4) holds, the matrices $\tilde{\alpha}$ and $\tilde{\beta}$ have to fulfil the following properties,

$$\tilde{\alpha}_x^2 = \tilde{\alpha}_y^2 = \tilde{\alpha}_z^2 = \tilde{\beta}^2 = \tilde{I}, \quad (5.5)$$

$$\tilde{\beta}\tilde{\alpha} + \tilde{\alpha}\tilde{\beta} = 0, \quad (5.6)$$

and

$$\tilde{\alpha}_i\tilde{\alpha}_j + \tilde{\alpha}_j\tilde{\alpha}_i = 0 \quad i \neq j. \quad (5.7)$$

These relations are satisfied by the commonly used representation [106, p. 15]

$$\tilde{\alpha}_i = \begin{pmatrix} 0 & \tilde{\sigma}_i \\ \tilde{\sigma}_i & 0 \end{pmatrix} \quad \text{and} \quad \tilde{\beta} = \begin{pmatrix} \tilde{I}_2 & 0 \\ 0 & -\tilde{I}_2 \end{pmatrix}, \quad (5.8)$$

where $\tilde{\sigma}_i$ are the well known PAULI matrices

$$\tilde{\sigma}_x = \begin{pmatrix} 0 & 1 \\ 1 & 0 \end{pmatrix}, \quad \tilde{\sigma}_y = \begin{pmatrix} 0 & -i \\ i & 0 \end{pmatrix}, \quad \tilde{\sigma}_z = \begin{pmatrix} 1 & 0 \\ 0 & -1 \end{pmatrix}, \quad (5.9)$$

and \tilde{I}_2 the 2-dimensional identity matrix. In general, the representation of the matrices $\tilde{\alpha}_i$ and $\tilde{\beta}$ is not unique. Famous alternatives are given by the approach of WEYL for massless particles [121], which is important for the description of the weak interaction, or by the approach of MAJORANA, for particles without charge [122, 123]. The approach of MAJORANA has gained a lot of attention in recent years due to investigations of MAJORANA fermions in superconductors [124, 125, 126].

The solution $\phi(\mathbf{r})$ is a complex 4×1 column matrix. Since the absolute square of the solution can be identified as the probability density of the DIRAC particle, ϕ has to satisfy the condition

$$\langle \phi | \phi \rangle = \int_{\mathbb{R}^3} d^3\mathbf{r} [\phi(\mathbf{r})]^\dagger \phi(\mathbf{r}) = \int_{\mathbb{R}^3} d^3\mathbf{r} \sum_{i=1}^4 [\phi_i(\mathbf{r})]^* \phi_i(\mathbf{r}) \stackrel{!}{=} 1. \quad (5.10)$$

The scalar product $\langle \phi | \phi \rangle$ of equation (5.10) induces a norm of the solution $\phi(\mathbf{r})$, $|\phi(\mathbf{r})| = \sqrt{\langle \phi | \phi \rangle}$. To satisfy (5.10), each component of $\phi(\mathbf{r})$ has to be a square integrable function. Hence, each $\phi_i(\mathbf{r})$ can be seen as a vector of the space $L^2(\mathbb{R}^3)$, the space of the equivalence classes of the LEBESQUE space $\mathcal{L}^2(\mathbb{R}^3)$ (see [127, p. 17] or [128, pp. 25-26]). The HILBERT space \mathcal{H} of the solution $\phi(\mathbf{r})$ can be constructed from the direct sum of spaces $L^2(\mathbb{R}^3)$ [129, p. 6],

$$\mathcal{H} = L^2(\mathbb{R}^3) \oplus L^2(\mathbb{R}^3) \oplus L^2(\mathbb{R}^3) \oplus L^2(\mathbb{R}^3). \quad (5.11)$$

The HAMILTON operator $\hat{H} = \left(c \tilde{\alpha} \cdot \hat{\boldsymbol{\pi}} + \tilde{\beta} m c^2 + v(\mathbf{r}, t) \right)$ of equation (5.1) is a linear operator $\hat{H} : \mathcal{D}(\hat{H}) \rightarrow \mathcal{H}$, acting on a suitable domain $\mathcal{D}(\hat{H}) \subset \mathcal{H}$. The inverse of the operator $-\left(\hat{H} - W \right)$ is called the GREEN operator or the GREEN function, which will be introduced in the next section.

5.2. Green function

The introduction of the GREEN function is of practical importance for the KKR method. In the sense of operator algebra within a HILBERT space, the GREEN function $\hat{G}(W)$ can be defined as the inverse of the operator $(\hat{H} - W)$ with negative sign,

$$(\hat{H} - W) \hat{G}(W) = -\hat{I}. \quad (5.12)$$

Suppose the HAMILTON operator has a countable set of eigenfunctions $|n\rangle$ which form an orthonormal basis within the HILBERT space and fulfil the completeness relation $\sum_n |n\rangle \langle n| = \hat{I}$. It follows from the eigenvalue equation $\hat{H} |n\rangle = W_n |n\rangle$ that the HAMILTON operator can be written as $\hat{H} = \sum_n W_n |n\rangle \langle n|$. Rewriting equation (5.12) in the form

$$\left(\sum_n W_n |n\rangle \langle n| - W \hat{I} \right) \hat{G} = \sum_n (W_n - W) |n\rangle \langle n| \hat{G}(W) = -\hat{I}, \quad (5.13)$$

it can be verified that the GREEN function in operator form can be represented by

$$\hat{G}(W) = \sum_n \frac{|n\rangle \langle n|}{W - W_n}. \quad (5.14)$$

Equation (5.14) is called LEHMANN representation. In real space, the relativistic GREEN function is a 4×4 -matrix-valued function of the variables \mathbf{r} , \mathbf{r}' and W and equation (5.12) can be written as follows,

$$(\hat{H}(\mathbf{r}) - W \tilde{I}_4) \tilde{G}(\mathbf{r}, \mathbf{r}', W) = -\delta(\mathbf{r} - \mathbf{r}') \tilde{I}_4, \quad (5.15)$$

where \tilde{I}_4 denotes the 4-dimensional identity matrix. The GREEN function has the advantage that perturbations of the HAMILTON operator can be treated in an exact manner, as will be explained in 5.4. For this approach the GREEN function of a reference system has to be known. Therefore, the GREEN function of the free electron is very important and will be derived in the next section.

5.3. Relativistic free space Green function

During this section, it will be shown, that the relativistic free electron GREEN function ($v(\mathbf{r}) = 0$, $\mathbf{A}(\mathbf{r}) = 0$) can be derived from the non-relativistic GREEN function G_{NR}^0 [130, pp. 413], which is given by the following equation [43, p. 192],

$$G_{\text{NR}}^0(\mathbf{r}, \mathbf{r}', E) = -\frac{1}{4\pi} \frac{2m}{\hbar^2} \frac{e^{ik|\mathbf{r}-\mathbf{r}'|}}{|\mathbf{r}-\mathbf{r}'|}, \quad k = \frac{1}{\hbar} \sqrt{2mE}. \quad (5.16)$$

From the definition of the matrices $\tilde{\alpha}_i$ and $\tilde{\beta}$ according to equation (5.8), the square of the relativistic HAMILTON operator is given by

$$\hat{H}_0^2 = \left(c\tilde{\alpha} \cdot \hat{\mathbf{p}} + \tilde{\beta}mc^2 \right) \left(c\tilde{\alpha} \cdot \hat{\mathbf{p}} + \tilde{\beta}mc^2 \right) = (c^2\hat{\mathbf{p}}^2 + m^2c^4) \tilde{I}_4. \quad (5.17)$$

From the operator product $(\hat{H}_0 - W\tilde{I}_4)(\hat{H}_0 + W\tilde{I}_4) = (-\hbar^2\nabla^2c^2 + m^2c^4 - W^2) \tilde{I}_4$ it can be verified that an equation similar to the non-relativistic SCHRÖDINGER equation can be obtained. Hence, the following equation can be derived for the non-relativistic GREEN function,

$$\begin{aligned} \frac{1}{2mc^2} (\hat{H}_0 - W\tilde{I}_4) (\hat{H}_0 + W\tilde{I}_4) G_{\text{NR}}^0(\mathbf{r}, \mathbf{r}', E) \\ = \left(-\frac{\hbar^2}{2m} \nabla^2 - E \right) \tilde{I}_4 G_{\text{NR}}^0(\mathbf{r}, \mathbf{r}', E) = -\delta(\mathbf{r} - \mathbf{r}') \tilde{I}_4. \end{aligned} \quad (5.18)$$

In the above equation, the energy E is an abbreviation for

$$E = \frac{W^2 - m^2c^4}{2mc^2}. \quad (5.19)$$

From equation (5.18) it can be seen (in comparison to (5.15)) that the relativistic GREEN function for a free electron is given by

$$\tilde{G}_0(\mathbf{r}, \mathbf{r}', W) = \frac{1}{2mc^2} (\hat{H}_0 + W\tilde{I}_4) G_{\text{NR}}^0(\mathbf{r}, \mathbf{r}', E). \quad (5.20)$$

5.4. The Dyson and Lippmann-Schwinger equation

A great advantage of GREEN function methods is given by the fact that perturbations can be treated using the DYSON and the LIPPMANN-SCHWINGER equation [43, pp. 31-38]. A short derivation of both equations will be given within this section. The approach is valid for the non-relativistic case as well as for the relativistic case. For brevity, all equations during this section are written in operator form.

Suppose the GREEN function of a reference system with HAMILTON operator \hat{H}_0 is known,

$$(\hat{H}_0 - W) \hat{G}_0 = -\hat{I}. \quad (5.21)$$

Let ΔV be a small perturbation then the perturbed Hamiltonian is given by $\hat{H} = \hat{H}_0 + \Delta V$. By taking the definition of the GREEN function \hat{G} in equation (5.12) together with (5.21), the following relation can be derived,

$$-\hat{I} = (\hat{H}_0 - W + \Delta V) \hat{G} = -\hat{G}_0^{-1} \hat{G} + \Delta V \hat{G}. \quad (5.22)$$

Rearranging equation (5.22) gives the so-called DYSON equation,

$$\hat{G} = \hat{G}_0 + \hat{G}_0 \Delta V \hat{G}. \quad (5.23)$$

The DYSON equation is an implicit equation for the operator \hat{G} that can be solved self-consistently via $\hat{G} = \hat{G}_0 + \hat{G}_0 \Delta V \hat{G}_0 + \hat{G}_0 \Delta V \hat{G}_0 \Delta V \hat{G}_0 + \dots$. By introducing the scattering path operator $\hat{T} = \Delta V + \Delta V \hat{G}_0 \Delta V + \dots$, equation (5.23) can be rewritten as an explicit operator equation,

$$\hat{G} = \hat{G}_0 + \hat{G}_0 \hat{T} \hat{G}_0. \quad (5.24)$$

In the next step it will be shown, how an approximation for the perturbed wave function can be found. It is assumed, that a solution ϕ_0 for the unperturbed system is known, which fulfils the equation $(\hat{H}_0 - W)\phi_0 = 0$. The solution of the perturbed system ϕ can be constructed from the unperturbed solution via,

$$\phi = \phi_0 + \delta\phi. \quad (5.25)$$

Using the definition $\hat{G}_0 = -(\hat{H}_0 - W)^{-1}$ and the eigenvalue equation

$$(\hat{H}_0 - W + \Delta V)\phi = 0, \quad (5.26)$$

the following relation can be found,

$$(\hat{H}_0 - W + \Delta V)(\phi_0 + \delta\phi) = \Delta V\phi - \hat{G}_0^{-1}\delta\phi = 0. \quad (5.27)$$

With the help of equation (5.27) the so-called LIPPMANN-SCHWINGER equation can be formulated,

$$\phi = \phi_0 + \hat{G}_0 \Delta V \phi. \quad (5.28)$$

The LIPPMANN-SCHWINGER equation is often used to solve the full-potential single-site scattering problem by taking into account the solution of the spherically symmetric problem as ϕ_0 and treating the non-spherical parts of the potential as a perturbation ΔV [7, 30]. From this approach it is possible to construct a set of integral equations, which can be solved iteratively, via

$$\phi = \phi_0 + \hat{G}_0 \Delta V \phi_0 + \hat{G}_0 \Delta V \hat{G}_0 \Delta V \phi_0 + \hat{G}_0 \Delta V \hat{G}_0 \Delta V \hat{G}_0 \Delta V \phi_0 + \dots \quad (5.29)$$

The iterative solution of the LIPPMANN-SCHWINGER equation is also known as BORN-series.

6. Relativistic scattering theory

6.1. Introduction

Within this chapter, basics of the relativistic multiple-scattering theory will be explained, which are needed for the implementation of a relativistic KKR method. The main formalism of the relativistic KKR method is similar to the non-relativistic KKR method, which was introduced shortly within Section 2. It was shown that the electron density, which is the main quantity within methods based on density functional theory, can be obtained from the trace of the multiple-scattering GREEN function. After decomposing the space into distinct scattering centres, the multiple-scattering GREEN function itself can be constructed from the regular and the irregular single-site scattering solutions at each scattering centre within the unit cell. Therefore, the main focus of the next sections will be the accurate solution of the single-site scattering problem. First of all, it will be shown how the KOHN-SHAM-DIRAC equation, which is a partial differential equation can be transferred into a set of coupled first-order ordinary differential equations by expanding the solution into spin-angular functions. To treat non-spherical potentials within this approach it is necessary to expand the potential term within the KOHN-SHAM-DIRAC equation into spherical harmonics, which will be explained afterwards. For each scattering centre it is assumed that the potential is non-zero within a finite distance and zero outside. Therefore, the solution of the DIRAC equation for free electrons is important for the normalization of the regular and the irregular single-site scattering solution, by defining two linearly independent solutions outside of the scattering centre. In connection to the general theory of the single-site scattering problem, the numerical solution of the underlying differential equations will be illustrated. Finally, it will be explained how the relativistic multiple-scattering GREEN function can be constructed. In contrast to the non-relativistic theory a so-called left-hand side solution of the single-site scattering problem is necessary for this construction. It will be explained how such a solution can be obtained. Last but not least, a relativistic formulation of LLOYDS equation will be derived which can be used for an accurate integration over the density of states to estimate the FERMI energy. If the FERMI energy is known, the charge density can be calculated analogously to equation (2.11).

6.2. The radial Dirac equation for an arbitrary single-site scattering potential

The origins of the formulation of a relativistic density functional theory go back to the work of MACDONALD and VOSKO [131] and RAMANA and RAJAGOPAL [132] in 1979. Using atomic RYDBERG units ($\hbar = 1$, $m = \frac{1}{2}$, $c = \frac{2}{\alpha} \approx 274$) the corresponding DIRAC or KOHN-SHAM-DIRAC equation for a magnetic system [3, 133] is given by

$$\left[-ic \tilde{\boldsymbol{\alpha}} \cdot \nabla + \frac{1}{2} \tilde{\beta} c^2 + \tilde{I}_4 V_{\text{eff}}(\mathbf{r}) + \tilde{\beta} \tilde{\boldsymbol{\sigma}} \cdot \mathbf{B}(\mathbf{r}) + \tilde{\boldsymbol{\alpha}} \cdot \mathbf{A}(\mathbf{r}) \right] \phi_q(\mathbf{r}) = W \phi_q(\mathbf{r}). \quad (6.1)$$

Here, the quantum number q is an abbreviation for (κ, μ) . Instead of using the vector operator $\hat{\boldsymbol{\pi}} = \hat{\mathbf{p}} - e\mathbf{A}(\mathbf{r}, t)$ it is assumed in the following that the magnetic field $\mathbf{B}(\mathbf{r}) = \nabla \times \mathbf{A}(\mathbf{r})$ is only coupling to the electron spin and orbital magnetism is neglected [131, 134]. Using this approximation the DIRAC equation for an arbitrary potential $\tilde{V}(\mathbf{r}) = \tilde{I}_4 V_{\text{eff}}(\mathbf{r}) + \tilde{\beta} \tilde{\boldsymbol{\sigma}} \cdot \mathbf{B}$ is given by

$$\left[-ic \tilde{\boldsymbol{\alpha}} \cdot \nabla + \frac{1}{2} \tilde{\beta} c^2 + \tilde{V}(\mathbf{r}) \right] \phi_q(\mathbf{r}) = W \phi_q(\mathbf{r}). \quad (6.2)$$

By introducing the spin-orbit operator \tilde{K} , the kinetic energy term $-ic \tilde{\boldsymbol{\alpha}} \cdot \nabla$ can be transferred to spherical polar coordinates [130, pp. 228] and the DIRAC equation can be written as

$$\left[-ic \tilde{\boldsymbol{\alpha}} \cdot \mathbf{e}_r \left(\frac{\partial}{\partial r} + \frac{1}{r} - \frac{1}{r} \tilde{\beta} \tilde{K} \right) + \frac{1}{2} \tilde{\beta} c^2 + \tilde{V}(\mathbf{r}) \right] \phi_q(\mathbf{r}) = W \phi_q(\mathbf{r}). \quad (6.3)$$

A solution for (6.3) can be found by expanding $\phi_q(\mathbf{r})$ by means of the spin angular functions $\chi_q(\hat{\mathbf{r}})$,

$$\phi_q(\mathbf{r}) = \sum_{q'} \begin{pmatrix} g_{q'q}(r) \chi_{q'}(\hat{\mathbf{r}}) \\ i f_{q'q}(r) \chi_{\bar{q}'}(\hat{\mathbf{r}}) \end{pmatrix}, \quad (6.4)$$

with

$$\chi_q(\hat{\mathbf{r}}) = \sum_{m_s} C_q^{m_s} Y_l^{\mu - m_s}(\hat{\mathbf{r}}) \boldsymbol{\xi}_{m_s}. \quad (6.5)$$

In the above equation, $C_q^{m_s}$ is an abbreviation for the CLEBSCH-GORDAN-coefficients, $C_q^{m_s} = C(l, 1/2, j; (\mu - m_s), m_s)$, which can be found in Table 6.1. Furthermore, $\boldsymbol{\xi}_{m_s}$ are the PAULI spinors with components $\xi_{m_s}^\alpha = \delta_{\alpha m_s}$, $\bar{q} = (-\kappa, \mu)$ and $Y_l^m(\hat{\mathbf{r}})$ denote the complex spherical harmonics [Ge1, Appendix].

For compactness, the matrix $\tilde{\sigma}_r$ is introduced as follows,

$$\tilde{\boldsymbol{\alpha}} \cdot \mathbf{e}_r = \begin{pmatrix} 0 & \tilde{\sigma}_r \\ \tilde{\sigma}_r & 0 \end{pmatrix}, \quad \tilde{\sigma}_r = \tilde{\boldsymbol{\sigma}} \cdot \mathbf{e}_r. \quad (6.6)$$

j	κ	$m_s = -\frac{1}{2}$	$m_s = \frac{1}{2}$
$l - \frac{1}{2}$	l	$\sqrt{\frac{l+\mu+\frac{1}{2}}{2l+1}}$	$-\sqrt{\frac{l-\mu+\frac{1}{2}}{2l+1}}$
$l + \frac{1}{2}$	$-l - 1$	$\sqrt{\frac{l-\mu+\frac{1}{2}}{2l+1}}$	$\sqrt{\frac{l+\mu+\frac{1}{2}}{2l+1}}$

Table 6.1.: CLEBSCH-GORDAN-coefficients according to STRANGE [130, p. 57].

Using the approach (6.4) for the DIRAC equation (6.2) two coupled differential equations arise,

$$\text{I:} \quad c\tilde{\sigma}_r \left(\frac{\partial}{\partial r} + \frac{1}{r} + \frac{\tilde{K}}{r} \right) \sum_{q'} f_{q'q} \chi_{q'} + \left(\tilde{V}^+ + \frac{c^2}{2} \right) \sum_{q'} g_{q'q} \chi_{q'} = W \sum_{q'} g_{q'q} \chi_{q'}, \quad (6.7)$$

$$\text{II:} \quad -c\tilde{\sigma}_r \left(\frac{\partial}{\partial r} + \frac{1}{r} - \frac{\tilde{K}}{r} \right) \sum_{q'} g_{q'q} \chi_{q'} + \left(\tilde{V}^- - \frac{c^2}{2} \right) \sum_{q'} f_{q'q} \chi_{q'} = W \sum_{q'} f_{q'q} \chi_{q'}. \quad (6.8)$$

For the potential, the abbreviation $\tilde{V}^\pm = \tilde{I}_2 V_{\text{eff}}(\mathbf{r}) \pm \tilde{\boldsymbol{\sigma}} \cdot \mathbf{B}(\mathbf{r})$ is used. The spin angular functions χ_q are eigenfunctions of the spin-orbit operator \tilde{K} with eigenvalues $-\kappa$ ($\tilde{K}\chi_q = -\kappa\chi_q$) and the operator $\tilde{\sigma}_r$ has the property $\tilde{\sigma}_r \chi_q(\hat{\mathbf{r}}) = -\chi_{\bar{q}}(\hat{\mathbf{r}})$ [130, p. 48, p. 59]. To get rid of the spin angular functions, the orthogonality $\langle \chi_q | \chi_{q'} \rangle = \delta_{q'q}$ can be taken into account. By multiplication of $\chi_{q''}^\dagger$ from the left to equation (6.7) and of $\chi_{\bar{q}''}^\dagger$ to equation (6.8) and integration over angles one finally ends up with

$$\text{I:} \quad -c \left(\frac{\partial}{\partial r} + \frac{1}{r} - \frac{\kappa'}{r} \right) f_{q'q} + \frac{c^2}{2} g_{q'q} + \sum_{q''} V_{q'q''}^+ g_{q''q} = W g_{q'q}, \quad (6.9)$$

$$\text{II:} \quad c \left(\frac{\partial}{\partial r} + \frac{1}{r} + \frac{\kappa'}{r} \right) g_{q'q} - \frac{c^2}{2} f_{q'q} + \sum_{q''} V_{\bar{q}'\bar{q}''}^- f_{q''q} = W f_{q'q}. \quad (6.10)$$

The equations (6.9) and (6.10) define an infinitely large coupled system of first-order ordinary differential equations. The components of the wave functions $f_{q'q}$ and $g_{q'q}$ are coupled via the potential matrices \tilde{V}^\pm . The calculation of the matrix elements $V_{q'q''}^\pm = \langle \chi_q | \tilde{V}^\pm | \chi_{q'} \rangle$ will be illustrated in the next section. A numerical approach to the solution of (6.9) and (6.10) will be discussed afterwards in Section 6.5.

6.3. Treatment of the non-spherical potential

6.3.1. Shape-truncation function

To simplify the explanations within this section, it is assumed that the unit cell of the crystal under consideration consists of one single atom. A similar approach can be formulated for larger unit cells, where instead of the WIGNER-SEITZ cell the VORONOI cell around each atom has to be taken into account. The basic idea of the KKR method is based on a decomposition of a crystal into distinct atomic regions [3]. Originally, this was done by means of the so-called muffin-tin approximation, where a non-overlapping spherical potential was assumed at each atomic site and the interstitial region was chosen to be constant [43, pp. 24-26]. Another spherical approach is given by the atomic sphere approximation [135, 136], where the volume of the atomic spheres is chosen such that it is equal to the volume of the WIGNER-SEITZ cell. Within a full-potential approximation, the real shape of the WIGNER-SEITZ cell is taken into account, as it is illustrated in Figure 6.1.

In the first step of the KKR method it is necessary to solve the differential equations (6.9) and (6.10) of the previous section at each atomic site of the unit cell,

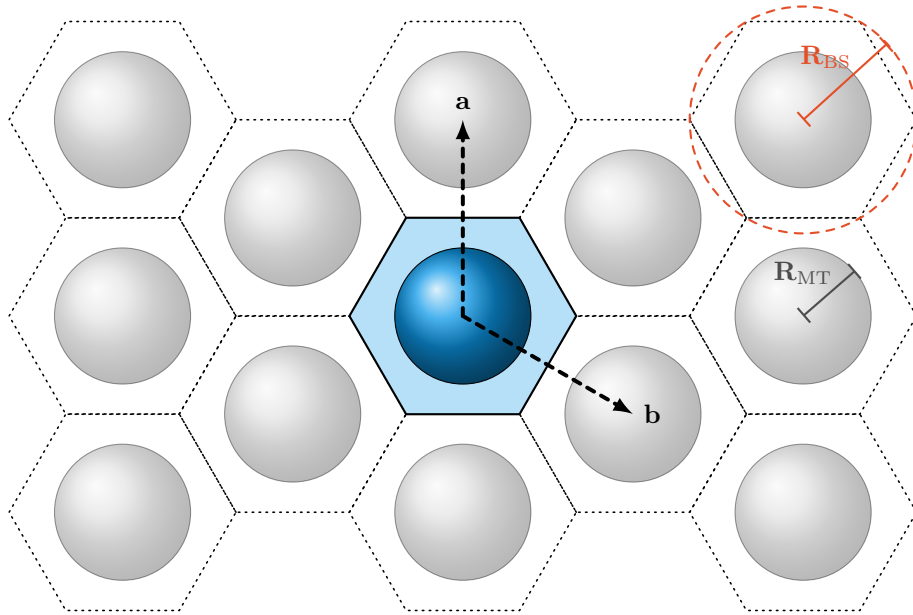


Figure 6.1.: Illustration of a hexagonal two-dimensional lattice with lattice vectors \mathbf{a} and \mathbf{b} , the hexagonal WIGNER-SEITZ cell at each site (blue), the muffin-tin spheres with the muffin-tin radius \mathbf{R}_{MT} and the circumscribing sphere about the WIGNER-SEITZ cell (orange) with the radius \mathbf{R}_{BS} .

which is called the solution of the single-site scattering problem. Since the atomic regions are chosen to be disjoint, the potential $\tilde{V}(\mathbf{r})$ in the DIRAC equation is chosen to be non-zero within the WIGNER-SEITZ cell and to be zero outside. To satisfy that the potential is equal to zero outside of the cell, the scattering-potential $\tilde{V}(\mathbf{r}) = \tilde{U}(\mathbf{r}) \Theta(\mathbf{r})$ is constructed as the product of the non-spherical effective potential $\tilde{U}(\mathbf{r}) = U_{\text{eff}}(\mathbf{r}) \tilde{I}_2 \pm \tilde{\boldsymbol{\sigma}} \cdot \mathbf{B}'_{\text{eff}}(\mathbf{r})$ which can be calculated from the charge density at each iteration of the self-consistency cycle and the so called shape-truncation function $\Theta(\mathbf{r})$ [137, pp. 55], which is given by

$$\Theta(\mathbf{r}) = \begin{cases} 1 & \text{for } \mathbf{r} \text{ inside of the cell} \\ 0 & \text{for } \mathbf{r} \text{ outside of the cell} \end{cases} . \quad (6.11)$$

Both, the non-spherical effective potential $\tilde{U}(\mathbf{r})$ as well as the shape-truncation function $\Theta(\mathbf{r})$ can be evaluated into spherical harmonics [85, 86, 30], via

$$\Theta(\mathbf{r}) = \sum_{l,m} \theta_{lm}(r) Y_l^m(\vartheta, \varphi), \quad \text{and} \quad \tilde{U}(\mathbf{r}) = \sum_{l,m} \tilde{U}_{lm}(r) Y_l^m(\vartheta, \varphi). \quad (6.12)$$

Of course, the same can be done with the scattering-potential $\tilde{V}(\mathbf{r})$, which gives the equation

$$\tilde{V}(\mathbf{r}) = \sum_{l,m} \tilde{V}_{lm}(r) Y_l^m(\vartheta, \varphi). \quad (6.13)$$

From (6.13) it can be verified that the expansion coefficients \tilde{V}_{lm} can be calculated via $\tilde{V}_{lm}(r) = \int d\Omega [Y_l^m(\vartheta, \varphi)]^* \tilde{U}(\mathbf{r}) \Theta(\mathbf{r})$ and hence, it is possible to obtain the following construction of the potential $\tilde{V}_{lm}(r)$ from the expansion coefficients $\tilde{U}_{lm}(r)$ and $\theta_{lm}(r)$ of the non-spherical effective potential and the shape-truncation function, respectively,

$$\tilde{V}_{lm}(r) = \sum_{l',m'} \sum_{l'',m''} \int d\Omega [Y_l^m(\vartheta, \varphi)]^* Y_{l'}^{m'}(\vartheta, \varphi) Y_{l''}^{m''}(\vartheta, \varphi) \theta_{l'm'}(r) \tilde{U}_{l''m''}(r) \quad (6.14)$$

$$= \sum_{l',m'} \sum_{l'',m''} G_{l'l''}^{m,m',m''} \theta_{l'm'}(r) \tilde{U}_{l''m''}(r). \quad (6.15)$$

Here, $G_{l'l''}^{m,m',m''}$ denote the GAUNT coefficients $G_{l'l''}^{m,m',m''} = \int d\Omega (Y_l^m)^* Y_{l'}^{m'} Y_{l''}^{m''}$, which can be obtained either algebraically by using WIGNER-3J-symbols [138, equation (17)] or numerically by means of the LEBEDEV quadrature formula [139].

In general, the expansion coefficients $\theta_{lm}(r)$ of the shape-truncation function have to be calculated from the integral,

$$\theta_{lm}(r) = \int_0^\pi d\vartheta \sin \vartheta \int_0^{2\pi} d\varphi [Y_l^m(\vartheta, \varphi)]^* \Theta(\mathbf{r}). \quad (6.16)$$

Since the shape function takes on values either 1 or 0, depending if the vector $\mathbf{r} = (r, \vartheta, \varphi)$ lies inside the WIGNER-SEITZ cell or not, the value of the integral can be obtained by specifying the range of integration over ϑ and φ for each value of r . By continuously increasing r it can be verified that the coefficients $\theta_{lm}(r)$ will show a kink if the sphere with radius r reaches a plane or an edge of the WIGNER-SEITZ cell. Those particular values of r are called critical radii. An illustration of the critical radii for a 2-dimensional rectangular lattice can be found in Figure 6.2. It was shown by ZAHARIOUDAKIS [140, 141] that it is possible to obtain analytic expressions for the expansion coefficients of the shape truncation function for cubic and hexagonal cells. The numerical evaluation of the coefficients was discussed e.g. by STEFANO, AKAI and ZELLER [85] and by STEFANO and ZELLER [86].

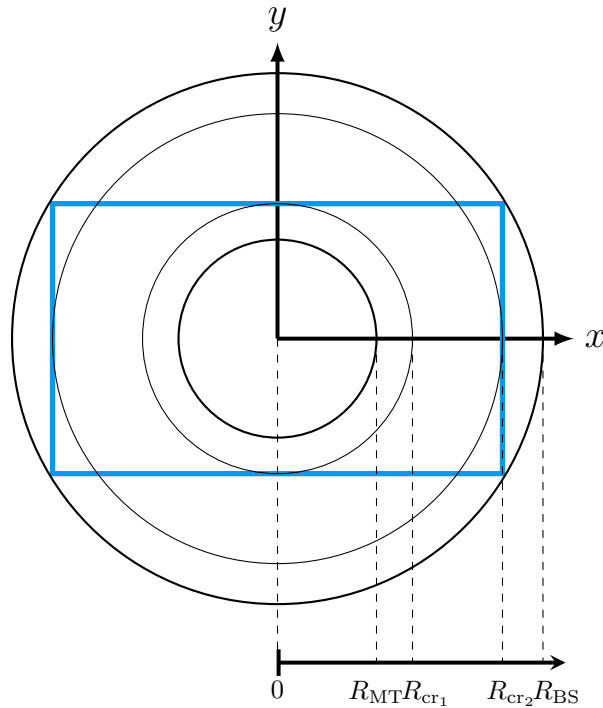


Figure 6.2.: Illustration of the critical radii R_{cr_i} for the construction of the shape-truncation function. R_{MT} denotes the muffin tin radius and R_{BS} is the radius of the circumscribing sphere of the cell.

6.3.2. The potential matrix

In Section 6.2 the elements of the potential matrix $V_{q'q''}^{\pm} = \langle \chi_q | \tilde{V}^{\pm} | \chi_{q'} \rangle$ were defined within the formulation of the differential equations (6.9) and (6.10) for the relativistic

single-site scattering problem. In the following, an exact equation for $V_{q'q''}^\pm$ will be derived. For a general effective magnetic field, the potential within the DIRAC equation can be written as a linear-combination of the effective electrostatic potential V_{eff} and the effective magnetic field $\mathbf{B}_{\text{eff}}(\mathbf{r})$,

$$\tilde{V}^\pm(\mathbf{r}) = V_{\text{eff}}(\mathbf{r})\tilde{I}_2 \pm \tilde{\boldsymbol{\sigma}} \cdot \mathbf{B}_{\text{eff}}(\mathbf{r}). \quad (6.17)$$

As explained in the previous section, after taking into account the shape-truncation function, the potential can be expanded into spherical harmonics,

$$\tilde{V}^\pm(\mathbf{r}) = \sum_{l,m} \left[V_L(r)\tilde{I}_2 \pm \tilde{\sigma}_x B_{x,L}(r) \pm \tilde{\sigma}_y B_{y,L}(r) \pm \tilde{\sigma}_z B_{z,L}(r) \right] Y_{lm}(\hat{\mathbf{r}}). \quad (6.18)$$

According to equation (6.5) the spin-angular functions are defined as a linear combination of the spherical harmonics $Y_l^m(\hat{\mathbf{r}})$ and the PAULI spinors $\boldsymbol{\xi}_{m_s}$. Using this definition, the matrix element $\langle \boldsymbol{\chi}_q | \tilde{V}^\pm | \boldsymbol{\chi}_{q'} \rangle$ is given by

$$\begin{aligned} V_{qq'}^\pm(r) &= \sum_{l''m''} \sum_{m_s} \sum_{m'_s} C_q^{m_s} C_{q'}^{m'_s} (\boldsymbol{\xi}^{m_s})^T \times \\ &\quad \times \left[V_{l''m''}(r)\tilde{I}_2 \pm \tilde{\sigma}_x B_{x,L''}(r) \pm \tilde{\sigma}_y B_{y,L''}(r) \pm \tilde{\sigma}_z B_{z,L''}(r) \right] \boldsymbol{\xi}^{m'_s} \times \\ &\quad \times \int d\Omega \left(Y_l^{\mu-m_s}(\hat{\mathbf{r}}) \right)^* Y_{l''}^{\mu''}(\hat{\mathbf{r}}) Y_{l'}^{\mu'-m'_s}(\hat{\mathbf{r}}). \end{aligned} \quad (6.19)$$

Within the above equation, expressions like $\tilde{\sigma}_i \boldsymbol{\xi}^{m_s}$ occur, where a PAULI matrix $\tilde{\sigma}_i$ acts on a PAULI spinor $\boldsymbol{\xi}^{m_s}$. Hence, it is necessary to verify the following relations,

$$\tilde{\sigma}_x \boldsymbol{\xi}^{m_s} = \boldsymbol{\xi}^{-m_s}, \quad \tilde{\sigma}_y \boldsymbol{\xi}^{m_s} = 2i m_s \boldsymbol{\xi}^{-m_s}, \quad \text{and} \quad \tilde{\sigma}_z \boldsymbol{\xi}^{m_s} = 2m_s \boldsymbol{\xi}^{m_s}. \quad (6.20)$$

By using the orthogonality of the PAULI spinors $\boldsymbol{\xi}^{m_s} \cdot \boldsymbol{\xi}^{m'_s} = \delta_{m_s m'_s}$, the GAUNT coefficients $G_{l,l',l''}^{m,m',m''} = \int d\Omega (Y_l^m)^* Y_{l'}^{m'} Y_{l''}^{m''}$ and the above equations, it is possible to obtain

$$\begin{aligned} V_{qq'}^\pm(r) &= \sum_{L''} \sum_{m_s} \sum_{m'_s} C_q^{m_s} C_{q'}^{m'_s} \left[(V_{L''}(r) \pm 2m'_s B_{z,L''}(r)) \delta_{m_s, m'_s} \right. \\ &\quad \left. \pm (B_{x,L''}(r) + 2i m'_s B_{y,L''}(r)) \delta_{m_s, -m'_s} \right] G_{l,l',l''}^{\mu-m_s, m''} \mu' - m'_s. \end{aligned} \quad (6.21)$$

Equation (6.21) was implemented within the computer program *Hutsepot* to calculate the matrix elements $V_{qq'}^\pm$ of the potential matrix. For an effective electrostatic potential $V_{\text{eff}}(\mathbf{r})$ and an effective magnetic field $\mathbf{B}_{\text{eff}}(\mathbf{r}) = (0, 0, B_{\text{eff}}(\mathbf{r}))^T$ pointing into the z -direction, equation (6.21) can be simplified to the following form,

$$V_{qq'}^\pm(r) = \sum_{L''} \sum_{m_s} C_q^{m_s} C_{q'}^{m'_s} [V_{L''}(r) \pm 2m_s B_{L''}(r)] G_{l,l',l''}^{(\mu-m_s) m''} (\mu' - m_s). \quad (6.22)$$

In many cases it is sufficient to assume that the effective magnetic field is collinear within each atomic region. In this case, it is possible to define the local coordinate system in such a way that the magnetic field runs parallel to the z -axis of the Cartesian coordinate system. Hence, equation (6.22) can be applied to calculate the potential matrix. It was shown by SANDRATSKII [142, 143] and later by YAVORSKY *et al.* [144] and LOUNIS *et al.* [145] that this approach can even be used for non-collinear magnetic systems, by introducing different local coordinate systems at each atomic site.

6.4. Solution of the free Dirac equation and matching conditions

According to the previous sections, the single-site scattering potential was defined to be non-zero inside of the WIGNER-SEITZ cell and zero outside. Therefore, it is important to know the solution of the radial DIRAC equation for a free electron, in order to have a correct description for the exterior of the cell.

Starting from the differential equations (6.9) and (6.10) and setting $\tilde{V}^+ = \tilde{V}^- = 0$, it is possible to formulate a second order differential equation for $g_{q'q}$, which can be denoted by g_κ in the following, since it is diagonal in q and q' and independent of μ ,

$$g_\kappa''(r) = -\frac{2}{r}g_\kappa'(r) + \frac{\kappa(\kappa+1)}{r^2}g_\kappa(r) + \frac{1}{c^2\hbar^2}(W^2 - m^2c^4)g_\kappa(r). \quad (6.23)$$

According to MORSE and FESHBACH [146, p. 622, p. 1465], the solution of the differential equation (6.23) is given by the spherical BESSEL and NEUMANN functions,

$$g_\kappa(r) = C_1j_\kappa(kr) + C_2n_\kappa(kr). \quad (6.24)$$

Analogously, a solution of the small component $f_\kappa(r)$ can be obtained,

$$f_\kappa(r) = \frac{c\hbar k}{W + mc^2}(C_1j_{\kappa-1}(kr) + C_2n_{\kappa-1}(kr)). \quad (6.25)$$

The spherical BESSEL and NEUMANN functions can be defined via the BESSEL function of the first kind [146, p. 622],

$$j_l(r) = \sqrt{\frac{2\pi}{r}}J_{l+1/2} \quad \text{and} \quad n_l(r) = (-1)^{l+1}\sqrt{\frac{2\pi}{r}}J_{-l-1/2} \quad (6.26)$$

Therefore, the common relations

$$j_{-l-1} = (-1)^{l+1}n_l \quad \text{and} \quad n_{-l-1} = (-1)^l j_l \quad (6.27)$$

can be evaluated. Since the quantum number κ can take on values either $\kappa = l$ or $\kappa = -l - 1$ it is necessary to distinguish between both cases to formulate a general l -dependent solution.

Case 1: $\kappa = l$

Since $\kappa \neq 0$, it is possible to assume $l \geq 1$ for the case $\kappa = l$. The l -dependent result is similar to (6.24) and (6.25),

$$g_\kappa(r) = g_l(r) = C_1 j_l(kr) + C_2 n_l(kr), \quad (6.28)$$

$$f_\kappa(r) = f_l(r) = \frac{c\hbar k}{W + mc^2} (C_1 j_{l-1}(kr) + C_2 n_{l-1}(kr)). \quad (6.29)$$

Case 2: $\kappa = -l - 1$

For the case $\kappa = -l - 1$ the relations (6.27) can be applied to obtain

$$g_\kappa(r) = g_{-l-1}(r) = (-1)^l (C_2 j_l(kr) - C_1 n_l(kr)), \quad (6.30)$$

$$f_\kappa(r) = f_{-l-1}(r) = \frac{c\hbar k}{W + mc^2} (-1)^l (-C_2 j_{l+1}(kr) + C_1 n_{l+1}(kr)). \quad (6.31)$$

The general solution

To summarize the results, it is common to introduce the quantities $S_\kappa = \frac{\kappa}{|\kappa|}$ and $\bar{l} = l - S_\kappa$ [34, p.105]. Doing so, the general form of the free solutions of the radial DIRAC equation is written as follows,

$$g_\kappa(r) = (A j_l(kr) + S_\kappa B n_l(kr)), \quad (6.32)$$

$$f_\kappa(r) = \frac{c\hbar k S_\kappa}{W + mc^2} (A j_{\bar{l}}(kr) + S_\kappa B n_{\bar{l}}(kr)). \quad (6.33)$$

During the development of the KKR method, at least two different choices for the constants A and B in the above equations have been established for the construction of the regular and irregular single-site scattering solutions. They are referred to as *Oak Ridge-Bristol convention*, and *Jülich convention* [3]. To distinguish both conventions, the single-site scattering solutions are denoted differently. For the *Oak Ridge-Bristol convention* the notations $\mathbf{Z}_q(\mathbf{r})$ and $\mathbf{J}_q(\mathbf{r})$ are commonly used for the regular and the irregular scattering solution, respectively, whereas $\mathbf{R}_q(\mathbf{r})$ and $\mathbf{H}_q(\mathbf{r})$ are taken within the *Jülich convention*.

Matching I: Oak Ridge-Bristol convention

The first matching condition was used successfully i.e. by FAULKNER and STOCKS [147] and contains the inverse of the single-site t-matrix. According to HUHNE *et al.* [30], the fully-relativistic regular scattering solution $\mathbf{Z}_q^{\text{outside}}(\mathbf{r})$ at the outside of the WIGNER-SEITZ cell is given by

$$\mathbf{Z}_q^{\text{outside}}(\mathbf{r}) = \sum_{q'} \left[\begin{pmatrix} j_{l'}(kr) \chi_{q'}(\hat{\mathbf{r}}) \\ e_{q'} j_{\bar{l}'}(kr) \chi_{q'}(\hat{\mathbf{r}}) \end{pmatrix} t_{q'q}^{-1} - ik \begin{pmatrix} h_{l'}(kr) \chi_{q'}(\hat{\mathbf{r}}) \\ e_{q'} h_{\bar{l}'}(kr) \chi_{q'}(\hat{\mathbf{r}}) \end{pmatrix} \delta_{q'q} \right]. \quad (6.34)$$

Here, $h_l(r)$ denotes the spherical HANKEL function of the first kind $h_l(r) = j_l(r) + in_l(r)$. The corresponding irregular scattering solution $\mathbf{J}_q^{\text{outside}}(\mathbf{r})$ can be constructed from the spherical BESSEL function [30],

$$\mathbf{J}_q^{\text{outside}}(\mathbf{r}) = \begin{pmatrix} j_l(kr)\chi_q(\hat{\mathbf{r}}) \\ e_q j_{\bar{l}}(kr)\chi_q(\hat{\mathbf{r}}) \end{pmatrix}. \quad (6.35)$$

In both equations (6.34) and (6.35), the abbreviation

$$e_q = \frac{ick}{E + c^2} S_\kappa \quad (6.36)$$

is used.

Matching II: Jülich convention

Since the entries of the single-site scattering t-matrix become very small for large values of l or $|\kappa|$, respectively, it may be more convenient to use a formulation where the t-matrix itself and not the inverse is taken into account [43, 148]. The relativistic version was discussed by HUHNE *et al.* [30], where the regular scattering solution is given by

$$\mathbf{R}_q^{\text{outside}}(\mathbf{r}) = \sum_{q'} \left[\begin{pmatrix} j_{l'}(kr)\chi_{q'}(\hat{\mathbf{r}}) \\ e_{q'} j_{\bar{l}'}(kr)\chi_{q'}(\hat{\mathbf{r}}) \end{pmatrix} \delta_{q'q} - ik \begin{pmatrix} h_{l'}(kr)\chi_{q'}(\hat{\mathbf{r}}) \\ e_{q'} h_{\bar{l}'}(kr)\chi_{q'}(\hat{\mathbf{r}}) \end{pmatrix} t_{q'q} \right], \quad (6.37)$$

The associated irregular scattering solution is given by

$$\mathbf{H}_q^{\text{outside}}(\mathbf{r}) = \begin{pmatrix} h_l(kr)\chi_q(\hat{\mathbf{r}}) \\ e_q h_{\bar{l}}(kr)\chi_q(\hat{\mathbf{r}}) \end{pmatrix}. \quad (6.38)$$

Independent of the choice of the matching condition, the single-site t-matrix is an unknown quantity in general and has to be obtained numerically. Details on this will be explained in Section 6.5.3.

6.5. Numerical solution of the single-site scattering problem

Within this section, the numerical solution of the differential equations (6.9) and (6.10) for a non-spherical potential will be discussed. Within the non-relativistic full-potential KKR method, it was suggested by DRITTLER [7], to solve the underlying single-site scattering problem by means of the LIPPMANN-SCHWINGER equation, i.e. in terms of integral equations. In general, these integral equations can be solved iteratively via a BORN series. Under sufficient conditions, it was stated that this series converges after a few iterations (≈ 4) [7, p.44, pp. 93-99]. Convergence

properties of integral equations can be investigated by using the fix-point theorem of BANACH, [149, pp. 69-71] and [150, pp. 24-28]. In the original implementation of DRITTLER *et al.* [8] the integral equations were integral equations of the FREDHOLM type [146, pp. 904-905],

$$y(x) = y_0(x) + \lambda \int_a^b K(x, s)y(s)ds. \quad (6.39)$$

An iterative solution of such an integral equation, converges for

$$\max |K(x, s)| |\lambda| (b - a) < 1, \quad (6.40)$$

(see [151, pp.186-188] or [150, pp. 25-26]). Regarding the LIPPMANN-SCHWINGER equation this means that the BORN series converges for sufficiently small perturbations $\Delta V(\mathbf{r})$ and for a sufficiently small absolute value of the energy $|E|$. However, it is possible to reformulate the underlying equations in terms of integral equations of the VOLTERRA type [152, 153]. The iterative solution of integral equations of the VOLTERRA type,

$$y(x) = y_0(x) + \lambda \int_a^x K(x, s)y(s)ds, \quad (6.41)$$

already converge for a bounded kernel $\max |K(x, s)| < \infty$ [150, pp. 26-28], which is a much weaker condition compared to the iterative solution of the integral equations of the FREDHOLM type.

A similar approach like the one of DRITTLER [7] can also be applied for the relativistic single-site scattering problem, as could be shown by HUHNE *et al.* [30]. Within the method, it is necessary to introduce a certain cut-off radius close to the origin in order to avoid problems arising from the treatment of the irregular single-site scattering solutions. Recently, it was shown by ZELLER [154] that this approximation might become inconvenient for materials like NiTi and that the cut-off radius can be chosen arbitrarily small by using an analytical decoupling scheme and a subinterval procedure with CHEBYSHEV interpolations in each subinterval.

Alternatively to the solution via integral equations, it is possible to directly solve the differential equations (6.9) and (6.10), e.g. by using an ADAMS-BASHFORTH-MOULTON predictor corrector scheme [35, pp. 136-141]. The implementation of such a method will be explained in the following. In contrast to the illustrations of ZABLOUDIL *et al.* [34, p. 76], it will be demonstrated in Chapter 8 that both, the regular as well as the irregular scattering solutions, can be achieved with high accuracy.

6.5.1. Transformation of the differential equations

For the numerical solution of the single-site scattering solution it is convenient to transform the large and the small component of the DIRAC equation [34, p. 85] via

$$f_{q'q}(r) = \frac{Q_{q'q}(r)}{cr}, \quad \text{and} \quad g_{q'q}(r) = \frac{P_{q'q}(r)}{r}. \quad (6.42)$$

Introducing the energy $\varepsilon = W - c^2$ and rearranging the equations (6.9) and (6.10), the following system of differential equations can be obtained,

$$\text{I:} \quad \frac{d}{dr} Q_{q'q}(r) = \frac{\kappa'}{r} Q_{q'q}(r) - \varepsilon P_{q'q}(r) + \sum_{q''} \tilde{V}_{q'q''}^+(r) P_{q''q}(r), \quad (6.43)$$

$$\text{II:} \quad \frac{d}{dr} P_{q'q}(r) = -\frac{\kappa'}{r} P_{q'q}(r) + \left(\frac{\varepsilon}{c^2} + 1\right) Q_{q'q}(r) - \frac{1}{c^2} \sum_{q''} \tilde{V}_{q'q''}^-(r) Q_{q''q}(r). \quad (6.44)$$

To further simplify the formalism, it can be verified that equations (6.43) and (6.44) can be reformulated in terms of matrix equations. Therefore, the matrix \tilde{K} is introduced via

$$\tilde{K} = \begin{pmatrix} \kappa'_1 & 0 & 0 & 0 \\ 0 & \kappa'_2 & 0 & 0 \\ \vdots & \vdots & \ddots & \vdots \\ 0 & 0 & 0 & \kappa'_{q_{\max}} \end{pmatrix}. \quad (6.45)$$

Furthermore, by defining the matrices

$$\tilde{U}^+(r) = \tilde{V}^+(r) - \varepsilon \tilde{I}, \quad \text{and} \quad \tilde{U}^-(r) = \left(\frac{\varepsilon}{c^2} + 1\right) \tilde{I} - \frac{1}{c^2} \tilde{V}^-(r), \quad (6.46)$$

the following compact form of the radial differential equations can be derived,

$$\text{I:} \quad \frac{d}{dr} \tilde{Q}(r) = \frac{1}{r} \tilde{K} \cdot \tilde{Q}(r) + \tilde{U}^+(r) \cdot \tilde{P}(r), \quad (6.47)$$

$$\text{II:} \quad \frac{d}{dr} \tilde{P}(r) = -\frac{1}{r} \tilde{K} \cdot \tilde{P}(r) + \tilde{U}^-(r) \cdot \tilde{Q}(r). \quad (6.48)$$

Since the potential has a COULOMB like behaviour close to the origin, some components of the radial wave functions are heavily oscillating for $r \rightarrow 0$, especially for heavy ions. As an example, the large component of the regular scattering wave function of gold (Au) is illustrated in Figure 6.3. By transferring the radial mesh to a logarithmic mesh [34, pp. 85] within the muffin-tin sphere it is possible to decrease the step size near $r = 0$ to achieve a higher numerical accuracy. By choosing $r = e^x$, the differential equations (6.47) and (6.48) can be transformed to

$$\text{I:} \quad \frac{d}{dx} \tilde{Q}(x) = \tilde{K} \cdot \tilde{Q}(x) + e^x \tilde{U}^+(x) \cdot \tilde{P}(x), \quad (6.49)$$

$$\text{II:} \quad \frac{d}{dx} \tilde{P}(x) = -\tilde{K} \cdot \tilde{P}(x) + e^x \tilde{U}^-(x) \cdot \tilde{Q}(x). \quad (6.50)$$

In Section 6.3.1, the partition of the radial mesh into distinct regions, bounded by the critical radii, was introduced. Referring to Figure 6.2, another radius R_{MT} , called muffin-tin radius is illustrated. For the numerical solution, the logarithmic mesh is chosen within the interval $[R_0, R_{\text{MT}}]$, where $R_0 \approx 10^{-5}$ a.u. is the smallest value of r . Hence, the equations (6.49) and (6.50) have to be solved. For $r > R_{\text{MT}}$, several distinct intervals $[R_{\text{MT}}, R_{C_1}], \dots, [R_{C_i}, R_{C_{i+1}}], \dots, [R_{C_N}, R_{\text{BS}}]$ are introduced and (6.47) and (6.48) have to be solved within each interval. The procedure is constructed such that the initial values for the solution in the next interval are given by the solution at the last point of the previous interval.

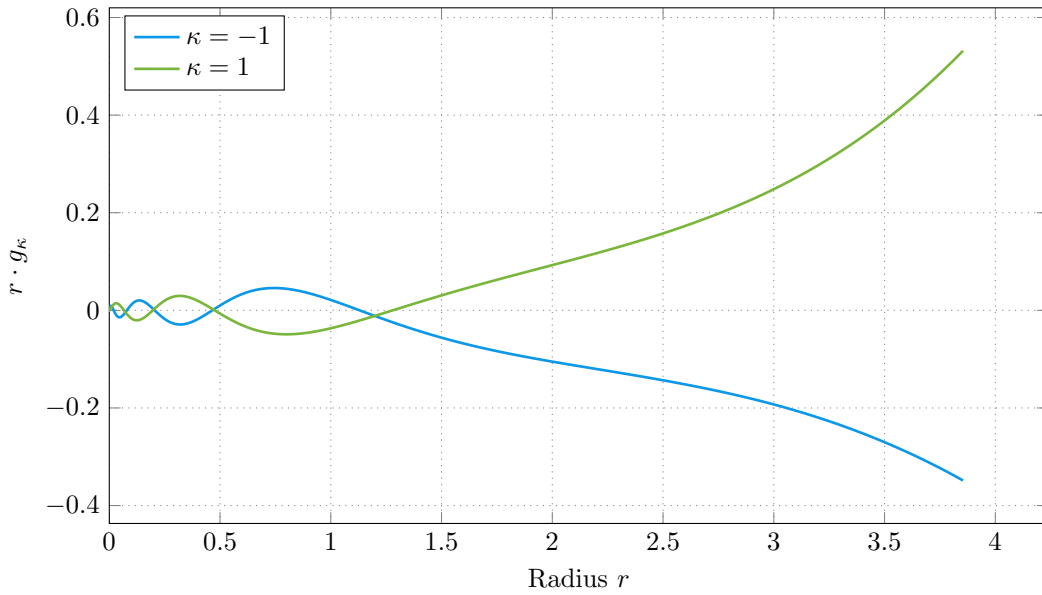


Figure 6.3.: Large component of the regular scattering solution for gold (Au) for the quantum numbers $\kappa = \pm 1$.

6.5.2. Initial conditions for the regular scattering solution

Previously it was shown, how the radial DIRAC equation for an arbitrary potential can be transformed into a set of ordinary differential equations of first order. To obtain reasonable initial values for the regular scattering solution, the approach of ZABLOUDIL *et al.* [34, pp. 85-86, p. 123] can be used, which will be explained within this section. Since the non-spherical terms in the potential are present due to the crystal field of the neighbouring atoms, the potential becomes more and more COULOMB-like close to the origin. Hence, for $|\mathbf{r}| \rightarrow 0$, a suitable physical approxi-

mation is given by

$$V(\mathbf{r}) \approx -\frac{2Z}{r}, \quad \text{and} \quad B(\mathbf{r}) \approx 0. \quad (6.51)$$

As explained in the previous section, a logarithmic mesh $r = e^x$ is chosen close to the origin. Using the approximation (6.51) for the differential equations (6.49) and (6.50) and taking the limit $x \rightarrow -\infty$ the following set of differential equations can be obtained,

$$\text{I:} \quad \frac{d}{dx} Q_{q'q}(x) = \kappa' Q_{q'q}(x) - 2Z P_{q'q}(x), \quad (6.52)$$

$$\text{II:} \quad \frac{d}{dx} P_{q'q}(x) = -\kappa' P_{q'q}(x) + \frac{2Z}{c^2} Q_{q'q}(x). \quad (6.53)$$

Forming the second derivative of $P_{q'q}(x)$ and replacing $\frac{d}{dx} Q_{q'q}(x)$ by means of (6.52), a decoupled second order differential equation can be found,

$$\frac{d^2}{dx^2} P_{q'q}(x) = \left(\kappa'^2 - \frac{4Z^2}{c^2} \right) P_{q'q}(x). \quad (6.54)$$

According to the theory of ordinary differential equations, (6.54) has two solutions, which are given by

$$P_{q'q}^1(x) = c_1 e^{\sqrt{\kappa'^2 - \frac{4Z^2}{c^2}} x} \quad \text{and} \quad P_{q'q}^2(x) = c_2 e^{-\sqrt{\kappa'^2 - \frac{4Z^2}{c^2}} x}. \quad (6.55)$$

Since $\sqrt{\kappa'^2 - \frac{4Z^2}{c^2}} > 0$, it follows that $P_{q'q}^1(x) \rightarrow 0$ for $x \rightarrow -\infty$ ($r \rightarrow 0$) and thus $P_{q'q}^1(x)$ can be identified as a solution, which is regular at the origin. Using equation (6.53), it is possible to derive an equation for the initial values of $Q_{q'q}^{\text{reg}}(x)$,

$$Q_{q'q}^{\text{reg}}(x_0) = \frac{\kappa' c^2}{2Z} \left(1 + \sqrt{1 - \frac{4Z^2}{\kappa'^2 c^2}} \right) P_{q'q}^{\text{reg}}(x_0). \quad (6.56)$$

Hence, it can be seen that $Q_{q'q}^{\text{reg}}(x_0)$ is calculated from $P_{q'q}^{\text{reg}}(x_0)$. Since the normalization of the scattering solution is done by matching the solution inside of the WIGNER-SEITZ cell to the free scattering solutions at the outside of the cell, $P_{q'q}^{\text{reg}}(x_0)$ can be chosen arbitrarily, e.g.

$$P_{q'q}^{\text{reg}}(x_0) = r_0 \sqrt{\kappa'^2 - \frac{4Z^2}{c^2}} \delta_{q'q}. \quad (6.57)$$

6.5.3. Normalization of regular scattering solutions and single-site t-matrix

After solving (6.43) and (6.44) numerically, the regular scattering solution has to be normalized properly. By construction, the numerical solution within the scattering potential has to be equal to the free solution at the outside of the scattering potential at $r = r_{BS}$,

$$\mathbf{R}_q^{\text{inside}}(R_{BS}) = \mathbf{R}_q^{\text{outside}}(R_{BS}). \quad (6.58)$$

According to section 6.4, two kinds of matching conditions are implemented, as will be explained in the following.

Normalization according to matching I

The numerical solution of the radial DIRAC equation (6.47) and (6.48) or (6.49) and (6.50) are given in terms of matrix valued functions $\tilde{P}(r)$ and $\tilde{Q}(r)$ with entries $P_{q'q}(r)$ and $Q_{q'q}(r)$, respectively. It is possible to construct normalized solutions $P_{q'q}^{\text{inside}}(r)$ and $Q_{q'q}^{\text{inside}}(r)$ by linear combinations of the numerical solutions via

$$P_{q'q}^{\text{inside}}(r) = \sum_{q''} P_{q'q''}(r) a_{q''q}, \quad \text{and} \quad Q_{q'q}^{\text{inside}}(r) = \sum_{q''} Q_{q'q''}(r) a_{q''q} \quad (6.59)$$

Using the above equations and the convention for the regular scattering solution according to matching I (6.34), it is possible to obtain the following algebraic system of linear equations at $r = R_{BS}$ for each pair of q and q' ,

$$\sum_{q''} \left[P_{q'q''}(R_{BS}) a_{q''q} - R_{BS} j_{l'}(kR_{BS}) \delta_{q'q''} t_{q''q}^{-1} \right] = -ikR_{BS} h_{l'}(kR_{BS}) \delta_{q'q}, \quad (6.60)$$

$$\sum_{q''} \left[Q_{q'q''}(R_{BS}) a_{q''q} - R_{BS} c e_{q'} j_{\bar{l}'}(kR_{BS}) \delta_{q'q''} t_{q''q}^{-1} \right] = -ikR_{BS} c e_{q'} h_{\bar{l}'}(kR_{BS}) \delta_{q'q}. \quad (6.61)$$

By introducing the matrices

$$\tilde{a} = \{a_{qq'}\}, \quad (6.62)$$

$$\tilde{J}(R_{BS}) = \{R_{BS} j_l(kR_{BS}) \delta_{qq'}\}, \quad (6.63)$$

$$\tilde{j}(R_{BS}) = \{R_{BS} c e_q j_{\bar{l}}(kR_{BS}) \delta_{qq'}\}, \quad (6.64)$$

$$\tilde{H}(R_{BS}) = \{R_{BS} h_l(kR_{BS}) \delta_{qq'}\}, \quad (6.65)$$

$$\tilde{h}(R_{BS}) = \{R_{BS} c e_q h_{\bar{l}}(kR_{BS}) \delta_{qq'}\}, \quad (6.66)$$

one can simplify the equations (6.60) and (6.61) by means of a matrix valued equation of the form

$$\begin{pmatrix} \tilde{P}(R_{BS}) & -\tilde{J}(R_{BS}) \\ \tilde{Q}(R_{BS}) & -\tilde{j}(R_{BS}) \end{pmatrix} \begin{pmatrix} \tilde{a} \\ \tilde{t}^{-1} \end{pmatrix} = \begin{pmatrix} -ik\tilde{H}(R_{BS}) \\ -ik\tilde{h}(R_{BS}) \end{pmatrix}. \quad (6.67)$$

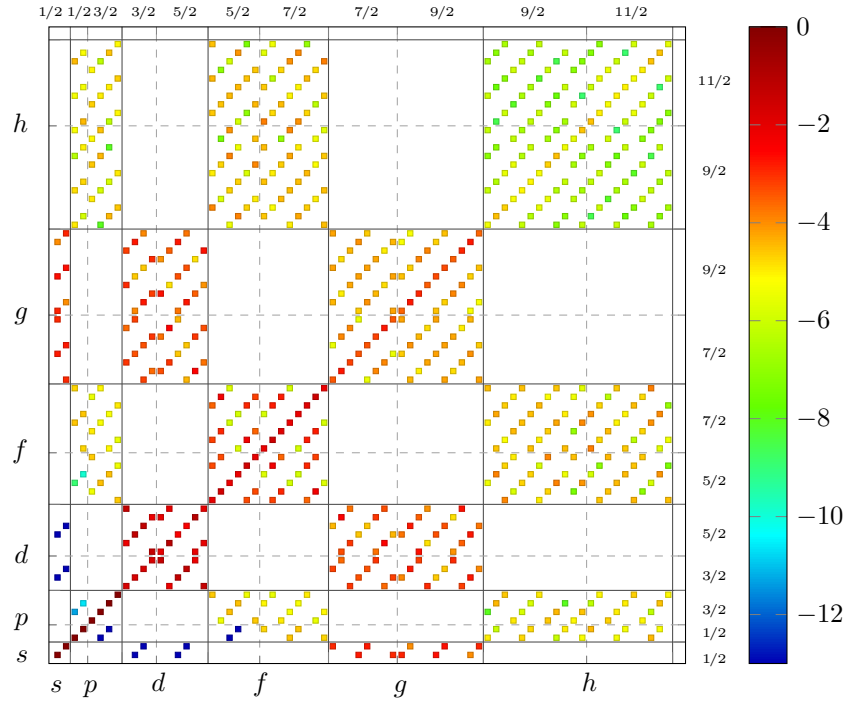


Figure 6.4.: Logarithm of the single-site scattering t-matrix for the cubic MATHIEU potential (details will be explained in Chapter 8). Used parameters are $U = 0.5$, $a = 2\pi$, $E = 1.5$ Ryd.

From the solution of (6.67), the inverse of the single-site scattering t-matrix \tilde{t} as well as the normalization coefficients $a_{q''q}$ of equation (6.59) can be calculated. As an example, the single-site scattering t-matrix for the cubic MATHIEU potential (see Chapter 8) is shown in Figure 6.4. Along the diagonal the absolute values of the entries are decreasing rapidly for increasing value of l . The same holds true for entries far away from the main diagonal. A similar behaviour can also be found for the regular single-site scattering solutions \tilde{P} and \tilde{Q} . Thus, solving (6.67) is numerically challenging. To obtain a numerical solution with high accuracy, the driver routine *zgesvxx* of the *Intel math kernel library* (MKL) was used. The method applies an equilibration of the coefficient matrix [155, pp. 64-71] as well as an iterative refinement of the solution [156, pp. 121-122].

Normalization according to matching II

Analogously to the derivation of the linear equation system (6.67) for matching I, a linear equation system for matching II can be derived by means of the Jülich

convention (6.37), which is given by

$$\begin{pmatrix} \tilde{P}(R_{BS}) & ik\tilde{H}(R_{BS}) \\ \tilde{Q}(R_{BS}) & ik\tilde{h}(R_{BS}) \end{pmatrix} \begin{pmatrix} \tilde{a} \\ \tilde{t} \end{pmatrix} = \begin{pmatrix} \tilde{J}(R_{BS}) \\ \tilde{j}(R_{BS}) \end{pmatrix}. \quad (6.68)$$

In contrast to matching I the single-site scattering t-matrix \tilde{t} can be obtained directly. Hence, the inversion of an ill-conditioned matrix can be omitted.

6.6. Initial conditions for the irregular scattering solution

Contrary to the regular scattering solution, where the numerical solution is achieved by starting at the origin, the irregular scattering solution is obtained by starting at the boundary sphere and integrating inwards. Therefore, in contrast to the regular scattering solution, which depends on the single-site scattering t-matrix, the irregular scattering solution outside of the WIGNER-SEITZ cell is independent of any unknown quantities. Thus, the initial values are given analytically.

For matching I, the irregular solution at the outside of the WIGNER-SEITZ cell is given by spherical BESSEL functions. According to equation (6.35) the initial conditions for the large and small component are

$$P_{q'q}^{\text{ir}, I}(R_{BS}) = \delta_{q'q} r j_l(k R_{BS}) \quad \text{and} \quad Q_{q'q}^{\text{ir}, I}(R_{BS}) = \delta_{q'q} \frac{r c^2 k}{E + c^2} j_{\bar{l}}(k R_{BS}). \quad (6.69)$$

The irregular scattering solution for matching II is given by spherical HANKEL functions at the outside of the WIGNER-SEITZ cell. Hence, the initial conditions can be formulated as follows,

$$P_{q'q}^{\text{ir}, II}(R_{BS}) = \delta_{q'q} r h_l(k R_{BS}) \quad \text{and} \quad Q_{q'q}^{\text{ir}, II}(R_{BS}) = \delta_{q'q} \frac{r c^2 k}{E + c^2} h_{\bar{l}}(k R_{BS}). \quad (6.70)$$

6.7. Implementation

In the previous sections, the basics for the numerical solution of the relativistic full-potential single-site scattering problem were presented. Since it is important for the tests, which will be explained in Chapter 7 and Chapter 8, an overview about different implemented solvers will be given during this section. The most important to mention is the one, which was finally implemented in *Hutsepot*. The solver is programmed using Fortran and is based on an ADAMS-BASHFORTH-MOULTON predictor corrector scheme with fixed and equidistant step size [157, pp. 74-77]. The order of the predictor step s_p and the corrector step s_c is fixed as well but it can be chosen to be $s_p = 1, \dots, 6$ and $s_c = s_p + 1, \dots, 12$, respectively. To assure that the obtained solution of the Fortran program is reasonable, a second program was developed, which

ode113	ADAMS-BASHFORTH-MOULTON predictor-corrector method, variable step size and variable order 1, . . . , 13, suitable for non-stiff differential equations [158, 159]
ode15s	implicit numerical differentiation formulas, variable step size and variable order 1, . . . , 5, suitable for stiff differential equations [158, 159]
ode45	DORMAND-PRINCE method, explicit RUNGE-KUTTA pair, variable step size and fixed order 5 [160, 158, 159]
ode23	BOGACKI-SHAMPINE method, explicit RUNGE-KUTTA pair, variable step size and fixed order 3 [161, 158, 159]
GBS	GRAGG-BULIRSCH-STOER extrapolation method [162, 163]
AB5	ADAMS-BASHFORTH-MOULTON predictor-corrector method, fixed step size, order 5 [34, pp. 60-61]
RK4	RUNGE-KUTTA method, fixed step size, order 4 [34, pp. 59-60]

Table 6.2.: Numerical methods for the solution of ordinary differential equations, used within the *Matlab* implementation of the fully relativistic single-site scattering problem.

was implemented in *Matlab*. The big advantage is that the numerical methods to solve ordinary differential equations can be switched easily, which allows an efficient comparison of different techniques. Especially to discuss if a differential equation is stiff or non-stiff, the performance of methods suitable for stiff and non-stiff equations can be compared. A list of all used numerical methods including a short description can be found in Table 6.2. To compare the solution of the differential equations (6.9) and (6.10) with the solution via integral equations, a third solver was implemented, which is based on the solution via the relativistic LIPPMANN-SCHWINGER equation [30],

$$\Phi_q(E, \mathbf{r}) = \mathring{\Phi}_q(E, \mathbf{r}) + \int_{\Omega_{WS}} d^3 r' \mathring{G}(E; \mathbf{r}, \mathbf{r}') \Delta V(\mathbf{r}') \Phi_q(E, \mathbf{r}'). \quad (6.71)$$

Here, $\Phi_q(E, \mathbf{r})$ denotes either the regular or the irregular single-site scattering solution. $\mathring{\Phi}_q(E, \mathbf{r})$ is the solution of the reference system and $\mathring{G}(E; \mathbf{r}, \mathbf{r}')$ the single-site GREEN function of the reference system.

6.8. Left-hand side solution

In the next section, the fully relativistic multiple scattering GREEN function will be introduced. It will be shown that besides the ordinary solution or right-hand side solution of the DIRAC equation a so called left-hand side solution of the DIRAC

equation is needed. This issue was initially described by TAMURA [133]. Formally, the left-hand side solution of the DIRAC equation can be defined via

$$\langle \phi_Q^L | (W - \tilde{H}) = 0. \quad (6.72)$$

Hence, by taking the adjoint of (6.72) the adjoint of the left hand side solution can be calculated in real space representation by solving the following DIRAC equation,

$$(W^* - \tilde{H}^\dagger) \phi_q^L(\mathbf{r}) = 0. \quad (6.73)$$

Since the matrices $\tilde{\sigma}_i$ and $\tilde{\alpha}_i$ are self-adjoint, the operator \tilde{H}^\dagger is given by

$$\tilde{H}^\dagger = ic \tilde{\boldsymbol{\alpha}} \cdot \nabla + \frac{1}{2} \tilde{\beta} c^2 + V_{\text{eff}}(\mathbf{r})^* + \tilde{\beta} \tilde{\boldsymbol{\sigma}} \cdot \mathbf{B}^*. \quad (6.74)$$

Following the derivation of TAMURA [133], the time-reversal operator \tilde{T} can be introduced by

$$\tilde{T} = -i \begin{pmatrix} \tilde{\sigma}_y & 0 \\ 0 & \tilde{\sigma}_y \end{pmatrix} \tilde{T}_0, \quad (6.75)$$

where \tilde{T}_0 is the complex-conjugation operator. The time reversal operator satisfies the property $\tilde{T}^2 = -\hat{1}$. Therefore, the inverse is given by $\tilde{T}^{-1} = -\tilde{T}$. Furthermore, it can be shown that the transformation of the Hamiltonian by means of the time reversal operator fulfils the relation $\tilde{T} \tilde{H}(-\mathbf{B}) \tilde{T}^{-1} = \tilde{H}^\dagger(\mathbf{B})$. From this behaviour, the eigenfunctions of \tilde{H}^\dagger can be estimated via

$$\begin{aligned} 0 &= (W - \tilde{H}^\dagger) \phi_q^L(\mathbf{r}) \\ &= \tilde{T} \left(W - \tilde{H}(V_{\text{eff}}, -\mathbf{B}) \right) \tilde{T}^{-1} \phi_q^L(\mathbf{r}) \\ &= \tilde{T} \left(W - \tilde{H}(V_{\text{eff}}, -\mathbf{B}) \right) \phi_q^{\tilde{\text{R}}}(\mathbf{r}). \end{aligned} \quad (6.76)$$

Hence, $\phi_q^{\tilde{\text{R}}}(\mathbf{r}) = \tilde{T}^{-1} \phi_q^L(\mathbf{r})$ are eigenfunctions of $(W - \tilde{H}(-\mathbf{B}))$. It follows that the left-hand-side solution can be calculated from the right-hand-side solution of $\tilde{H}(-\mathbf{B})$ by

$$\langle \phi_Q^L | \mathbf{r} \rangle = \left[\tilde{T} \phi_q^{\tilde{\text{R}}}(\mathbf{r}) \right]^\dagger. \quad (6.77)$$

Since $\phi_q^{\tilde{\text{R}}}(\mathbf{r})$ is a right-hand side solution of the DIRAC equation with inverted magnetic field, the formalism which was introduced in the previous sections can be applied without restrictions. According to equation (6.4), $\phi_q^{\tilde{\text{R}}}(\mathbf{r})$ can be written as an expansion into spin-angular functions. To understand how the time reversal operator acts on $\phi_q^{\tilde{\text{R}}}(\mathbf{r})$, the application of $\tilde{\sigma}_y$ to $\chi_{\kappa, \mu}(\hat{\mathbf{r}})$ needs to be investigated. By

using complex spherical harmonics and the CONDON-SHORTLEY phase [164, p. 52] $Y_l^{-m} = (-1)^m (Y_l^m)^*$ and by verifying the relation $C_{\kappa,\mu}^{m_s} = -S_\kappa C_{\kappa,-\mu}^{-m_s}$ from table 6.1, the following equation can be obtained,

$$\tilde{\sigma}_y \chi_{\kappa,\mu}(\hat{\mathbf{r}}) = i S_\kappa (-1)^{\mu+1/2} \chi_{\kappa,-\mu}(\hat{\mathbf{r}})^*. \quad (6.78)$$

Thus, the adjoint left-hand-side solution is given by

$$\phi_Q^L(\mathbf{r}) = \sum_{\kappa',\mu'} S_{\kappa'} (-1)^{\mu'+1/2} \begin{pmatrix} g_{\kappa',\mu';\kappa,\mu}^{\tilde{\mathbf{R}}}(r)^* \chi_{\kappa',-\mu'}(\hat{\mathbf{r}}) \\ -i f_{\kappa',\mu';\kappa,\mu}^{\tilde{\mathbf{R}}}(r)^* \chi_{-\kappa',-\mu'}(\hat{\mathbf{r}}) \end{pmatrix}. \quad (6.79)$$

Finally, to obtain an expression for the left hand side solution, the adjoint of equation (6.79) has to be derived,

$$\langle \phi_Q^L | \mathbf{r} \rangle = \sum_{\kappa',\mu'} S_{\kappa'} (-1)^{\mu'+1/2} \begin{pmatrix} g_{\kappa',\mu';\kappa,\mu}^{\tilde{\mathbf{R}}}(r) \chi_{\kappa',-\mu'}(\hat{\mathbf{r}})^\dagger \\ i f_{\kappa',\mu';\kappa,\mu}^{\tilde{\mathbf{R}}}(r) \chi_{-\kappa',-\mu'}(\hat{\mathbf{r}})^\dagger \end{pmatrix}. \quad (6.80)$$

In general it is always possible to obtain the left-hand side solution from the right-hand side solution of the DIRAC equation if no magnetic field is present. For an arbitrary magnetic field, one needs to solve the single-site scattering problem twice, for $\hat{H}(\mathbf{B})$ and $\hat{H}(-\mathbf{B})$, respectively.

6.9. Multiple scattering Green Function

In Section 2.1 the non-relativistic KKR method was introduced and the multiple scattering GREEN function was given in equation (2.8). A similar form can be found for the multiple scattering GREEN function in the fully relativistic KKR method, [130, pp. 437-440, pp. 443-450] or [165, 30]. According to matching II, where the regular single-site scattering solutions at the site \mathbf{R}_m are denoted by $\mathbf{R}_q^m(W, \mathbf{r}_m)$ and the irregular single-site scattering solutions are denoted by $\mathbf{H}_q^m(W, \mathbf{r}_m)$, respectively, the multiple scattering GREEN function can be written as

$$\begin{aligned} \tilde{G}(W; \mathbf{r}_n + \mathbf{R}_n, \mathbf{r}_m + \mathbf{R}_m) &= \sum_{q,q'} \mathbf{R}_q^n(W, \mathbf{r}_n) \tilde{G}_{qq'}^{mm}(W) \mathbf{R}_{q'}^m(W, \mathbf{r}_m)^\times \\ &\quad - \delta_{nm} \sum_q (\mathbf{H}_q^n(W, \mathbf{r}_n) \mathbf{R}_q^m(W, \mathbf{r}_m)^\times \theta(r_n - r_m) \\ &\quad \quad \quad + \mathbf{R}_q^n(W, \mathbf{r}_n) \mathbf{H}_q^m(W, \mathbf{r}_m)^\times \theta(r_m - r_n)). \end{aligned} \quad (6.81)$$

In the above equation $\mathbf{R}_q^m(W, \mathbf{r}_m)^\times$ denotes the left-hand side solution, which is a 1×4 row matrix, whereas $\mathbf{R}_q^m(W, \mathbf{r}_m)$ is a 4×1 column matrix. The product of two such matrices, i.e. $\mathbf{H}_q^n(W, \mathbf{r}_n) \mathbf{R}_q^m(W, \mathbf{r}_m)^\times$ is a 4×4 matrix and hence in contrast

to the non-relativistic case, where the GREEN function is a scalar valued function, the GREEN function is a 4×4 matrix in the relativistic case. In the first part of the above equation, regular single-site scattering solutions at two different sites \mathbf{R}_m and \mathbf{R}_n are combined, which represents the multiple scattering contribution within the multiple-scattering GREEN function. Products of the regular and the irregular single-site scattering solution at the same site, like in the second term of equation (6.81), represent the single-site scattering contribution.

By introducing the scattering path operator [130, pp. 437-440],

$$\tilde{\tau}^{ij}(W) = \delta_{ij}\tilde{t}^i(W) + \sum_{k \neq i} \tilde{t}^i(W)\tilde{G}_0(W)\tilde{\tau}^{kj}(W), \quad (6.82)$$

it is possible to express the multiple scattering GREEN function in terms of the scattering solutions $\mathbf{Z}_q^m(W, \mathbf{r}_m)$ and $\mathbf{J}_q^m(W, \mathbf{r}_m)$ according to matching I,

$$\begin{aligned} \tilde{G}(W; \mathbf{r}_n + \mathbf{R}_n, \mathbf{r}_m + \mathbf{R}_m) &= \sum_{q, q'} \mathbf{Z}_q^n(W, \mathbf{r}_n)\tilde{\tau}_{qq'}^{nm}(W)\mathbf{Z}_{q'}^m(W, \mathbf{r}_m)^\times - \\ &- \delta_{nm} \sum_q (\mathbf{J}_q^n(W, \mathbf{r}_n)\mathbf{Z}_q^m(W, \mathbf{r}_m)^\times \theta(r_n - r_m) \\ &+ \mathbf{Z}_q^n(W, \mathbf{r}_n)\mathbf{J}_q^m(W, \mathbf{r}_m)^\times \theta(r_m - r_n)). \end{aligned} \quad (6.83)$$

6.10. The Lloyd equation

LLOYD's equation [166, 167] provides a powerful tool for the calculation of the integrated density of states. It allows an accurate estimation of the FERMI energy, which is needed for the calculation of the charge density. In the non-relativistic real space representation, the GREEN function $G(E, \mathbf{r}, \mathbf{r}')$ is a scalar function of the coordinates \mathbf{r} and \mathbf{r}' . Hence, it commutes with the potential $V(\mathbf{r})$ and the general form of the LLOYD equation can be found in a few steps using elementary mathematics [168, 152]. Regarding the relativistic case, the GREEN function and the potential are matrix valued functions which do not commute in general. Nevertheless, fully relativistic implementations of the LLOYD equation exist [169, 170]. The goal of this chapter is to give a general but concise derivation of the LLOYD equation for non-commuting operators.

Suppose the solution of a reference system is known and the associated GREEN function is denoted by $\hat{G}_0(E)$. Since the density of states is defined as $n(E) = -\frac{1}{\pi}\Im \text{Tr} \hat{G}(E)$, the difference of the density of states of the reference system and the perturbed system can be calculated via

$$\Delta n(E) = -\frac{1}{\pi}\Im \text{Tr} [\hat{G}(E) - \hat{G}_0(E)] = -\frac{1}{\pi}\Im \text{Tr} [\hat{G}_0(E)\hat{V}\hat{G}(E)]. \quad (6.84)$$

The second identity in the above equation can be verified using the DYSON equation $\hat{G} = \hat{G}_0 + \hat{G}_0 \hat{V} \hat{G}$. Furthermore, from the DYSON equation it follows that $\hat{G} = (1 - \hat{G}_0 \hat{V})^{-1} \hat{G}_0$. Using the property that the trace of the product of several operators is invariant under cyclic permutation ($\text{Tr } \hat{A} \hat{B} \hat{C} = \text{Tr } \hat{C} \hat{A} \hat{B} = \text{Tr } \hat{B} \hat{C} \hat{A}$), one derives

$$\Delta n(E) = -\frac{1}{\pi} \Im \text{Tr} \left[\hat{G}_0(E) \hat{G}_0(E) \hat{V} (1 - \hat{G}_0(E) \hat{V})^{-1} \right]. \quad (6.85)$$

Assuming that the condition $\|\hat{G}_0 \hat{V}\| < 1$ is fulfilled, VON-NEUMANN's theorem [149, pp. 59-60] can be applied, which gives a series expansion for the inverse operator in terms of $(1 - \hat{G}_0(E) \hat{V})^{-1} = \sum_{n=0}^{\infty} (\hat{G}_0 \hat{V})^n$. In other words, VON-NEUMANN's theorem represents the analogue of the geometric series for linear operators. Using the VON-NEUMANN series together with the identity $\frac{d}{dE} \hat{G}_0(E) = -\hat{G}_0(E) \hat{G}_0(E)$, the difference of the density of states can be written as follows,

$$\Delta n(E) = -\frac{1}{\pi} \Im \text{Tr} \left[- \left(\frac{d}{dE} \hat{G}_0(E) \hat{V} \right) \sum_{n=0}^{\infty} (\hat{G}_0(E) \hat{V})^n \right]. \quad (6.86)$$

For the next step, one needs the derivative of $\hat{G}_0 \hat{V}$. Due to the trace operation it is not necessary to discuss if $\frac{d}{dE} \hat{G}_0(E) \hat{V}$ and $\hat{G}_0 \hat{V}$ commute, since cyclic permutation is allowed anyway. Hence, the trace of the derivative is given by

$$\text{Tr} \left[\frac{d}{dE} (\hat{G}_0(E) \hat{V})^n \right] = \text{Tr} \left[n \left(\frac{d}{dE} \hat{G}_0(E) \hat{V} \right) (\hat{G}_0(E) \hat{V})^{n-1} \right]. \quad (6.87)$$

Putting together equation (6.86) and (6.87), one ends up with the equation

$$\Delta n(E) = -\frac{1}{\pi} \Im \text{Tr} \left[\frac{d}{dE} \sum_{n=1}^{\infty} \frac{(\hat{G}_0(E) \hat{V})^n}{n} \right] = -\frac{1}{\pi} \Im \text{Tr} \left[\frac{d}{dE} \ln (\hat{1} - \hat{G}_0(E) \hat{V}) \right]. \quad (6.88)$$

In the second part, the definition of the logarithm for linear operators $\ln(1 - \hat{x}) = -\hat{x} - \frac{\hat{x}^2}{2} - \dots$ is used. By applying the definition of the integrated density of states $\Delta N(E) = \int_{-\infty}^E d\epsilon \Delta n(\epsilon)$, one finally obtains the LLOYD's equation

$$\Delta N(E) = -\frac{1}{\pi} \Im \text{Tr} \left[\ln (\hat{1} - \hat{G}_0(E) \hat{V}) \right]. \quad (6.89)$$

Part III.

Tests of the relativistic extension

7. The relativistic Coulomb problem

7.1. Introduction

The solution of the DIRAC equation for a COULOMB potential is a standard example in many books about relativistic quantum mechanics [130, 171, 172]. A comprehensive mathematical discussion of the COULOMB-DIRAC problem was published by SWAINSON and DRAKE [36, 173, 174]. Unfortunately, all works mentioned here concentrate on eigenstates of the COULOMB-DIRAC Hamiltonian, i.e. on the regular solutions. A motivation for studying the COULOMB potential within this thesis can be verified from Figure 7.1, where the relativistic and the non-relativistic irregular single-site scattering wave function for a screened COULOMB potential for copper, obtained from a self-consistent calculation for $\kappa = -1$ or $l = 0$ is shown. Since relativistic effects are small for copper, both wave-functions appear to be similar far away from the origin. However, for small values of r the relativistic solution shows a sudden deviation from the non-relativistic behaviour. Since the screened COULOMB

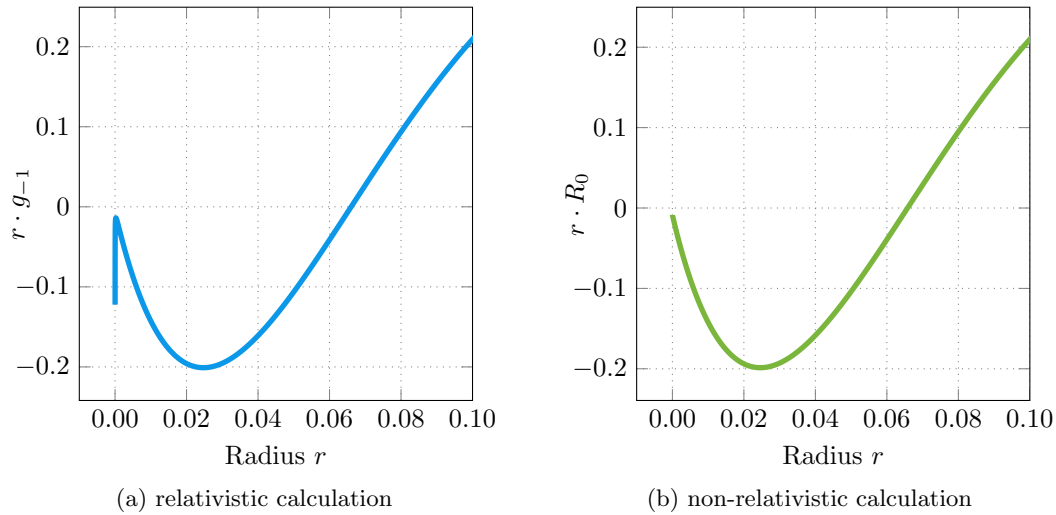


Figure 7.1.: Comparison of a relativistic and a non-relativistic irregular single-site scattering solution ($l = 0$, $\kappa = -1$) for a screened COULOMB potential of copper.

potential is approximately similar to a pure COULOMB potential for very small values of r , and the pure COULOMB potential problem can be solved analytically, the unexpected asymptotic behaviour of the irregular scattering solution close to the origin can be explained. Furthermore, using *Matlab*, different numerical methods for the solution of the DIRAC equation for the COULOMB potential will be discussed and the choice of an exponential mesh within the muffin-tin sphere will be motivated.

7.2. Asymptotic behaviour

The asymptotic behaviour of the regular and, especially, the irregular single-site scattering wave functions for $r \ll 1$ can be analysed from the underlying differential equations, which will be derived in the following. Since the COULOMB potential $\sim 1/r$ is a spherical potential, the expansion into spherical harmonics contains the spherical component only,

$$V_{lm}(r) = -\frac{1}{\sqrt{\pi}} \frac{Z}{r} \delta_{l,0} \delta_{m,0}. \quad (7.1)$$

For spherical potentials, the approach of equation (6.4) decouples with respect to κ and μ . Furthermore, if no magnetic field is present, the large and the small component of the relativistic solution of the DIRAC equation (6.2) are independent of the magnetic quantum number μ and can be written as follows,

$$\phi_{\kappa,\mu}(\mathbf{r}) = \begin{pmatrix} g_{\kappa}(r) \chi_{\kappa,\mu}(\hat{\mathbf{r}}) \\ i f_{\kappa}(r) \chi_{-\kappa,\mu}(\hat{\mathbf{r}}) \end{pmatrix}. \quad (7.2)$$

The associated differential equations for f_{κ} and g_{κ} are given by

$$\left[\frac{c^2}{2} - \frac{2Z}{r} - W \right] g_{\kappa}(r) + \left[\frac{\kappa c}{r} - \frac{c}{r} \frac{d}{dr} r \right] f_{\kappa}(r) = 0, \quad (7.3)$$

$$\left[\frac{\kappa c}{r} + \frac{c}{r} \frac{d}{dr} r \right] g_{\kappa}(r) - \left[\frac{c^2}{2} + \frac{2Z}{r} + W \right] f_{\kappa}(r) = 0. \quad (7.4)$$

It remains to solve a linear system of two coupled differential equations, which can be decoupled corresponding to [36] by a transformation of the wave function according to

$$\begin{pmatrix} \tilde{g}_{\kappa}(r) \\ \tilde{f}_{\kappa}(r) \end{pmatrix} = \begin{pmatrix} 1 & X \\ X & 1 \end{pmatrix} \cdot \begin{pmatrix} g_{\kappa}(r) \\ f_{\kappa}(r) \end{pmatrix}. \quad (7.5)$$

The newly introduced quantities are given by

$$X = \frac{2(\gamma - \kappa)}{cZ}, \quad (7.6)$$

$$\gamma = \sqrt{\kappa^2 - \frac{4Z^2}{c^2}}, \quad (7.7)$$

$$\epsilon = \frac{W}{c}, \quad (7.8)$$

$$\omega^2 = \left(\frac{c}{2} - \frac{W}{c}\right)^2. \quad (7.9)$$

By using (7.5) together with (7.3) and (7.4), two differential equations of second order can be found,

$$\left[\frac{d^2}{dr^2} + \frac{2}{r} \frac{d}{dr} - \frac{\gamma(\gamma+1)}{r^2} + \frac{2\alpha Z\epsilon}{r} - \omega^2 \right] \tilde{g}_\kappa(r) = 0, \quad (7.10)$$

$$\left[\frac{d^2}{dr^2} + \frac{2}{r} \frac{d}{dr} - \frac{\gamma(\gamma-1)}{r^2} + \frac{2\alpha Z\epsilon}{r} - \omega^2 \right] \tilde{f}_\kappa(r) = 0. \quad (7.11)$$

The differential equations presented above are of the same form as the radial SCHRÖDINGER equation [175, pp. 168]. Approaching the origin $r \rightarrow 0$, the angular momentum barriers $\gamma(\gamma+1)/r^2$ and $\gamma(\gamma-1)/r^2$ in (7.10) and (7.11), respectively, are the dominant terms and the contribution of $2\alpha Z\epsilon/r$ and ω^2 can be neglected. Introducing the quantities $\tilde{P}_\kappa = r \tilde{g}_\kappa$ and $\tilde{Q}_\kappa = r \tilde{f}_\kappa$, the first derivative cancels and the following differential equations can be obtained,

$$\left[\frac{d^2}{dr^2} - \frac{\gamma(\gamma+1)}{r^2} \right] \tilde{P}_\kappa(r) = 0, \quad (7.12)$$

$$\left[\frac{d^2}{dr^2} - \frac{\gamma(\gamma-1)}{r^2} \right] \tilde{Q}_\kappa(r) = 0. \quad (7.13)$$

The solution of both equations can be calculated by assuming rational functions $\tilde{P}_\kappa(r) \sim r^{\alpha_1}$ and $\tilde{Q}_\kappa(r) \sim r^{\alpha_2}$. Forming the derivative

$$\frac{d^2}{dr^2} r^\alpha = \alpha(\alpha-1)r^{\alpha-2}, \quad (7.14)$$

the following two algebraic equations for the coefficients α_1 and α_2 can be found from (7.12) and (7.13),

$$\alpha_1(\alpha_1 - 1) = \gamma(\gamma + 1) \quad \text{and} \quad \alpha_2(\alpha_2 - 1) = \gamma(\gamma - 1). \quad (7.15)$$

After solving equation (7.15), it is possible to verify the asymptotic behaviour of the transformed functions \tilde{P}_κ and \tilde{Q}_κ close to the origin, which is given by

$$\tilde{P}_\kappa = c_1 r^{\gamma+1} + c_2 r^{-\gamma}, \quad (7.16)$$

$$\tilde{Q}_\kappa = c_3 r^\gamma + c_4 r^{-\gamma+1}. \quad (7.17)$$

Since both solutions, the large component g_κ and the small component f_κ of equation (7.3) and (7.4) are given as a linear combination of \tilde{P}_κ/r and \tilde{Q}_κ/r , the leading term of the irregular single-site scattering solution, which is singular at the origin, is given by $r^{-\gamma-1}$ in both cases. To confirm the solution behaviour for $r \ll 1$, a double logarithmic plot of the numerical solution for $Z = 79$, $c = \frac{2}{\alpha}$, and various values for κ is illustrated in Figure 7.2. The predicted asymptotic behaviour is clearly revealed.

Referring to Figure 7.1 and regarding the special case of an s state ($l = 0$ and $\kappa = -1$) for a small atomic number $4Z^2/c^2 \approx 0$, the relativistic irregular solution has an asymptotic behaviour $\sim r^{-2}$ which is in contrast to the non-relativistic solution $\sim r^{-1}$. A double-logarithmic plot of the solution, illustrated in Figure 7.1a can be found in Figure 7.3a. For the s wave function of copper ($Z = 29$, $\kappa = -1$) the analytical value of $\gamma = \sqrt{\kappa^2 - \frac{4Z^2}{c^2}}$ is given by $\gamma \approx 0.977$. To verify, if a similar value can be observed for the numerical solution of the screened COULOMB potential, the slope of the linear graph in Figure 7.3a can be calculated and a numerical value of $\gamma = 0.951$ can be achieved for the minimal radius, which is given by $r = 10^{-5}$ for the present example. To improve the numerical value by extrapolating to $r \rightarrow 0$, the derivative of the solution can be taken into account (see Figure 7.3b). For the derivative, an exponential behaviour can be observed, which can be fitted by using

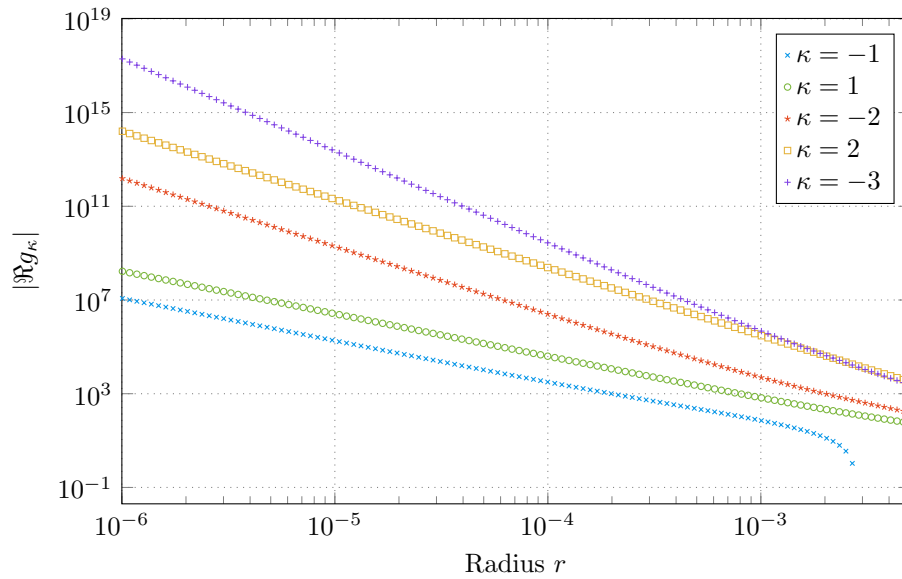
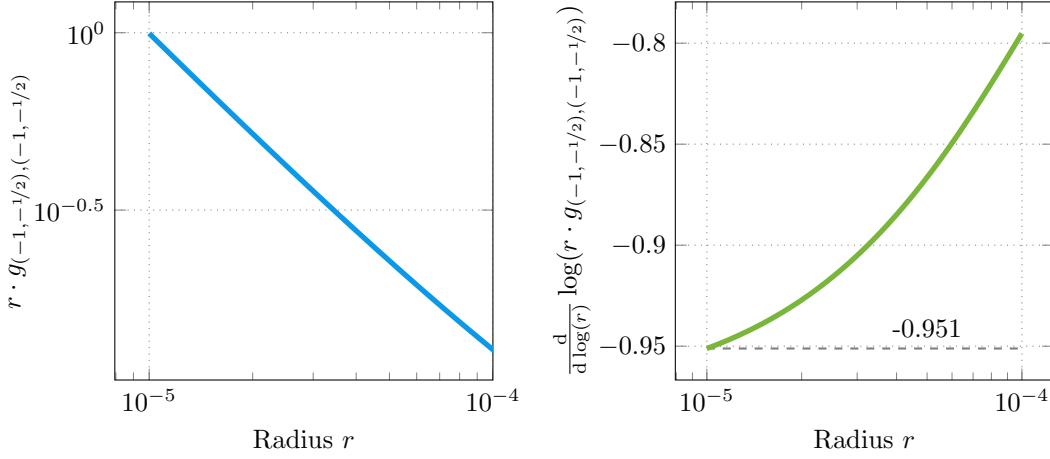


Figure 7.2.: Double-logarithmic plot of the real part of a relativistic irregular single-site scattering solutions for a COULOMB potential ($Z = 79$) close to the origin.

a function of the form

$$\gamma(r) = be^{\frac{\log(r)}{c}}. \quad (7.18)$$

By calculating the limit $r \rightarrow 0$ a better approximation $\gamma \approx 0.98$ can be found, which is in very good agreement with the analytical value of $\gamma \approx 0.977$. Hence, from the considerations of this section, the sudden change of the irregular single-site scattering wave function for $r \ll 1$ can be explained.



(a) Double-logarithmic plot close to the origin. (b) Derivative of the double logarithmic plot close to the origin.

Figure 7.3.: Asymptotic behaviour of the relativistic irregular scattering solution ($l = 0$, $\kappa = -1$) for a screened COULOMB potential of Cu.

7.3. Exact solution

As already mentioned in the previous section, the first derivative in (7.10) and (7.11) cancels by introducing the quantities $\tilde{P}_\kappa = r \tilde{g}_\kappa$ and $\tilde{Q}_\kappa = r \tilde{f}_\kappa$ and the following differential equations remain,

$$\left[\frac{d^2}{dr^2} - \frac{\gamma(\gamma + 1)}{r^2} + \frac{2\alpha Z\epsilon}{r} - \omega^2 \right] \tilde{P}_\kappa(r) = 0, \quad (7.19)$$

$$\left[\frac{d^2}{dr^2} - \frac{\gamma(\gamma - 1)}{r^2} + \frac{2\alpha Z\epsilon}{r} - \omega^2 \right] \tilde{Q}_\kappa(r) = 0. \quad (7.20)$$

Both equations can be solved in terms of the WHITTAKER functions $M_{k,m}(r)$ and $W_{k,m}(r)$ [176, 177], where the solution is given by

$$\tilde{P}_\kappa(r) = c_1 M_{Z\alpha\epsilon/\omega, g+1/2}(2r\omega) + c_2 W_{Z\alpha\epsilon/\omega, g+1/2}(2r\omega), \quad (7.21)$$

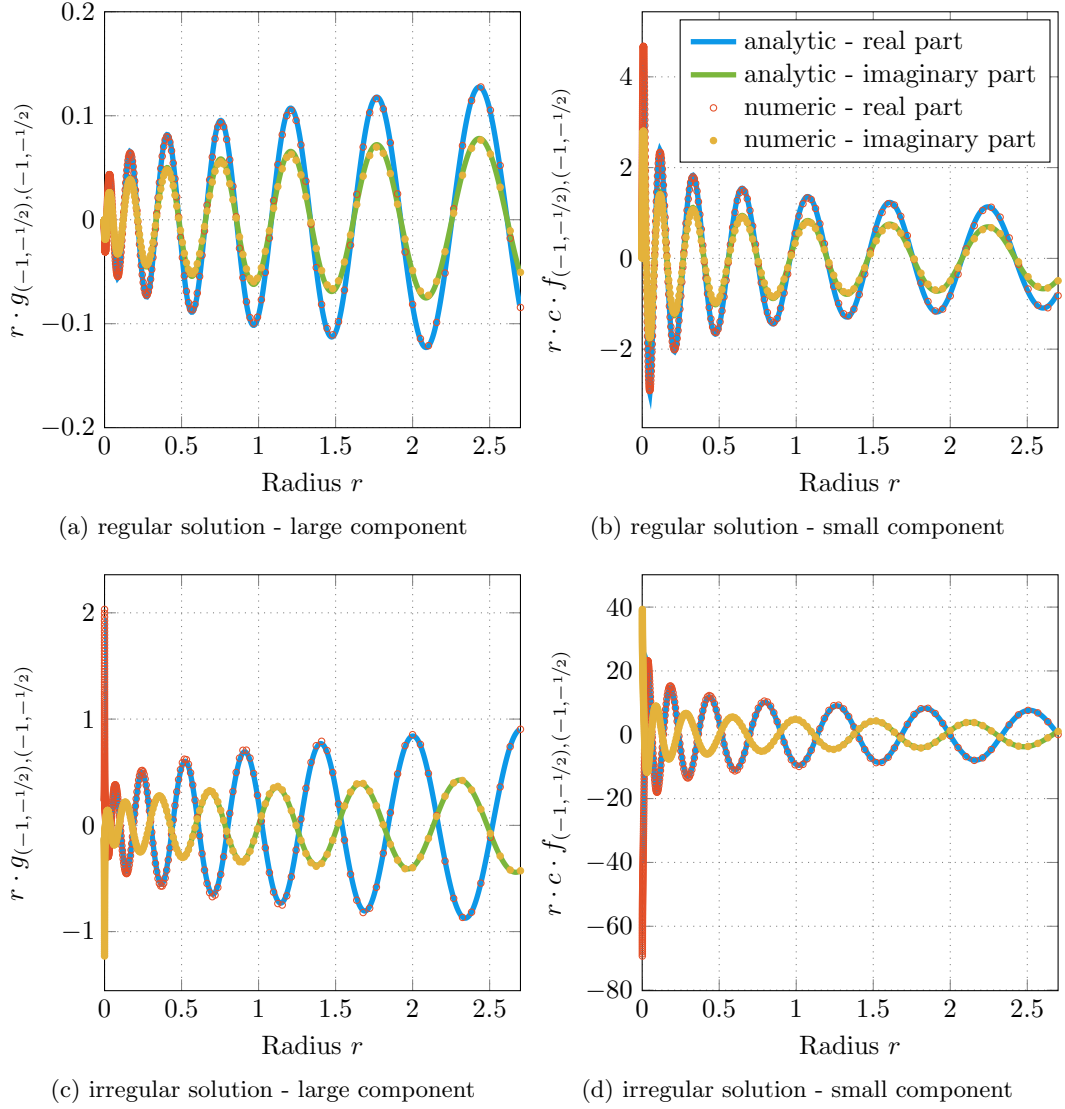


Figure 7.4.: Comparison of the analytical and the numerical solution for a uranium COULOMB potential.

and

$$\tilde{Q}_\kappa(r) = c_1 M_{Z\alpha\epsilon/\omega, g-1/2}(2r\omega) + c_2 W_{Z\alpha\epsilon/\omega, g-1/2}(2r\omega). \quad (7.22)$$

The analytical solution can be used to test the numerical implementation of the solver for the single-site scattering problem. Using the transformation matrix of (7.5), the initial conditions of the regular solution (6.57) and (6.56) as well as the

initial conditions of the irregular solution (6.69) or (6.70) can be used to determine the initial conditions of (7.21) and (7.22) for the functions $\tilde{P}(r)$ and $\tilde{Q}(r)$. Out of it, the unknown coefficients in (7.21) and (7.22) can be calculated. As an example, the scattering solutions for $\kappa = -1$ ($l = 0$) for an uranium COULOMB potential ($Z = 92$) are considered. Even though uranium is radioactive, it is the heaviest atom within the periodic table, which is still occurring naturally in low concentrations on the planet earth. Due to the large atomic number, relativistic effects are significant. To obtain scattering solutions an energy of 1 Ry is used. The numerical solution was obtained using an ADAMS-BASHFORTH-MOULTON predictor-corrector method of order 5 and 1001 mesh points. According to Figure 7.4, the numerical solution reflects the general behaviour of the analytical solution. To confirm the investigations of the previous section, the asymptotic behaviour of the analytic irregular scattering solution can be discussed. The double logarithmic plot of the large and small component is illustrated in Figure 7.5. Again, a linear behaviour can be seen and the slope can be calculated via the derivation of the double logarithmic plot. For $r \rightarrow 0$ a value of -0.741 can be found for both, the large and the small component. This value matches exactly to the value of $-\gamma = -\sqrt{\kappa^2 - \frac{4Z^2}{c^2}}$ using $\kappa = -1$, $Z = 92$ and $c = 274$. The result is in perfect agreement with (7.16) and (7.17).

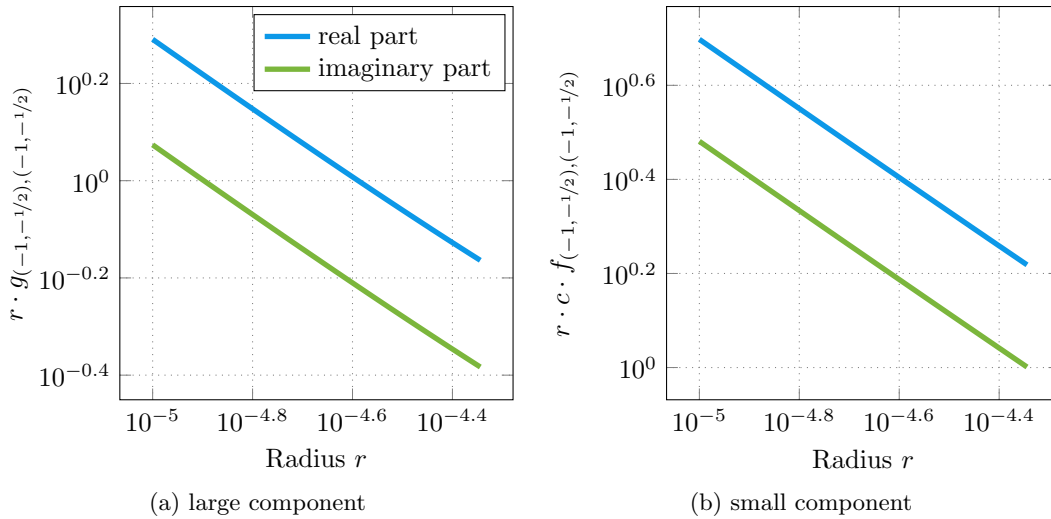


Figure 7.5.: Asymptotic behaviour of the analytic relativistic irregular single-site scattering solution ($l = 0$, $\kappa = -1$) for a uranium COULOMB potential ($Z=92$).

7.4. Numerical accuracy

Besides the asymptotic behaviour of the relativistic single-site scattering solution of the COULOMB-DIRAC problem, the accuracy for the numerical solution was investigated. The results in the first part of this section were obtained using *Matlab* and different methods for the solution of the differential equation [Ge2], whereas in the second part the results are achieved using the Fortran implementation within *Hutsepot*.

For the test using *Matlab*, a COULOMB potential with an atomic number of $Z = 79$ was used since it represents the element gold (Au). Due to the large atomic mass and non-negligible spin-orbit coupling, which causes the typical golden colour, it is a prominent example for relativistic effects. Usually, for KKR calculations, a maximal angular momentum quantum number $l_{\max} = 3$ or $l_{\max} = 4$ is used in practice. For the test which is discussed in the following, this value was slightly increased up to $l_{\max} = 5$, to ensure that the discussion is still valid for a higher value. To obtain a scattering solution, the energy was chosen to be $\epsilon = 1$. For the construction of the spherical cell, a minimal radius of $r_0 = 10^{-4}$ and a maximal radius of $r_{\text{BS}} = 3$ was used, which is a valid approximation for the usual muffin-tin radius of gold. The differential equations (6.47) and (6.48) for the COULOMB potential (7.1) were solved by using the methods illustrated in Table 6.2.

The numerical solutions obtained by using different solvers were compared with a reference solution, which was obtained by using *ode113* and very high accuracy goals. For the solvers taken from the *Matlab ode-suite* absolute and relative tolerances were chosen to be equal and values between 10^{-1} and 10^{-10} were used. The maximal relative error of the numerical solution in comparison to the reference solution was plotted as a function of the evaluations of the right-hand side of the differential equation (see Figure 7.6). First of all, it can be verified that the numerical accuracy for obtaining the regular single-site scattering solution is similar to the results of the irregular single-site scattering solution. Hence, the following statements can be given for both solutions. The *Matlab* solvers *ode113* and *ode15s* are well established implementations using multi-step methods with variable step size and variable order [158, 159]. By comparing the performance of *ode113*, which is a method capable for non-stiff equations, with the performance of the implicit method *ode15s* which is reasonable for stiff equations it is possible to conclude if the underlying differential equations are stiff. As soon as one deals with coupled first order equations, stiffness occurs if there are two or more very different scales of the independent variable on which the dependent variables are changing [92, pp. 727-731]. However, following SÖDERLIND *et al.* [178], a precise mathematical definition of stiffness is not present yet, but the historical and intuitive meaning can be summarized by:

Stiff equations are equations where certain implicit methods, in par-

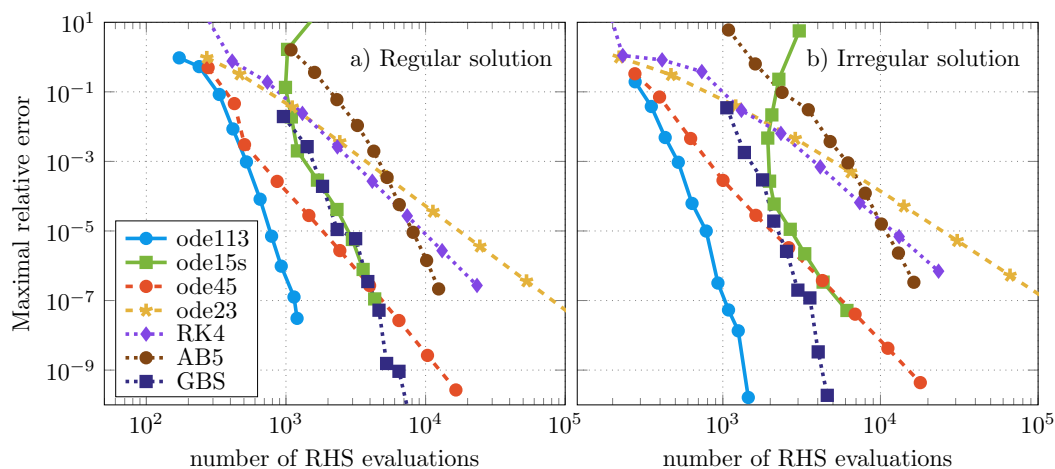


Figure 7.6.: Maximal relative error versus number of right-hand side (RHS) evaluations of the DIRAC equation for a COULOMB potential using different methods for the solution (see Table 6.2). The method *AB5* was implemented within *Hutsepot*.

ticular BDF¹, perform better, usually tremendously better, than explicit ones.

According to Figure 7.6, the opposite behaviour for the numerical solution of the DIRAC equation for a COULOMB potential is observed, since the method *ode15s* needs to evaluate the right hand-side of the differential equation at least five times as many as the method *ode113*. Therefore, the underlying differential equations can be characterized as non-stiff. The performance of the DORMAND-PRINCE method (*ode45*) is very good for crude tolerances and becomes comparable to *ode15s* for fine tolerances. The ADAMS-BASHFORTH-MOULTON predictor-corrector method of order 5 with a fixed step size (*AB5*) is rather expensive for high tolerances. But, due to the higher order, the performance is better in comparison to the methods of the RUNGE-KUTTA type *ode23* and *RK4*, if high accuracy goals are demanded. Also, in comparison to *ode45*, which has the same order, less evaluations of the right-hand side of the differential equation for high accuracy goals are necessary; it is therefore more efficient. The implemented GRAGG-BULIRSCH-STOER method with both adaptive order and step-size (*GBS*) [163] is able to solve the differential equations with very high orders. But, for the accuracy goals in practice ($\approx 10^{-8}$) it needs about five times as many evaluations of the right hand side of the differential equation in comparison to *ode113*.

¹BDF is an abbreviation for backward differentiation formulas [35, pp. 323-333].

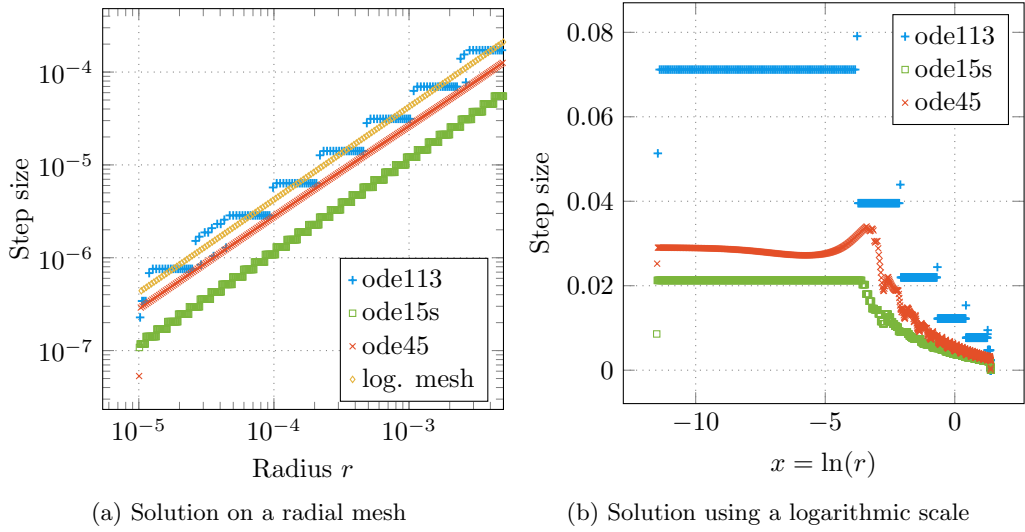


Figure 7.7.: Step size for the solution of the Coulomb-Dirac problem using adaptive methods.

In many implementations of the KKR method, solvers with fixed step size are used for spherically symmetric atomic potentials, whereas a logarithmic mesh of type $x = \log(r)$ or similar is employed [34]. The reason for this is that the wave functions are highly oscillating close to the nucleus, and are smooth for larger values of r . To verify that a logarithmic mesh is a reasonable choice, the step size for adaptive methods close the origin was investigated (see Figures 7.7a and 7.7b). The step size during the numerical solution of the COULOMB-DIRAC problem using *ode113*, *ode15s*, and *ode45* is shown in Figure 7.7a and compared with the step size of a logarithmic mesh. It can be verified that the step size used by *ode45* is similar to the characteristic of a logarithmic mesh. However, the stair-case-like behaviour of *ode113* and *ode15s* occurs due to the step-size strategy of the method itself, i.e. the change of the step-size is avoided as much as possible [158]. Analogously, it is possible to transform the differential equations (7.10) and (7.11) to a logarithmic scale $x = \log(r)$ and to investigate the varying step size of the methods *ode113*, *ode15s* and *ode45* for the numerical solution of the transformed equations. As shown in Figure 7.7b, all three solvers adopt a constant step size close to the origin ($x < -5$), which again reassures the choice of a logarithmic scale for methods with a fixed step size.

With the help of the Fortran solver based on the ADAMS-BASHFORTH-MOULTON method the accuracy of the single-site scattering t-matrix was investigated, which can be calculated after obtaining the regular single-site scattering solution numerically. The differential equations were solved for an energy of $\epsilon = 1$, a maximal angular

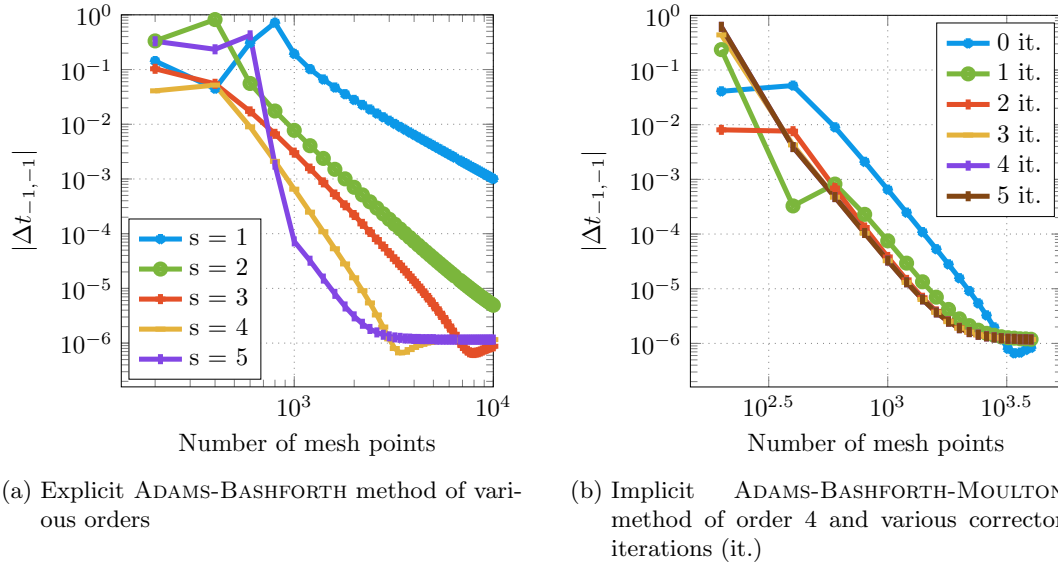


Figure 7.8.: Relative deviation of the s -electron contribution ($\kappa = -1$) of the single-site scattering t-matrix $|\Delta t_{-1,-1}|$ calculated with an explicit ADAMS-BASHFORTH method and an implicit ADAMS-BASHFORTH-MOULTON method.

momentum quantum number of $l = 3$ and an uranium potential with an atomic number of $Z = 92$. In Figure 7.8a the relative deviation of the s -electron contribution ($\kappa = -1$) of the single-site scattering t-matrix $|\Delta t_{-1,-1}|$ for an increasing number of radial mesh points is illustrated for the explicit ADAMS-BASHFORTH method of various orders without an application of an implicit corrector. Within this example, the accuracy saturates for an value of $\approx 10^{-6}$ which can be achieved using ≈ 1500 mesh points and order 5. The deviation of the t-matrix for lower orders can be decreased by applying an implicit ADAMS-MOULTON corrector step, as can be seen in Figure 7.8b. The corrector step can be applied m times, until the solution converges. In the present example, the solution converges after three iterations.

8. The relativistic Mathieu problem

8.1. Introduction

A reasonable test for a full-potential KKR method is given by the solution of the SCHRÖDINGER equation or the DIRAC equation for the periodic MATHIEU potential,

$$V(\mathbf{r}) = -U_0 (\cos(ax) + \cos(ay) + \cos(az)). \quad (8.1)$$

For the non-relativistic full-potential KKR method, band structure calculations for the MATHIEU potential were communicated by YEH *et al.* [179]. A test of the implemented relativistic full-potential method within the computer program *Hutsepot* will be discussed in the following. After the expansion of the MATHIEU potential into spherical harmonics is derived in the first section, a discussion for the numerical accuracy follows. It will be seen that the ADAMS-BASHFORTH-MOULTON predictor-corrector method is a reasonable choice for the solution of the differential equations. Therefore, the method is used within *Hutsepot* where the calculation of the band structure is possible in terms of the BLOCH spectral function. A comparison of the analytical and the numerical band structure follows in the last part.

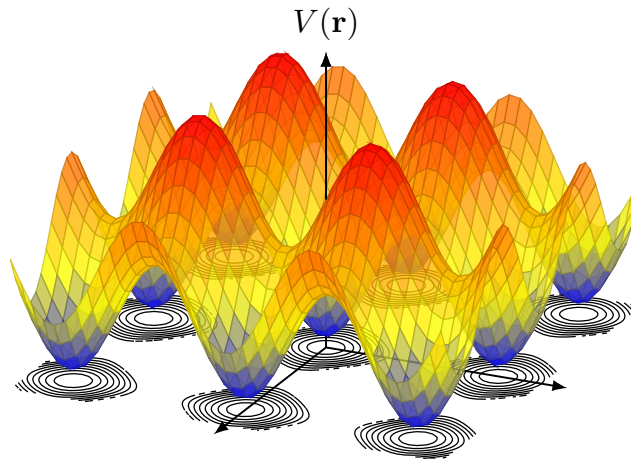


Figure 8.1.: The MATHIEU potential in two dimensions.

8.2. Expansion of the Mathieu potential into spherical harmonics

For the solution of the differential equations of the single-site scattering problem (6.9) and (6.10) it is necessary to transform the MATHIEU potential from Cartesian coordinates (8.1) to spherical polar coordinates and to expand the MATHIEU potential into spherical harmonics to calculate the potential matrices $\tilde{V}^+(r)$ and $\tilde{V}^-(r)$ according to Section 6.3.2. Both can be achieved by the following idea [180]. By rewriting equation (8.1) in exponential form,

$$V(\mathbf{r}) = -\frac{U_0}{2} (e^{iax} + e^{-iax} + e^{iay} + e^{-iay} + e^{iaz} + e^{-iaz}) \quad (8.2)$$

it is possible to apply BAUER's identity,

$$e^{i\mathbf{k}\cdot\mathbf{r}} = 4\pi \sum_{l=0}^{\infty} \sum_{m=-l}^l i^l j_l(kr) Y_l^m(\hat{\mathbf{r}}) Y_l^m(\hat{\mathbf{k}})^*, \quad (8.3)$$

which already gives an expansion by means of spherical harmonics. Introducing the vectors $\mathbf{k}_x = (a, 0, 0)$, $\mathbf{k}_y = (0, a, 0)$ and $\mathbf{k}_z = (0, 0, a)$ it is possible to replace the exponential functions of equation (8.2) according to (8.3). Using the behaviour of spherical harmonics under the application of the inversion operation,

$$\hat{P}(l) Y_l^m = (-1)^l Y_l^m, \quad (8.4)$$

each pair of \mathbf{k}_i and $-\mathbf{k}_i$ can be replaced by

$$e^{i\mathbf{k}_i\cdot\mathbf{r}} + e^{-i\mathbf{k}_i\cdot\mathbf{r}} = 8\pi \sum_{l=0}^{\infty} \sum_{m=-l}^l \cos\left(l\frac{\pi}{2}\right) j_l(ar) Y_l^m(\hat{\mathbf{r}}) Y_l^m(\hat{\mathbf{k}}_i)^*. \quad (8.5)$$

To calculate exact values of $Y_l^m(\hat{\mathbf{k}}_i)$ the associated angles ϑ and φ for \mathbf{k}_x , \mathbf{k}_y , \mathbf{k}_z are tabulated in Table 8.1, where $a > 0$ is assumed. For the given angles, values of $Y_l^{-m}(\hat{\mathbf{k}})$ can be calculated by taking analytic expressions for the spherical harmonics, which can be found in the book of VARSHALOVICH *et al.* [181, p. 158],

$$Y_l^m(0, \phi) = \delta_{m,0} \sqrt{\frac{2l+1}{4\pi}}, \quad (8.6)$$

$$Y_l^m\left(\frac{\pi}{2}, \phi\right) = \begin{cases} (-1)^{\frac{l+m}{2}} e^{im\phi} \sqrt{\frac{2l+1}{4\pi} \frac{(l+m-1)!! (l-m-1)!!}{(l+m)!! (l-m)!!}} & m \text{ is even} \\ 0 & m \text{ is odd} \end{cases}. \quad (8.7)$$

Finally, the expansion of the MATHIEU potential into spherical harmonics can be

\mathbf{k}	ϑ	φ
$(a, 0, 0)$	$\frac{\pi}{2}$	0
$(0, a, 0)$	$\frac{\pi}{2}$	$\frac{\pi}{2}$
$(0, 0, a)$	0	0

Table 8.1.: The associated values of ϑ and φ for the different \mathbf{k} -vectors.

written in the following compact form,

$$V(\mathbf{r}) = -\sqrt{4\pi}U_0 \sum_{l=0}^{\infty} \sum_{m=-l}^l \cos\left(l\frac{\pi}{2}\right) \sqrt{2l+1} [\delta_{m,0} + f_{lm}] j_l(kr) Y_l^m(\hat{\mathbf{r}}). \quad (8.8)$$

In the above equation, the algebraic coefficients f_{lm} are given by

$$f_{lm} = \begin{cases} \left((-1)^{\frac{m}{2}} + 1\right) (-1)^{\frac{l}{2}} \sqrt{\frac{(l+m-1)!! (l-m-1)!!}{(l+m)!! (l-m)!!}} & m \text{ is even} \\ 0 & m \text{ is odd} \end{cases}. \quad (8.9)$$

The expansion coefficients of equation (8.8) are given in terms of the spherical BESSEL functions $j_l(ar)$.

8.3. Numerical accuracy

Analogously to Section 7.4, where the numerical accuracy was discussed for the COULOMB potential, the *Matlab* implementation of the single-site scattering solver is used to discuss the numerical solution of the differential equations (6.47) and (6.48) for the MATHIEU potential [Ge2]. Analogously to YEH *et al.* [179], the lattice constant was chosen to be $a = 2\pi$ and the pre-factor U_0 was set to $U_0 = -0.5$. The expansion of the solution in terms of spin-angular functions was evaluated up to an maximal angular momentum quantum number of $l_{\max} = 5$. Due to the high value of l_{\max} the matrices \tilde{P} and \tilde{Q} in (6.9) and (6.10) are of dimension 72×72 . For the investigation of the numerical accuracy the methods illustrated in Table 6.2 were taken into account.

Analogously to Section 7.4, the numerical solutions obtained by using different solvers were compared with a reference solution, which was obtained by applying *ode113* and very high accuracy goals. The results by means of maximal relative error versus number of evaluations of the right-hand side of the differential equation are shown in Figure 8.2. Whereas the general behaviour of the different methods

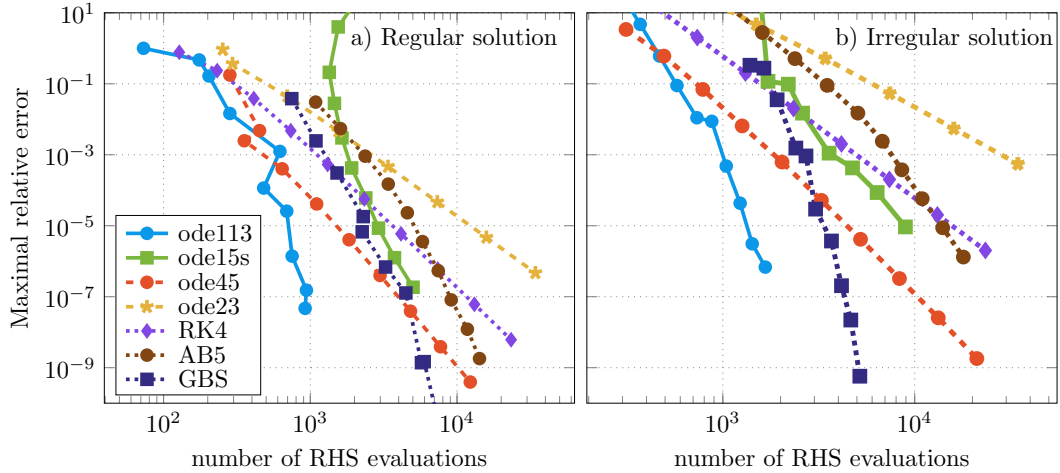


Figure 8.2.: Maximal relative error versus evaluations of the right-hand side of the DIRAC equation for a MATHIEU potential using different methods for the solution (see Table 6.2). The method *AB5* was implemented within *Hutsepot*.

compared to each other is similar for regular and irregular single-site scattering solutions, it can be verified that for a particular method and the same number of evaluations of the right-hand side of the differential equation the maximal relative error for the regular solution is smaller in comparison to the irregular solution by approximately 2 orders of magnitude, which is due to the very high absolute values of the irregular single-site scattering solutions close to the origin. Analogously to the discussion of the COULOMB potential in Section 7.4, the underlying differential equations for the MATHIEU potential can be regarded as non-stiff, since the performance of the method *ode113* is much better than the performance of the implicit method *ode15s* [178]. Furthermore, the performance of the ADAMS-BASHFORTH-MOULTON predictor-corrector method of order 5 (AB5) is worse than the explicit RUNGE-KUTTA methods RK4 and *ode45* for crude tolerances but becomes more efficient if high accuracy goals are required, which is in agreement with the results of Section 7.4 as well. Especially for the irregular solutions *ode23* fails to give a reasonable solution for an appropriate amount of evaluations of the right-hand side of the differential equation.

The differential equations (6.47) and (6.48) are characterized by the effective potential. Since the MATHIEU potential is known analytically, methods with adaptive step-size like *ode113* are a reasonable choice. In general, the effective potential within each iteration of the KKR method is given on a discrete mesh. Thus, a method with

a fixed step size is appropriate, since interpolations of the potential between mesh points are avoided. For the MATHIEU potential, it can be verified (see Figure 8.2) that the numerical solution of the full-potential single-site scattering problem can be obtained by linear multi-step methods for non-stiff equations, e.g. by applying an ADAMS-BASHFORTH-MOULTON predictor-corrector method. Therefore, the method *AB5* was implemented within the computer code *Hutsepot*.

Next to the solution via differential equations, the solution of the DIRAC equation for a MATHIEU potential was investigated by means of integral equations. The implementation was done analogously to the publication of HUHNE *et al.* [30] (for details see [Ge2]). For the integration, the trapezoidal rule as well as the SIMPSON rule [182, pp. 309] was used. In Figure 8.3 the maximal relative error of the solution is plotted versus the number of iterations within the BORN series for the solution of the LIPPMANN-SCHWINGER equation. It can be seen that the maximal relative error saturates quickly and the Born series converges after three iterations. This is in perfect agreement with the observation of Drittler [7] for the non-relativistic method.

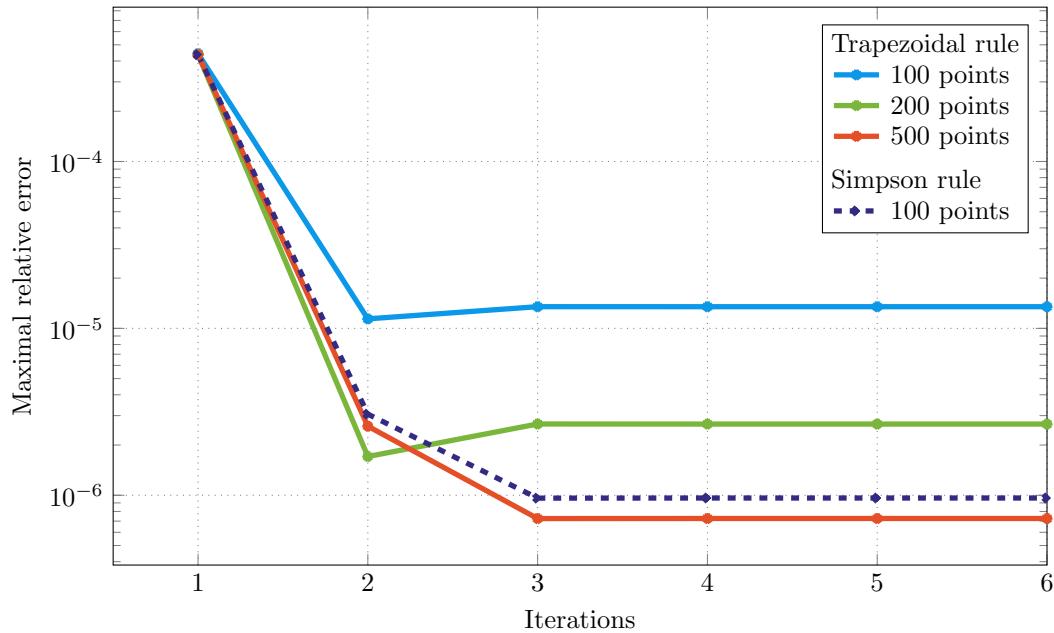


Figure 8.3.: Maximal relative error versus number of iterations within the BORN series for the solution of the DIRAC equation for a MATHIEU potential by means of integral equations.

Since the deviation from the exact solution is dominated by the error of the numerical quadrature, the accuracy of the solution can be improved by either increasing the number of mesh points for the quadrature or by improving the integration scheme, e.g. using the Simpson rule instead of the trapezoidal rule. In this way the maximal relative error can be decreased by about one order of magnitude for the same number of points, where the integrand is evaluated.

8.4. Band structure

In Section 8.3 it was shown that the ADAMS-BASHFORTH-MOULTON predictor corrector method can be used to solve the DIRAC equation for a MATHIEU potential. Therefore, this method was implemented within the computer code *Hutsepot*. To test the full-potential implementation the band structure for the MATHIEU problem was calculated by means of the relativistic version of the BLOCH spectral function (compare equation (2.12)),

$$A_B(\mathbf{k}, W) = -\frac{1}{\pi} \text{Im Tr} \left[\sum_{\mathbf{R}_j \in L} e^{i\mathbf{k} \cdot \mathbf{R}_j} \int d^3 r_j \tilde{G}(\mathbf{r}_j, \mathbf{r}_j + \mathbf{R}_j, W) \right]. \quad (8.10)$$

The results for different values of l_{\max} are presented in Figure 8.4. Again, the values $a = 2\pi$ for the lattice constant as well as $U_0 = -0.5$ for the strength of the potential were taken. To achieve sharp bands within the plot of the BLOCH spectral function a small imaginary part of the complex energy $\delta = 10^{-3}$ was used as well as a large number of energy points, $N_E = 800$. Furthermore, to compare the BLOCH spectral function, a second band structure was calculated using a plane-wave approach [180]. Since the MATHIEU potential itself is given as a linear combination of plane waves (8.2), this approach converges rapidly and gives accurate results. It can be seen that high values of l_{\max} are needed for the calculation of the BLOCH spectral function, to obtain a result, comparable to the plane-wave band structure. However, high values of l_{\max} are critical within a full potential method, since the evaluation of the potential into spherical harmonics has to be performed up to $l_{\text{pot}} = 2l_{\max}$ and according to equation (6.15) the shape-truncation functions has to be evaluated up to an maximal angular momentum quantum number of $l_{\text{shape}} = 2l_{\text{pot}} = 4l_{\max}$. Nevertheless, the BLOCH spectral function for $l_{\max} = 4$ reflects the general behaviour of the plane-wave band structure. Problems occur especially for high energy values, where undesired splitting of energy bands can be found.

Still, it has to be pointed out that the reasonable calculation of the energy bands by means of the newly developed code within *Hutsepot* does not only verify the successful implementation of a solver for the relativistic single-site scattering problem for non-spherical potentials, but also the proper implementation of the multiple-scattering

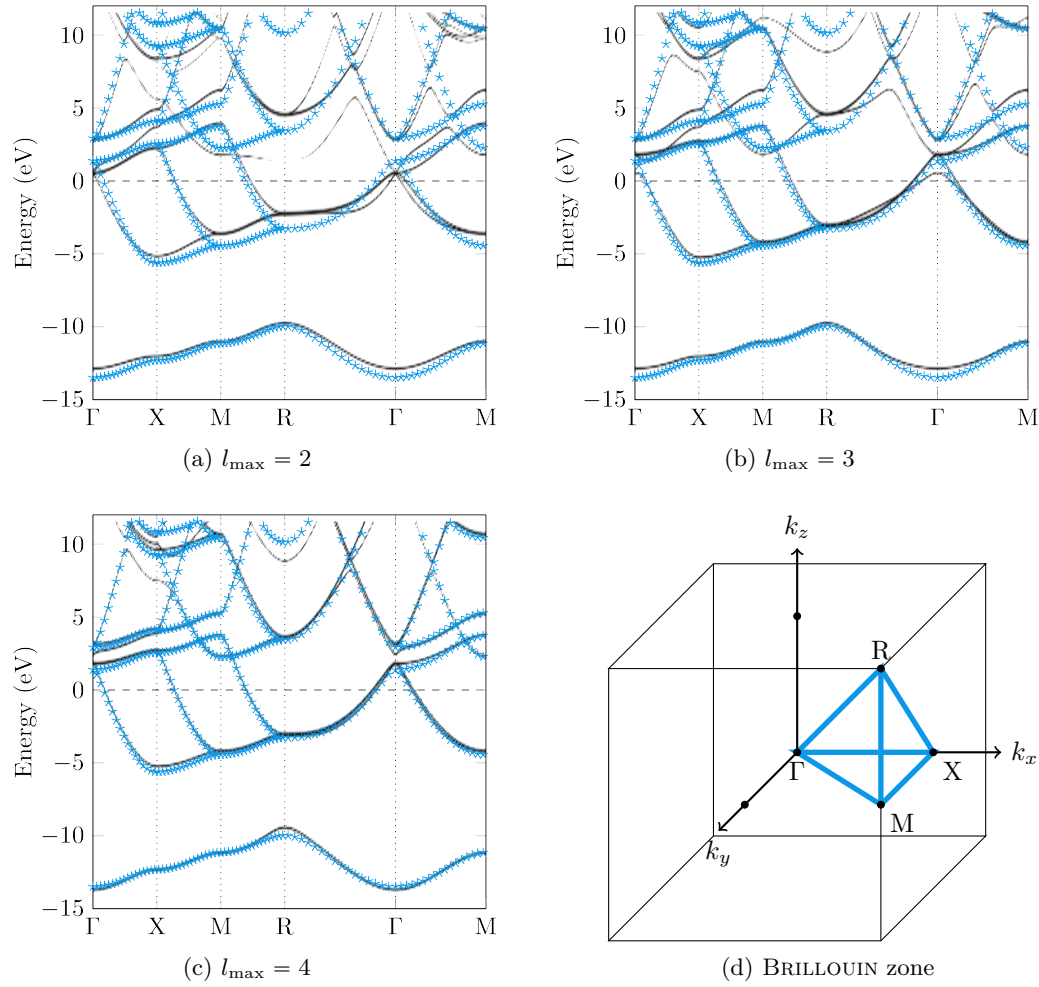


Figure 8.4.: Comparison of the relativistic BLOCH spectral function calculated with *Hutsepot* (black) and a band structure calculated by means of a plane-wave approach (blue) for the MATHIEU potential.

formalism of the KKR method. Furthermore, it ensures the correct calculation of the shape truncation function, which is needed for the computation of the BLOCH spectral function.

9. The electronic structure of PbTe and SnTe

9.1. Introduction

Investigations of tellurides, especially lead telluride (PbTe) and tin telluride (SnTe) have been performed for decades. Alloys of both materials ($\text{Pb}_x\text{Sn}_{1-x}\text{Te}$) were widely used as infrared detectors during the late 1960s and early 1970s [37]. Although, $\text{Pb}_x\text{Sn}_{1-x}\text{Te}$ detectors are easy to prepare and very stable, they were replaced by $\text{Hg}_x\text{Cd}_{1-x}\text{Te}$ devices later on. During the 1990s, $\text{Pb}_x\text{Sn}_{1-x}\text{Te}$ on Silicon (Si) was investigated for the usage as a photovoltaic infrared sensor [183]. Furthermore, PbTe and SnTe play an important role in the fabrication of thermoelectric materials. Especially by alloying, e.g. with bismuth (Bi) or antimony (Sb) a high figure of merit can be reached [184, 185]. Recently, SnTe attracted great attention due to its electronic structure. In comparison to other semiconducting materials, band inversion at the L-point can be seen. This particular property lead to the experimental realization of a topological crystalline insulator in 2012 [38, 39]. The band inversion at the L-point for SnTe is a relativistic effect and is caused by spin-orbit coupling. Within this chapter, the electronic structure of SnTe and PbTe is discussed as it was calculated by means of the relativistic extension of *Hutsepot*. Furthermore it will be shown that band inversion can be controlled by alloying of SnTe and PbTe as well as by applying hydrostatic pressure or uniaxial strain.

9.2. Crystal structure

At room temperature, both materials PbTe and SnTe occur in rock salt structure with the space group $\text{Fm}\bar{3}\text{m}$ (225). An illustration of the crystal structure can be found in Figure 9.1a, where the blue atoms represent the cation (Pb, Sn) and the red atoms the anion (Te). The primitive cell of the structure is shown in Figure 9.1b. To obtain better convergence properties within the KKR method two additional empty spheres were added. For the rock salt crystal structure, only one independent lattice constant a has to be determined. The equilibrium lattice constants were calculated using the VASP code together with the PBEsol-GGA exchange correlation functional [88]. In comparison to the experiment, larger values are achieved, meaning 6.560\AA for PbTe and 6.408\AA for SnTe [186]. Taking into account spin-orbit coupling,

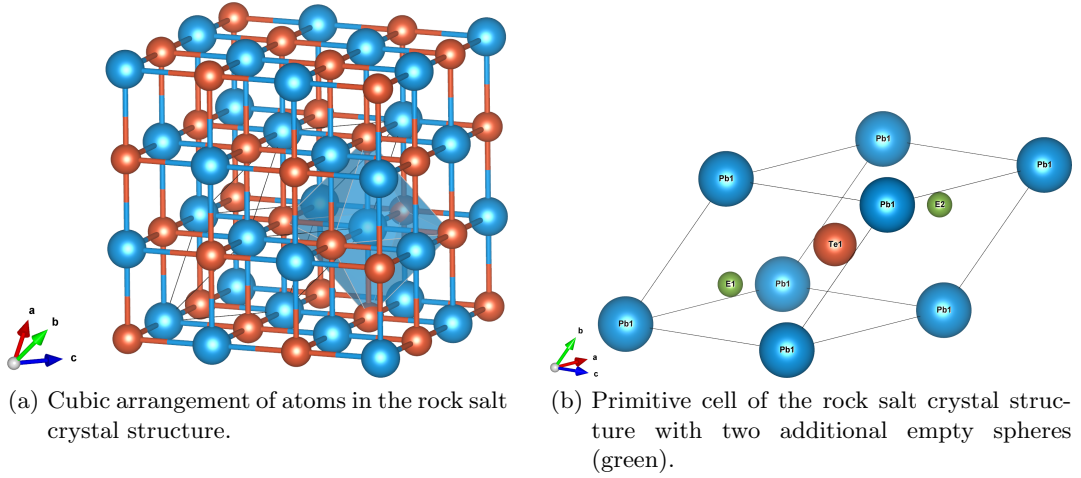


Figure 9.1.: The rock salt crystal structure of $\text{Pb}_x\text{Sn}_{1-x}\text{Te}$ [80].

the values of the lattice constants slightly increase to 6.562\AA for PbTe and 6.410\AA for SnTe. The estimated lattice constants are in good agreement with the experimental values [187], which are given by 6.461\AA and 6.318\AA , for PbTe and SnTe, respectively.

9.3. Computational methods

The electronic structure calculations were performed using *Hutsepot*. The atomic potentials of the scattering centres were obtained self-consistently by applying the scalar relativistic approximation [83, 84] together with the atomic sphere approximation [135]. The evaluation of the Green function in terms of spherical harmonics was expanded up to a maximal angular momentum of $l = 3$. The energy contour along the complex energy plane consisted of 24 points. As an approximation for the exchange-correlation functional the LibXC[89] implementation of PBE [188] was used, which is a generalized gradient approximation. To properly simulate the $\text{Pb}_{1-x}\text{Sn}_x\text{Te}$ alloy the coherent-potential approximation (see Section 2.2) was applied. Band structures were calculated in terms of the Bloch spectral function (see equation (8.10)) by using a fully-relativistic KKR method based on the solution of the Dirac equation [Ge2].

9.4. Electronic structure

Both materials SnTe and PbTe are narrow band gap semiconductors. Experimental values for the band gap are between 0.19 eV and 0.32 eV for PbTe and between 0.2 eV and 0.3 eV for SnTe [189, 190, 191]. Illustrations of the BLOCH spectral function

of PbTe and SnTe, calculated using the fully-relativistic KKR method can be seen in Figure 9.2. Regarding PbTe, the states directly below the FERMI energy can be allocated to the p -states of tellurium (Te) whereas the states directly above the FERMI energy are p -states of lead (Pb). The band gap occurs at the L-point, as it can be seen in Figure 9.2a and Figure 9.2b. The band structure of SnTe is illustrated in Figure 9.2c. Again, the band gap is located at the L-point, but resolving the contribution of Sn and Te to the band structure according to Figure 9.2d it can be verified that an inverted behaviour in comparison to PbTe is observed. That means, close to the L-point p -states of Sn and p -states of Te are interchanged in a small region about the FERMI energy. Since the band inversion property of SnTe is

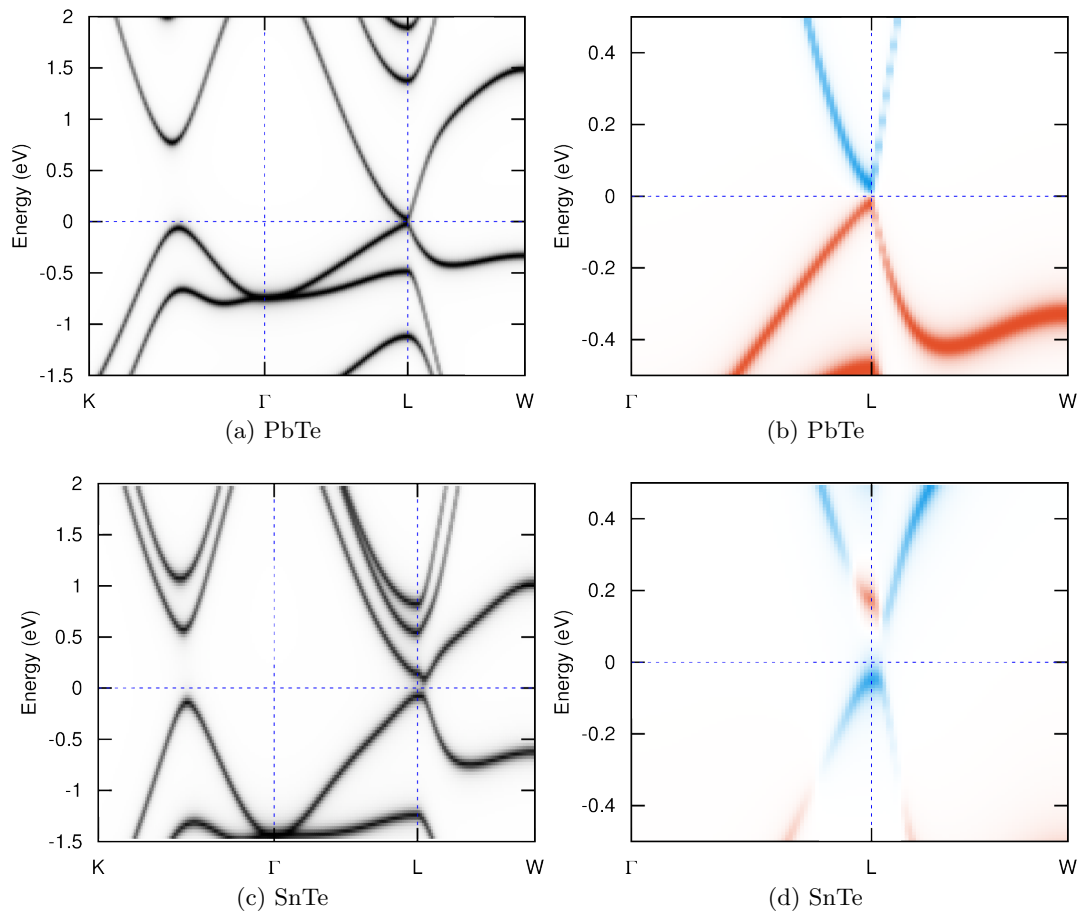


Figure 9.2.: Band structure of PbTe and SnTe calculated using a fully-relativistic KKR method. The Figures (b) and (d) show the site resolved Bloch spectral function. Yellow denotes the anion contribution (Te) and black the cation contribution (Pb, Sn).

very important for the realization of crystalline topological insulators [39], it will be illustrated during the next section, how this property can be tuned by alloying and by applying hydrostatic pressure.

9.5. Influence of alloying and hydrostatic pressure on band inversion

To better understand the band inversion property of SnTe, the band gap energy for the alloy $\text{Pb}_x\text{Sn}_{1-x}\text{Te}$ was investigated for different concentrations x and different lattice parameters between 6.3\AA and 6.7\AA . The band gap energy was estimated by calculating the BLOCH spectral function at the L-point within a small energy region $[E_F - \Delta, E_F + \Delta]$ ($\Delta \approx 0.2\text{eV}$) about the FERMI energy E_F using $N_E = 700$ energy points and a small imaginary part for the energy ($\delta \approx 10^{-4}$) to get sharp peaks. Since the GREEN function in LEHMANN representation has the form

$$G(E) = \sum_m \frac{|m\rangle\langle m|}{E - E_m + i\delta}, \quad (9.1)$$

and the BLOCH spectral function is defined as the \mathbf{k} resolved imaginary part of the GREEN function, it is reasonable to fit the peaks of the BLOCH spectral function using a LORENTZian function [192]

$$L(E) = \frac{1}{\pi} \frac{C}{(E - E_0)^2 + C^2}. \quad (9.2)$$

Afterwards, the band gap energy can be calculated easily by taking the difference of the peak positions (E_0) of the two peaks next to the FERMI energy. Results of the band gap energies for different concentrations and different lattice parameters are illustrated in Figure 9.3. Negative values represent the results for an inverted band structure. All together the calculations were performed for 11 different concentrations and 20 different lattice parameters each, to produce a reasonable dataset. Since the described procedure fails in the region where the band gap changes sign, this array was interpolated using *Mathematica* to obtain a well defined curve with $E_g = 0$.

The equilibrium lattice constants of SnTe and PbTe are sketched via dashed vertical lines. Furthermore, they are connected via a third line which describes the change of the lattice constants according to the change of the concentration of Pb with respect to VEGARD's law [193], which is a reasonable approximation for binary systems, where alloying does not influence the space group of the crystal. Following the line of VEGARD's law from PbTe to SnTe, it can be seen that with increasing amount of Sn the band gap energy decreases until the band gap vanishes for a Pb

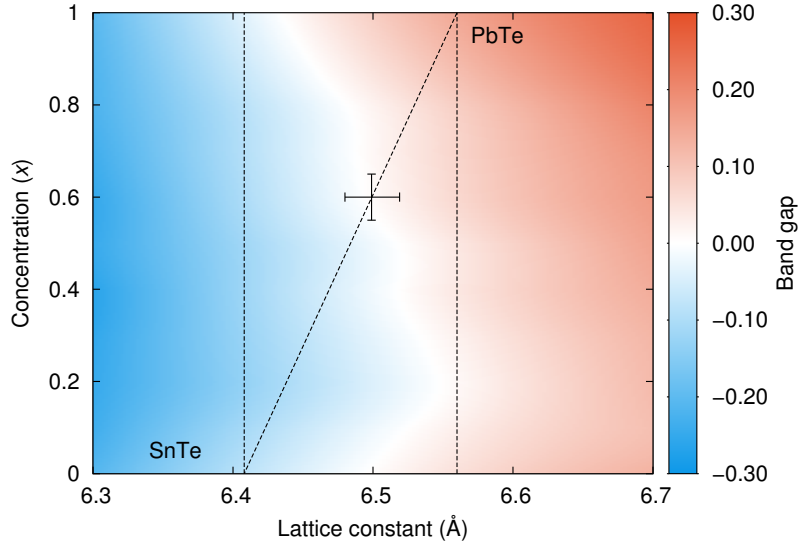


Figure 9.3.: The band gap energy as a function of the lattice constant and the concentration x of a $\text{Pb}_x\text{Sn}_{1-x}\text{Te}$ alloy.

concentration of $x \approx 60\%$. Lowering the lead concentration furthermore will increase the band gap again, but with an inverted band characteristic at the L-point. Hence, the size of the band gap as well as the band characteristic of $\text{Pb}_x\text{Sn}_{1-x}\text{Te}$ can be tuned with changing the concentration of Pb. Comparable results can be found in the literature e.g. in the work of DIMMOCK *et al.* [194] or DIXON *et al.* [195]. The experimental results published in both works show a strong temperature dependence of the zero band gap concentration, which can not be modelled in a proper manner with the used methods.

Starting again with pure PbTe and leaving the concentration constant, a similar behaviour can be seen for compressing the crystal. Again, compression leads to a decrease of the band gap until the band gap vanishes at a lattice constant of about 6.42\AA . This value corresponds to a lowering of the lattice constant of about 2%, which can be obtained by applying a pressure of $\approx 4\text{ GPa}$ ¹. Further compression will open the band gap again but with inverted band characteristic. In general, compression of the $\text{Pb}_x\text{Sn}_{1-x}\text{Te}$ will lead to a stronger interaction between the electrons in the

¹The pressure was calculated from the MURNAGHAN equation of states, which is given by

$$p(V) = \frac{B_0}{B'} \left[\left(\frac{V}{V_0} \right)^{-B'} - 1 \right]. \quad (9.3)$$

The used values for the bulk modulus B_0 and for the derivation of the bulk modulus with respect to the pressure B' were obtained from calculating the total energy of PbTe and SnTe as a function of the volume and by fitting the data by means of the BIRCH-MURNAGHAN equation of states [196]. Results are given by $B_0 = 51.67\text{ GPa}$ and $B' = 4.5$ for PbTe and by $B_0 = 52.38\text{ GPa}$ and $B' = 4.44$ for SnTe.

valence band. This interaction leads to a shift of the energy levels and influences the size of the band gap.

9.6. Influence of uniaxial strain on band inversion

A similar approach like for the investigation of the influence of hydrostatic pressure on the band inversion property can be used to study the effect of applying uniaxial strain. According to Figure 9.3, the transition between inverted and non-inverted band gap occurs at a Pb concentration of 60 %. Therefore the concentrations 100 %, 90 %, 78 % and 60 % were chosen to investigate how uniaxial strain influences the band gap. For the calculations a cubic cell was chosen, where four Pb or Sn atoms and four Te atoms are present. The lattice vectors of the cell are given by $\mathbf{a} = (a, 0, 0)$, $\mathbf{b} = (0, b, 0)$ and $\mathbf{c} = (0, 0, c)$, whereas the relation $a_0 = b_0 = c_0$ holds for the equilibrium lattice constants. The cell was compressed or strained along the crystallographic \mathbf{c} -direction. To obtain the lattice constants a and b it was assumed that the volume of the unit cell is constant.

The band gap as a function of c for the above mentioned concentrations is shown in Figure 9.4. It can be verified that both, compression as well as strain leads to a lowering of the band gap. In both cases, band inversion can be triggered if the change

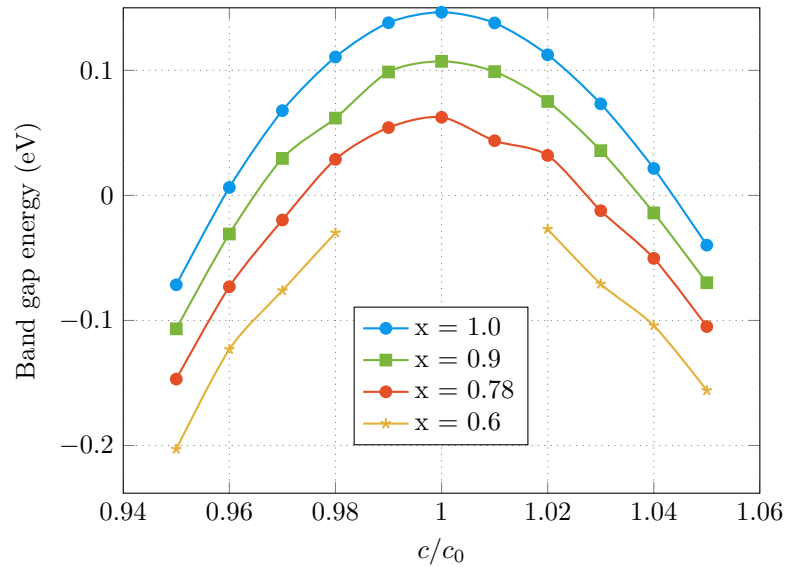


Figure 9.4.: Band gap energy of $\text{Pb}_x\text{Sn}_{1-x}\text{Te}$ versus change of the lattice constant c in units of the equilibrium lattice constant c_0 for various concentrations x of Sn.

of the lattice constant c is reasonably large. For pure PbTe the band gap vanishes for the values $c/c_0 \approx 0.96$ and $c/c_0 \approx 1.045$. By alloying, the band gap for the equilibrium lattice constants c_0 change and therefore the transition between inverted and non-inverted band characteristic already occurs for smaller deformations. For a Pb concentration of 60%, $\text{Pb}_x\text{Sn}_{1-x}\text{Te}$ is metallic at the equilibrium. By applying uniaxial strain an inverted band gap appears.

10. Summary

The main focus of the thesis was the implementation of a relativistic full-potential KORRINGA-KOHN-ROSTOKER GREEN function method within the computer program *Hutsepot*. The central part of the method is the solution of the single-site scattering problem, where the regular and the irregular scattering solutions are calculated, which are needed for the construction of the multiple-scattering GREEN function. In contrast to previous approaches [7, 30] these solutions were obtained by the direct solution of the underlying differential equations via using a linear multi-step method, which is possible without the definition of a certain cut-off radius close to the origin. To ensure that the solution can be obtained with reasonable accuracy, a comprehensive discussion of the numerics was conducted [Ge2], first, for a spherical COULOMB potential and, second, for a non-spherical MATHIEU potential. Furthermore, the asymptotic behaviour of the irregular single-site scattering solutions close to the origin was investigated and it could be shown that the non-relativistic limit of solutions with the quantum number $\kappa = -l - 1$ differs from the non-relativistic solutions with the associated quantum number l for $r \ll 1$.

Up to now, the relativistic implementation was used, i.e. for the study of electronic and magnetic properties of ultra-thin Co films on BaTiO₃ [Ge3], the investigation of magnetic properties in binary chalcogenides [Ge5] or the study of magnetic anisotropy of single rare-earth atoms on highly conducting surfaces [Ge6, Ge7]. As an example for the application of the relativistic method within this thesis, the band inversion property of SnTe at the L-point was discussed. By using the coherent potential approximation it could be shown that in addition to the size of the band gap the band inversion can be tuned by changing the concentration x within the alloy Pb_{*x*}Sn_{1-*x*}Te or by the application of hydrostatic pressure or uniaxial strain.

By using a scalar relativistic KKR method, the electronic and the magnetic structure of PrMnO₃ and CaMnO₃ was investigated. It could be verified that both materials are semiconductors with indirect band gap. For the magnetic structure, it could be shown that the manganese moments couple antiferromagnetically. The magnetic ordering is of the A-type for PrMnO₃ and of G-Type for CaMnO₃. In contrast to the reference work of JIRAK [96] who suggested low praseodymium moments $\approx 0.5 \mu_B$, the illustrated calculations predict the high-spin state of praseodymium with a magnetic moment of $2 \mu_B$ and a ferromagnetic coupling of praseodymium and manganese moments. This new approach to the magnetic structure has been measured in recent neutron-diffraction experiments [97].

In addition to the implementation of the fully-relativistic KKR method, a *Mathematica* group theory package *GTPack* was developed [Ge1]. Along with the different possibilities *GTPack* can be used for, it can be applied in the area of crystal field theory [Ge4]. Within this thesis, some of the developments related to crystal field theory were illustrated and the method was applied to single holmium atoms on a platinum (111) surface [Ge6]. By assuming that the valence electrons of holmium form a many particle state with the total angular momentum of 8, it has been shown that this state splits within the trigonal crystal field induced by the platinum surface and shows a two-fold degenerate ground state offering an expectation value of the magnetic moment of $\pm 8 \mu_B$ perpendicular to the surface. It has been shown analytically that the transition between both states is forbidden. Hence, high lifetimes can be expected.

Part IV.
Appendix

A. Density functional theory

For a non-relativistic quantum many-particle system with N_e electrons and N_c atomic cores, the associated SCHRÖDINGER equation is given by

$$\hat{H} \Psi_\nu(\mathbf{R}_1, \dots, \mathbf{R}_{N_c}, \mathbf{r}_1, \dots, \mathbf{r}_{N_e}) = E_\nu \Psi_\nu(\mathbf{R}_1, \dots, \mathbf{R}_{N_c}, \mathbf{r}_1, \dots, \mathbf{r}_{N_e}). \quad (\text{A.1})$$

The HAMILTON operator \hat{H} includes the kinetic energy of the cores \hat{T}_c and electrons \hat{T}_e as well as the core-core interaction V_{cc} , the core-electron interaction V_{ce} , and the electron-electron interaction V_{ee} ,

$$\hat{H} = \hat{T}_c + \hat{T}_e + \hat{V}_{cc} + \hat{V}_{ce} + \hat{V}_{ee}. \quad (\text{A.2})$$

Assuming that a core with the index i has the mass M_i , the atomic number Z_i , and is located at \mathbf{R}_i , and that an electron with the index j and mass m is located at \mathbf{r}_j , the terms of Equation (A.2) can be written as

$$\hat{T}_c = -\frac{\hbar^2}{2} \sum_{i=1}^{N_c} \frac{1}{M_i} \nabla_{\mathbf{R}_i}^2, \quad (\text{A.3})$$

$$\hat{T}_e = -\frac{\hbar^2}{2m} \sum_{i=1}^{N_e} \nabla_{\mathbf{r}_i}^2, \quad (\text{A.4})$$

$$\hat{V}_{cc} = \frac{1}{8\pi\epsilon_0} \sum_{i=1}^{N_c} \sum_{\substack{j=1 \\ j \neq i}}^{N_c} \frac{Z_i Z_j e^2}{|\mathbf{R}_i - \mathbf{R}_j|}, \quad (\text{A.5})$$

$$\hat{V}_{ce} = -\frac{1}{4\pi\epsilon_0} \sum_{i=1}^{N_c} \sum_{j=1}^{N_e} \frac{Z_i e^2}{|\mathbf{r}_i - \mathbf{R}_j|}, \quad \text{and} \quad (\text{A.6})$$

$$\hat{V}_{ee} = \frac{1}{8\pi\epsilon_0} \sum_{i=1}^{N_e} \sum_{\substack{j=1 \\ j \neq i}}^{N_e} \frac{e^2}{|\mathbf{r}_i - \mathbf{r}_j|}. \quad (\text{A.7})$$

Since the mass of the proton is about 1800 times larger than the mass of the electron it was pointed out by BORN and OPPENHEIMER [197] that the so-called adiabatic approximation can be applied, which separates the core and the electron solution,

$$\Psi_\nu(\mathbf{R}_1, \dots, \mathbf{R}_{N_c}, \mathbf{r}_1, \dots, \mathbf{r}_{N_e}) = \phi_\nu(\mathbf{r}_1, \dots, \mathbf{r}_{N_e}; \mathbf{R}_1, \dots, \mathbf{R}_{N_c}) \eta_\nu(\mathbf{R}_1, \dots, \mathbf{R}_{N_c}). \quad (\text{A.8})$$

In the above equation, Φ_ν is a N_e -electron wave functions which depends on the variables \mathbf{r}_i and contains the core coordinates \mathbf{R}_j as parameters. Φ_ν can be calculated by solving the associated electron SCHRÖDINGER equation,

$$\left(\hat{T}_e + \hat{V}_{ce} + \hat{V}_{ee} + E_c\right) \Phi_\nu(\mathbf{r}_1, \dots, \mathbf{r}_{N_e}) = E_\nu \Phi_\nu(\mathbf{r}_1, \dots, \mathbf{r}_{N_e}). \quad (\text{A.9})$$

Here, E_c denotes the core-core interaction for a fixed set of vectors \mathbf{R}_i . Due to the electron-electron interaction V_{ee} , a coupling between all independent variables $\mathbf{r}_1, \dots, \mathbf{r}_{N_e}$ in equation (A.9) occurs, and therefore it is not possible to solve it analytically. However, imagining it is possible to solve equation (A.9) numerically for an oxygen atom on a crude Cartesian grid with 10 points in each direction. Since oxygen has 8 electrons the wave function is stored on $(10^3)^8 = 10^{24}$ points. The wave function is complex-valued and a complex single-precision variable needs 8 B of memory. Hence, the crude solution would need $\approx 10^{25}$ B = 10^{13} TB of memory, which is impossible on nowadays computers.

An elegant way to overcome this circumstance is given by the approach of density functional theory. Instead of concentrating on the wave function which depends on N_e position vectors, it is the goal to concentrate on the ground state density of a system which depends on one position vector and which is a real valued quantity. The mathematical background of the theory is given by the two theorems of HOHENBERG and KOHN [198], which can be formulated in the following way:

1. For an interacting electron system, the external potential $V_{\text{ext}}(\mathbf{r})$ is uniquely defined up to a constant by the ground state density $n_0(\mathbf{r})$.
2. The total energy $E[n]$ has a global minimum for the ground state density n_0 , meaning

$$E[n] \geq E[n_0] = E_0 \quad (\text{A.10})$$

Furthermore, for every chosen density $n(\mathbf{r})$, it is essential that $n(\mathbf{r}) \geq 0$ and $\int d^3\mathbf{r} n(\mathbf{r}) = N$.

The original proof of the theorems relies on a non-degenerate ground state. However, it can be shown that the theorems are also valid for a degenerate ground state [47, pp. 18]. Important extensions are the time-dependent density functional theory [199], the current density functional theory [200] as well as the relativistic density functional theory [201, 202].

To obtain the ground state density $n_0(\mathbf{r})$ the approach of KOHN and SHAM [203] can be used, where the interacting N particle system with a known potential is mapped to a non-interacting N particle system with an effective unknown potential $V_{\text{eff}}(\mathbf{r})$, but with the same ground-state density. In general, the effective potential $V_{\text{eff}}(\mathbf{r})$ can be constructed from the external potential $V_{\text{ext}}(\mathbf{r})$ the HARTREE potential

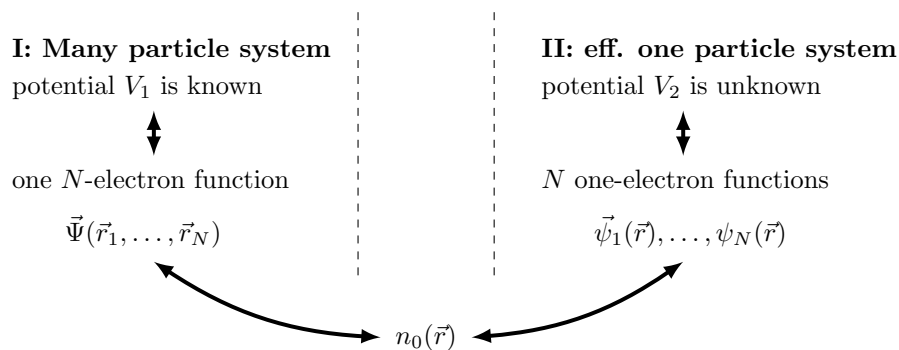


Figure A.1.: Illustration of the KOHN-SHAM approach, where a interacting N particle system is related to an effective one-particle system with the same ground-state density.

$V_{\text{H}}(\mathbf{r})$ and the exchange-correlation potential $V_{\text{xc}}(\mathbf{r})$, which leads to the effective one-particle KOHN-SHAM equation for the KOHN-SHAM wave-function $\psi_{i\sigma}(\mathbf{r})$ with the spin quantum number σ ,

$$\left[-\frac{\hbar^2}{2m} \nabla^2 + V_{\text{ext}}(\mathbf{r}) + V_{\text{H}}([n]; \mathbf{r}) + V_{\text{xc}}([n_{\uparrow}, n_{\downarrow}]; \mathbf{r}) \right] \psi_{i\sigma}(\mathbf{r}) = \epsilon_{i\sigma} \psi_{i\sigma}(\mathbf{r}). \quad (\text{A.11})$$

An illustration of the idea can be found in Figure A.1. The external potential $V_{\text{ext}}(\mathbf{r})$ includes the electron-core interaction as well as the external magnetic field. The HARTREE potential represents the electron-electron interaction and is given by

$$V_{\text{H}}([n]; \mathbf{r}) = -\frac{1}{4\pi\epsilon_0} \int d^3\mathbf{r}' \frac{n(\mathbf{r}')}{|\mathbf{r} - \mathbf{r}'|}. \quad (\text{A.12})$$

Whereas equations for calculating the external potential and the HARTREE potential can be derived analytically, an exact expression for the exchange-correlation functional is not known. However, two famous approximations will be mentioned at the end of this section.

The electron density for each spin state σ can be estimated by summation over KOHN-SHAM-orbitals $\psi_{i\sigma}$, according to

$$n_{\sigma}(\mathbf{r}) = \sum_i^{\text{occ.}} |\psi_{i\sigma}(\mathbf{r})|^2. \quad (\text{A.13})$$

From the spin polarized electron densities n_{\uparrow} and n_{\downarrow} , the total electron density can be calculated according to

$$n(\mathbf{r}) = n_{\uparrow}(\mathbf{r}) + n_{\downarrow}(\mathbf{r}). \quad (\text{A.14})$$

In the same manner, the magnetisation density can be derived via

$$m(\mathbf{r}) = n_{\uparrow}(\mathbf{r}) - n_{\downarrow}(\mathbf{r}). \quad (\text{A.15})$$

The KOHN-SHAM Equation (A.11) is exact if the exchange-correlation potential $V_{\text{xc}}([n_{\uparrow}, n_{\downarrow}]; \mathbf{r})$ is known. Unfortunately this is not the case and therefore reasonable approximation for the exchange-correlation potential have to be found. Such approximations can be obtained, e.g. by finding functionals which reflect the results obtained by means of quantum Monte Carlo calculations [204]. If the electron density is slowly varying it can be described locally by the electron density of the uniform electron gas [205]. This leads to the motivation of the local density approximation (LDA) with the exchange correlation potential

$$V_{\text{xc}}^{\text{LDA}}([n_{\sigma}]; \mathbf{r}) = \epsilon_{\text{xc}}^{\text{unif.}}([n_{\sigma}]; \mathbf{r}) + n(\mathbf{r}) \frac{\partial \epsilon_{\text{xc}}^{\text{unif.}}([n_{\sigma}]; \mathbf{r})}{\partial n_{\sigma}}. \quad (\text{A.16})$$

The exchange energy of the uniform electron gas can be found analytically and is proportional to $n^{1/3}$. This approach can be improved by including the gradient of the electron density leading to the so-called generalized gradient approximation (GGA) [188],

$$V_{\text{xc},\sigma}^{\text{GGA}}([n_{\sigma}]; \mathbf{r}) = \epsilon_{\text{xc}}^{\text{unif.}}([n_{\sigma}]; \mathbf{r}) + n(\mathbf{r}) \frac{\partial \epsilon_{\text{xc}}^{\text{unif.}}([n_{\sigma}]; \mathbf{r})}{\partial n_{\sigma}} - \nabla \left(n(\mathbf{r}) \frac{\partial \epsilon_{\text{xc}}^{\text{unif.}}([n_{\sigma}]; \mathbf{r})}{\partial \nabla n_{\sigma}} \right). \quad (\text{A.17})$$

According to the problem under consideration, higher approximations can be applied [72], e.g. meta-GGA [206] or hybrid-functionals [207].

B. The Mathematica package *GTPack*

The *Mathematica* group theory package *GTPack* has been developed for applications in solid state physics and photonics [Ge1]. It offers more than 150 new commands which are denoted with *GT* at the beginning, like *GTInstallGroup* for the installation of point groups. The functionality can be characterized by the following areas.

1. **Basic group theory and representation theory:** The package covers the installation of the 32 point groups or the installation of arbitrary finite groups from generators. It is possible to calculate i.e. left and right cosets, normal divisors, classes or the centre of a group. It covers basic representation theory like the calculation of character tables [108], the generation of matrices of irreducible representations [208] or direct product representations, or the computation of CLEBSCH-GORDAN coefficients [209].
2. **Electronic structure theory:** *GTPack* automatise the construction and solution of real space and \mathbf{k} -space tight binding Hamiltonians in 2- and 3-centre form [210, 211, 212] and the construction of plane wave Hamiltonians [213, 214]. It allows the group theoretical investigation of calculated band structures and allocates the states to the related irreducible representations. Furthermore *GTPack* includes modules for calculations in the framework of crystal field theory, like the construction of a crystal field Hamiltonian or the generation of STEVENS operator equivalents [112].
3. **Photonics:** With the help of the plane-wave approach, it is possible to calculate 2-dimensional photonic band structures. By applying the character projection operator, it is possible to analyse the symmetry of the electric or magnetic field and to estimate the related irreducible representation.
4. **Crystal structure, lattice and \mathbf{k} -space:** *GTPack* offers the possibility to load, save and to plot crystal structures. The stored information can be used for electronic structure calculations. *GTPack* can be applied to estimate the small groups in \mathbf{k} -space, which represent the symmetry operations at certain high-symmetry points within the BRILLOUIN zone.
5. **Auxiliary:** Within *GTPack* quaternions are introduced and the quaternion algebra is implemented. Furthermore tesseral harmonics and Cartesian spher-

ical harmonics are added. Furthermore, rotation matrices in spin space can be constructed.

Within *GTPack* symmetry elements can be represented by symbols, matrices, quaternions or EULER angles. Next to ordinary point groups, double groups can be installed for the investigation of systems with spin-orbit coupling [215].

As an example for *GTPackMathematica* notebooks related to Section 4.2 and Section 4.3 are illustrated in Figure B.1 and Figure B.2. It can be seen that all important results can be obtained after a few steps using *GTPack* commands. Starting with the qualitative discussion, it was explained in Section 4.2 that the decomposition of the 17-dimensional unperturbed ground-state belonging to the irreducible representation D^8 of the group $O(3)$ into irreducible representations of the group C_{3v} has to be investigated for the case that the symmetry is lowered from $O(3)$ to C_{3v}

```

In[1]:= Needs["GroupTheory`"]
Installation of the point group  $C_{3v}$ , and calculation of the character table.

In[1]:= c3v = GTInstallGroup["C3v"]
The standard representation has changed to  $O(3)$ 

Out[1]:= {Ee,  $C_{3z}^{-1}$ ,  $C_{3z}$ ,  $IC_{2D}$ ,  $IC_{2C}$ ,  $IC_{2Y}$ }

In[2]:= ct = {classes, chars, names} = GTCharacterTable[c3v, GOIrepNotation -> "Mulliken"]



|       | Ee | $2 C_{3z}^{-1}$ | $3 IC_{2D}$ |
|-------|----|-----------------|-------------|
| $A_1$ | 1  | 1               | 1           |
| $A_2$ | 1  | 1               | -1          |
| E     | 2  | -1              | 0           |

 $C_1 = \{Ee\}$ 

 $C_2 = \{C_{3z}^{-1}, C_{3z}\}$ 

 $C_3 = \{IC_{2D}, IC_{2C}, IC_{2Y}\}$ 

Out[2]:= {{{Ee}, { $C_{3z}^{-1}$ ,  $C_{3z}$ }, { $IC_{2D}$ ,  $IC_{2C}$ ,  $IC_{2Y}$ }}, {{1, 1, 1}, {1, 1, -1}, {2, -1, 0}}, { $A_1$ ,  $A_2$ , E}}

Characters of the angular momentum representation with  $j=8$ .

In[3]:= ac = GTAngularMomentumChars[classes, 8]

Out[3]:= {17, -1, 1}

Which irreducible representations occur?

In[4]:= GTIrep[ac, ct]

3  $A_1 \oplus 2 A_2 \oplus 6 E$ 

```

Figure B.1.: Example of *GTPack* illustrating the qualitative discussion of the crystal field splitting of the $4f_{7/2}$ four particle state ($J = 8$) of a single holmium atom on a platinum (111) surface

due to the crystal field of the platinum (111) surface. After loading *GTPack*, the point group C_{3v} can be installed by means of *GTInstallGroup*, as shown in Figure B.1. Afterwards, the character table is calculated using *GTCharacterTable*, where the irreducible representations are denoted in MULLIKEN notation [109, 110]. The characters of the elements in each of the three classes of C_{3v} for the representation D^8 can be estimated with the help of *GTAngularMomentumChars*. To calculate the decomposition of D^8 into irreducible representations of C_{3v} equation (4.1) can be used, which is implemented with the module *GTIrep*.

The quantitative discussion according to Section 4.3 can be found in Figure B.2. After loading the package and installing C_{3v} by means of *GTInstallGroup*, the crystal field Hamiltonian can be constructed with the help of *GTCrystalField*. To calculate the matrix \tilde{A} of equation (4.7), the functions $S[1, \mathbf{m}]$ of the crystal field expansion can be replaced by matrix elements of the STEVENS operator equivalents [112], which can be calculated using *GTStevensOperator*. Using crystal field parameters $B[1, \mathbf{m}]$ according to MIYAMACHI *et al.* [Ge6] the eigenvalues and eigenvectors of \tilde{A} can be calculated with the *Mathematica* command *Eigensystem*. Finally, from the eigenvectors \mathbf{a}^i , the expected value of the magnetization in z -direction $\langle J_z \rangle$ can be calculated by

$$\langle J_z \rangle = \sum_{m=1}^{2J+1} |a_m^i|^2 \langle Jm | \hat{J}_z | Jm \rangle = \sum_{m=1}^{2J+1} |a_m^i|^2 m, \quad (\text{B.1})$$

which gives the result illustrated in Figure 4.2.

```

In[0]:= Needs["GroupTheory`"]
Installation of the point group C3v.

In[1]:= c3v = GTInstallGroup["C3v"]
The standard representation has changed to O(3)

Out[1]:= {Ee, C3z1, C3z, IC2D, IC2C, IC2y}

The total angular momentum of the system is 8.

In[2]:= j = 8;
Calculation of the crystal field hamiltonian.

In[3]:= vcrtmp = GTCrystalField[c3v, 6, GOHarmonics → "Real"] /. A[l_, m_] → B[l, m] / r^l
Out[3]:= B[0, 0] S[0, 0] + B[2, 0] S[2, 0] + B[4, -3] S[4, -3] +
B[4, 0] S[4, 0] + B[6, -3] S[6, -3] + B[6, 0] S[6, 0] + B[6, 6] S[6, 6]

The tesseral harmonics can be replaced by the matrix elements of Stevens operator equivalents, calculated according to Ryabov, Applied Magnetic Resonance, Springer Vienna, 2009, 35, 481-494.

In[4]:= vcr = vcrtmp /. S[l_, m_] := GTStevensOperator[l, m, j];
The angular part of the matrix Al = (ψml, Vcr ψml) is already calculated by GTStevensOperators. The radial part is included within the coefficients Blm. Those can be taken from Miyamachi et al., Nature Publishing Group, 2013, 503, 242-246.

In[5]:= Amat =
SetAccuracy[
vcr /. {B[0, 0] → 0, B[2, 0] → -239.068 * 10^-6, B[4, 0] → 85.9023 * 10^-9,
B[4, -3] → 293.446 * 10^-9, B[6, 0] → 0.186782 * 10^-9,
B[6, -3] → -1.96786 * 10^-9, B[6, 6] → 0.630483 * 10^-9}, 20];
Now, the eigenvalues and eigenvectors of the matrix A can be calculated.

In[6]:= {ev, evec} = Eigensystem[Amat] // Chop;
If ai is an eigenvector of the matrix A, then the expectation value <Jz> can be calculated by <Jz> = ∑m=-jj |ami|2 (Szm, Jz Szm).

In[7]:= Svec[j_] := Table[S[j, m], {m, -j, j}];
Jz[j_] := DiagonalMatrix[Table[m, {m, -j, j}]];
eval = Table[vec = Abs[evec[[i]]]^2 * Svec[j]; {
Expand[vec.Jz[j].vec] /. S[l_, m_]^2 → 1, (ev[[i]] - Min[ev]) * 1000},
In[10]:= TableForm[Sort[eval, #1[[2]] < #2[[2]] &] // Chop,
TableHeadings → {None, {"<Jz> (ħ)", "E (meV)"}]}

```

<Jz> (ħ)	E (meV)
-7.9997095054350	0
7.9997095054350	0
-6.9999662944931	7.7065623650411
6.9999662944931	7.7065623650411
0	16.3255289929368
0	16.3258394803538
-4.99565857723855	24.5806183377632
4.99565857723855	24.5806183377632
-3.99213710896990	31.7345753785788
3.99213710896990	31.7345753785788
0	37.3309658650636
0	37.5195682145235
1.99073857297212	41.5090799788041
-1.99073857297212	41.5090799788041
0.99451156791772	43.9531146737451
-0.99451156791772	43.9531146737451

Figure B.2.: Example of *GTPack* illustrating the quantitative discussion of the crystal field splitting of the $4f_{7/2}$ four particle state ($J = 8$) of a single holmium atom on a platinum (111) surface

Theses and publications

- [Ge1] W. Hergert and M. Geilhufe, *Group Theory in Solid State Physics and Photonics. Problem Solving with Mathematica*, Wiley Blackwell (To be published).
- [Ge2] M. Geilhufe, S. Achilles, M. A. Köbis, M. Arnold, I. Mertig, W. Hergert, and A. Ernst, *Numerical solution of the relativistic single-site scattering problem for the Coulomb and the Mathieu potential*, arXiv:1506.07743, submitted to Journal of Physics: Condensed Matter (2015).
- [Ge3] M. Hoffmann, S. Borek, I. V. Maznichenko, S. Ostanin, G. Fischer, M. Geilhufe, W. Hergert, I. Mertig, A. Ernst, and A. Chassé, *Study of electronic and magnetic properties and related x-ray absorption spectroscopy of ultrathin Co films on BaTiO₃*, arXiv:1505.07306, submitted to Journal of Physics: Condensed Matter (2015).
- [Ge4] M. Geilhufe and W. Hergert, *GTPack - ein Mathematica package für Gruppentheorie in der Festkörperphysik*, Computer Algebra Rundbrief, **53**, 11 (2014).
- [Ge5] M. G. Vergniory, M. M. Otrokov, D. Thonig, M. Hoffmann, I. V. Maznichenko, M. Geilhufe, X. Zubizarreta, S. Ostanin, A. Marmodoro, J. Henk, W. Hergert, I. Mertig, E. V. Chulkov, and A. Ernst, *Exchange interaction and its tuning in magnetic binary chalcogenides*, Physical Review B, **89**, 165202 (2014).
- [Ge6] T. Miyamachi, T. Schuh, T. Märkl, C. Bresch, T. Balashov, A. Stöhr, C. Karlewski, S. André, M. Marthaler, M. Hoffmann, M. Geilhufe, S. Ostanin, W. Hergert, I. Mertig, G. Schön, A. Ernst, and W. Wulfhekel, *Stabilizing the magnetic moment of single holmium atoms by symmetry*, Nature, **503**, 7475, 242 (2013).
- [Ge7] T. Schuh, T. Miyamachi, S. Gerstl, M. Geilhufe, M. Hoffmann, S. Ostanin, W. Hergert, A. Ernst, and W. Wulfhekel, *Magnetic Excitations of Rare Earth Atoms and Clusters on Metallic Surfaces*, Nano Letters, **12**, 9, 4805 (2012).
- [Ge8] K. Mathwig, M. Geilhufe, F. Müller, and U. Gösele, *Bias-assisted KOH etching of macroporous silicon membranes*, Journal of Micromechanics and Microengineering, **21**, 3, 035015 (2011).

- [Ge9] M. Geilhufe, *Ab initio electronic structure of oxides: Towards a fully relativistic description and investigation of the localization failure of the local density approximation*, Master's thesis, Martin-Luther-Universität Halle-Wittenberg (2012).
- [Ge10] M. Geilhufe, *Clustermodelle elektronischer Defektstrukturen in Oxiden*, Bachelor's thesis, Martin-Luther-Universität Halle-Wittenberg (2009).

Bibliography

- [1] J. Korringa, *On the calculation of the energy of a Bloch wave in a metal*, *Physica*, **13**, 6-7, 392 (1947).
- [2] W. Kohn and N. Rostoker, *Solution of the Schrödinger Equation in Periodic Lattices with an Application to Metallic Lithium*, *Physical Review*, **94**, 1111 (1954).
- [3] H. Ebert, D. Ködderitzsch, and J. Minár, *Calculating condensed matter properties using the KKR-Green's function method - recent developments and applications*, *Reports on Progress in Physics*, **74**, 9, 096501 (2011).
- [4] R. Feder, F. Rosicky, and B. Ackermann, *Relativistic multiple scattering theory of electrons by ferromagnets*, *Zeitschrift für Physik B: Condensed Matter*, **52**, 31 (1983).
- [5] P. Strange, J. Staunton, and B. L. Gyorffy, *Relativistic spin-polarised scattering theory - solution of the single-site problem*, *Journal of Physics C: Solid State Physics*, **17**, 19, 3355 (1984).
- [6] H. Ebert, *Fully Relativistic Band Structure Calculations for Magnetic Solids - Formalism and Application*, in H. Dreyssé, ed., *Electronic Structure and Physical Properties of Solids*, Springer Berlin Heidelberg, volume 535 of *Lecture Notes in Physics*, 191–246 (2000).
- [7] B. H. Drittler, *KKR-Greensche Funktionsmethode für das volle Zellpotential*, Ph.D. thesis, Forschungszentrum Jülich (1991).
- [8] B. Drittler, M. Weinert, R. Zeller, and P. Dederichs, *Vacancy formation energies of fcc transition metals calculated by a full potential Green's function method*, *Solid State Communications*, **79**, 1, 31 (1991).
- [9] G. Dresselhaus, *Spin-Orbit Coupling Effects in Zinc Blende Structures*, *Physical Review*, **100**, 580 (1955).
- [10] R. Braunstein and E. Kane, *The valence band structure of the III–V compounds*, *Journal of Physics and Chemistry of Solids*, **23**, 10, 1423 (1962).

-
- [11] J. Henk, A. Ernst, and P. Bruno, *Spin polarization of the L-gap surface states on Au(111)*, Physical Review B, **68**, 165416 (2003).
- [12] H. Mirhosseini, J. Henk, A. Ernst, S. Ostanin, C.-T. Chiang, P. Yu, A. Winkelmann, and J. Kirschner, *Unconventional spin topology in surface alloys with Rashba-type spin splitting*, Physical Review B, **79**, 245428 (2009).
- [13] M. Z. Hasan and C. L. Kane, *Colloquium : Topological insulators*, Reviews of Modern Physics, **82**, 3045 (2010).
- [14] C. L. Kane and E. J. Mele, *Quantum Spin Hall Effect in Graphene*, Physical Review Letters, **95**, 226801 (2005).
- [15] C. L. Kane and E. J. Mele, *Z_2 Topological Order and the Quantum Spin Hall Effect*, Physical Review Letters, **95**, 146802 (2005).
- [16] B. A. Bernevig and S.-C. Zhang, *Quantum Spin Hall Effect*, Physical Review Letters, **96**, 106802 (2006).
- [17] N. Papanikolaou, R. Zeller, and P. Dederichs, *Conceptual improvements of the KKR method*, Journal of Physics: Condensed Matter, **14**, 11, 2799 (2002).
- [18] N. Papanikolaou, R. Zeller, P. H. Dederichs, and N. Stefanou, *Lattice distortion in Cu-based dilute alloys: A first-principles study by the KKR Green-function method*, Physical Review B, **55**, 4157 (1997).
- [19] M. Khalid, M. Ziese, A. Setzer, P. Esquinazi, M. Lorenz, H. Hochmuth, M. Grundmann, D. Spemann, T. Butz, G. Brauer, W. Anwand, G. Fischer, W. A. Adeagbo, W. Hergert, and A. Ernst, *Defect-induced magnetic order in pure ZnO films*, Physical Review B, **80**, 035331 (2009).
- [20] W. A. Adeagbo, G. Fischer, A. Ernst, and W. Hergert, *Magnetic effects of defect pair formation in ZnO*, Journal of Physics: Condensed Matter, **22**, 43, 436002 (2010).
- [21] A. Ernst, *Multiple-scattering theory: new developments and applications*, Habilitation thesis, Naturwissenschaftlichen Fakultät II - Chemie, Physik und Mathematik der Martin-Luther-Universität Halle-Wittenberg (2007).
- [22] M. Lüders, A. Ernst, W. M. Temmerman, Z. Szotek, and P. J. Durham, *Ab initio angle-resolved photoemission in multiple-scattering formulation*, Journal of Physics: Condensed Matter, **13**, 38, 8587 (2001).
- [23] G. Fischer, M. Däne, A. Ernst, P. Bruno, M. Lüders, Z. Szotek, W. Temmerman, and W. Hergert, *Exchange coupling in transition metal monoxides: Electronic structure calculations*, Physical Review B, **80**, 014408 (2009).

- [24] I. V. Maznichenko, A. Ernst, M. Bouhassoune, J. Henk, M. Däne, M. Lüders, P. Bruno, W. Hergert, I. Mertig, Z. Szotek, and W. M. Temmerman, *Structural phase transitions and fundamental band gaps of $Mg_xZn_{1-x}O$ alloys from first principles*, Physical Review B, **80**, 144101 (2009).
- [25] M. Lüders, A. Ernst, M. Däne, Z. Szotek, A. Svane, D. Ködderitzsch, W. Hergert, B. L. Györfy, and W. M. Temmerman, *Self-interaction correction in multiple scattering theory*, Physical Review B, **71**, 205109 (2005).
- [26] M. Däne, M. Lüders, A. Ernst, D. Ködderitzsch, W. M. Temmerman, Z. Szotek, and W. Hergert, *Self-interaction correction in multiple scattering theory: application to transition metal oxides*, Journal of Physics: Condensed Matter, **21**, 4, 045604 (2009).
- [27] P. Buczek, A. Ernst, P. Bruno, and L. M. Sandratskii, *Energies and Lifetimes of Magnons in Complex Ferromagnets: A First-Principle Study of Heusler Alloys*, Physical Review Letters, **102**, 247206 (2009).
- [28] P. Buczek, A. Ernst, and L. M. Sandratskii, *Standing Spin Waves as a Basis for the Control of Terahertz Spin Dynamics: Time Dependent Density Functional Theory Study*, Physical Review Letters, **105**, 097205 (2010).
- [29] P. Buczek, A. Ernst, and L. M. Sandratskii, *Interface Electronic Complexes and Landau Damping of Magnons in Ultrathin Magnets*, Physical Review Letters, **106**, 157204 (2011).
- [30] T. Hühne, C. Zecha, H. Ebert, P. H. Dederichs, and R. Zeller, *Full-potential spin-polarized relativistic Korringa-Kohn-Rostoker method implemented and applied to bcc Fe, fcc Co, and fcc Ni*, Physical Review B, **58**, 10236 (1998).
- [31] S. Bei der Kellen and A. J. Freeman, *Self-consistent relativistic full-potential Korringa-Kohn-Rostoker total-energy method and applications*, Physical Review B, **54**, 11187 (1996).
- [32] E. Dagotto, *Nanoscale phase separation and colossal magnetoresistance: the physics of manganites and related compounds*, volume 136, Springer Science & Business Media (2003).
- [33] Wolfram Research, Inc., *Mathematica, Version 10.0* (2014).
- [34] J. Zabloudil, R. Hammerling, L. Szunyogh, and P. Weinberger, *Electron Scattering in Solid Matter: a theoretical and computational treatise*, volume 147, Springer Science & Business Media (2006).

-
- [35] K. Strehmel, R. Weiner, and H. Podhaisky, *Numerik gewöhnlicher Differentialgleichungen: Nichtsteife, steife und differential-algebraische Gleichungen*, Vieweg+Teubner Verlag (2012).
- [36] R. A. Swainson and G. W. Drake, *A unified treatment of the non-relativistic and relativistic hydrogen atom I: The wavefunctions*, Journal of Physics A: Mathematical and General, **24**, 1, 79 (1991).
- [37] A. Rogalski, *Infrared detectors: status and trends*, Progress in Quantum Electronics, **27**, 2-3, 59 (2003).
- [38] Y. Tanaka, Z. Ren, T. Sato, K. Nakayama, S. Souma, T. Takahashi, K. Segawa, and Y. Ando, *Experimental realization of a topological crystalline insulator in SnTe*, Nature Physics, **8**, 11, 800 (2012).
- [39] T. H. Hsieh, H. Lin, J. Liu, W. Duan, A. Bansil, and L. Fu, *Topological crystalline insulators in the SnTe material class*, Nature Communications, **3**, 982 (2012).
- [40] G. Fischer, *Defektinduzierter und intrinsischer Magnetismus in Zinkoxid und Übergangsmetallfluoriden – Einfluss von Korrelationskorrekturen*, Ph.D. thesis, Martin-Luther-Universität Halle-Wittenberg (2011).
- [41] P. A. Buczek, *Spin dynamics of complex itinerant magnets*, Ph.D. thesis, Martin-Luther-Universität Halle-Wittenberg (2009).
- [42] S. Achilles, *Nichtgleichgewichts-Green-Funktionen zur Beschreibung mesoskopischer Systeme*, Ph.D. thesis, Martin-Luther-Universität Halle-Wittenberg (2012).
- [43] I. Mertig, E. Mrosan, and P. Ziesche, *Multiple scattering theory of point defects in metals: electronic properties*, Teubner-Texte zur Physik, BSB B.G. Teubner Verlagsgesellschaft (1987).
- [44] R. Zeller, P. H. Dederichs, B. Újfalussy, L. Szunyogh, and P. Weinberger, *Theory and convergence properties of the screened Korringa-Kohn-Rostoker method*, Physical Review B, **52**, 8807 (1995).
- [45] L. Szunyogh, B. Újfalussy, P. Weinberger, and J. Kollár, *Self-consistent localized KKR scheme for surfaces and interfaces*, Physical Review B, **49**, 2721 (1994).
- [46] P. Weinberger, *Electron scattering theory for ordered and disordered matter*, Clarendon Press Oxford (1990).
- [47] R. M. Dreizler and E. Engel, *Density functional theory*, Springer (2011).

- [48] G. D. Clark and N. Holonyak, *Optical Properties of Gallium Arsenide-Phosphide*, Physical Review, **156**, 913 (1967).
- [49] T. Sato and M. Imai, *Characteristics of Nitrogen-Doped GaAsP Light-Emitting Diodes*, Japanese Journal of Applied Physics, **41**, 10R, 5995 (2002).
- [50] R. Moon, G. Antypas, and L. James, *Bandgap and lattice constant of GaInAsP as a function of alloy composition*, Journal of Electronic Materials, **3**, 3, 635 (1974).
- [51] V. Popescu and A. Zunger, *Effective Band Structure of Random Alloys*, Physical Review Letters, **104**, 236403 (2010).
- [52] H. Neddermeyer, L. P. L. M. Rabou, and P. E. Mijnaerends, *Photoemission investigation of the electronic structure of $\text{Co}_{0.92}\text{Fe}_{0.08}$* , Journal of Physics F: Metal Physics, **14**, 1, 259 (1984).
- [53] N. J. Ramer and A. M. Rappe, *Virtual-crystal approximation that works: Locating a compositional phase boundary in $\text{Pb}(\text{Zr}_{1-x}\text{Ti}_x)\text{O}_3$* , Physical Review B, **62**, R743 (2000).
- [54] P. Soven, *Coherent-Potential Model of Substitutional Disordered Alloys*, Physical Review, **156**, 809 (1967).
- [55] B. Velický, S. Kirkpatrick, and H. Ehrenreich, *Single-Site Approximations in the Electronic Theory of Simple Binary Alloys*, Physical Review, **175**, 747 (1968).
- [56] B. L. Gyorffy, *Coherent-Potential Approximation for a Nonoverlapping-Muffin-Tin-Potential Model of Random Substitutional Alloys*, Physical Review B, **5**, 2382 (1972).
- [57] J. Faulkner, *The modern theory of alloys*, Progress in Materials Science, **27**, 1-2, 1 (1982).
- [58] W. Nolting and A. Ramakanth, *Quantum Theory of Magnetism*, Springer (2009).
- [59] W. Heisenberg, *Zur Theorie des Ferromagnetismus*, Zeitschrift für Physik, **49**, 9-10, 619 (1928).
- [60] A. Ernst, G. Fischer, P. Buczek, S. Ostanin, M. Däne, I. Maznichenko, A. Marmodoro, M. Hoffmann, W. Hergert, L. Bekenov, *et al.*, *First-principles design of magnetic oxides*, Ψ_k Newsletter, **112**, 16 (2012).
- [61] D. Coffey, T. M. Rice, and F. C. Zhang, *Dzyaloshinskii-Moriya interaction in the cuprates*, Physical Review B, **44**, 10112 (1991).

-
- [62] I. A. Sergienko and E. Dagotto, *Role of the Dzyaloshinskii-Moriya interaction in multiferroic perovskites*, Physical Review B, **73**, 094434 (2006).
- [63] K. Zakeri, Y. Zhang, J. Prokop, T.-H. Chuang, N. Sakr, W. X. Tang, and J. Kirschner, *Asymmetric Spin-Wave Dispersion on Fe(110): Direct Evidence of the Dzyaloshinskii-Moriya Interaction*, Physical Review Letters, **104**, 137203 (2010).
- [64] A. Liechtenstein, M. Katsnelson, V. Antropov, and V. Gubanov, *Local spin density functional approach to the theory of exchange interactions in ferromagnetic metals and alloys*, Journal of Magnetism and Magnetic Materials, **67**, 1, 65 (1987).
- [65] S. Parkin, X. Jiang, C. Kaiser, A. Panchula, K. Roche, and M. Samant, *Magnetically engineered spintronic sensors and memory*, Proceedings of the IEEE, **91**, 5, 661 (2003).
- [66] M. Svedberg, S. Majumdar, H. Huhtinen, P. Paturi, and S. Granroth, *Optimization of $Pr_{0.9}Ca_{0.1}MnO_3$ thin films and observation of coexisting spin-glass and ferromagnetic phases at low temperature*, Journal of Physics: Condensed Matter, **23**, 38, 386005 (2011).
- [67] Y. Tokura and Y. Tomioka, *Colossal magnetoresistive manganites*, Journal of Magnetism and Magnetic Materials, **200**, 1-3, 1 (1999).
- [68] C. Cardoso, R. P. Borges, T. Gasche, and M. Godinho, *Ab-initio calculations of the Ruddlesden-Popper phases $CaMnO_3$, $CaO(CaMnO_3)$ and $CaO(CaMnO_3)_2$* , Journal of Physics: Condensed Matter, **20**, 3, 035202 (2008).
- [69] V. I. Anisimov, I. S. Elfimov, M. A. Korotin, and K. Terakura, *Orbital and charge ordering in $Pr_{1-x}Ca_xMnO_3$ ($x=0$ and 0.5) from the ab initio calculations*, Physical Review B, **55**, 15494 (1997).
- [70] P. Fulde, P. Thalmeier, and G. Zwicknagl, *Strongly correlated electrons*, arXiv:0607165 (2006).
- [71] A. J. Cohen, P. Mori-Sánchez, and W. Yang, *Insights into current limitations of density functional theory*, Science, **321**, 5890, 792 (2008).
- [72] J. P. Perdew and K. Schmidt, *Jacob's ladder of density functional approximations for the exchange-correlation energy*, in *AIP Conference Proceedings*, IOP (2001), 1–20.
- [73] J. P. Perdew and A. Zunger, *Self-interaction correction to density-functional approximations for many-electron systems*, Physical Review B, **23**, 5048 (1981).

- [74] V. I. Anisimov, J. Zaanen, and O. K. Andersen, *Band theory and Mott insulators: Hubbard U instead of Stoner I* , Physical Review B, **44**, 943 (1991).
- [75] K. Wildberger, P. Lang, R. Zeller, and P. H. Dederichs, *Fermi-Dirac distribution in ab initio Green's-function calculations*, Physical Review B, **52**, 11502 (1995).
- [76] J. Staunton, B. Gyorffy, A. Pindor, G. Stocks, and H. Winter, *The disordered local moment picture of itinerant magnetism at finite temperatures*, Journal of Magnetism and Magnetic Materials, **45**, 1, 15 (1984).
- [77] A. J. Pindor, J. Staunton, G. M. Stocks, and H. Winter, *Disordered local moment state of magnetic transition metals: a self-consistent KKR CPA calculation*, Journal of Physics F: Metal Physics, **13**, 5, 979 (1983).
- [78] H. Ebert, S. Mankovsky, D. Ködderitzsch, and P. J. Kelly, *Ab-initio Calculation of the Gilbert Damping Parameter via the Linear Response Formalism*, Physical Review Letters, **107**, 066603 (2011).
- [79] H. A. Jahn and E. Teller, *Stability of polyatomic molecules in degenerate electronic states. I. Orbital degeneracy*, Proceedings of the Royal Society of London. Series A, 220–235 (1937).
- [80] K. Momma and F. Izumi, *VESTA 3 for three-dimensional visualization of crystal, volumetric and morphology data*, Journal of Applied Crystallography, **44**, 6, 1272 (2011).
- [81] D. Sánchez, J. A. Alonso, and M. J. Martínez-Lope, *Neutron-diffraction study of the Jahn-Teller transition in PrMnO_3* , Journal of the Chemical Society, Dalton Transactions, **23**, 4422 (2002).
- [82] Neetika, A. Das, I. Dhiman, A. K. Nigam, A. K. Yadav, D. Bhattacharyya, and S. S. Meena, *Transport and magnetic properties of Fe doped CaMnO_3* , Journal of Applied Physics, **112**, 12 (2012).
- [83] D. D. Koelling and B. N. Harmon, *A technique for relativistic spin-polarised calculations*, Journal of Physics C: Solid State Physics, **10**, 16, 3107 (1977).
- [84] T. Takeda, *The scalar relativistic approximation*, Zeitschrift für Physik B: Condensed Matter, **32**, 1, 43 (1978).
- [85] N. Stefanou, H. Akai, and R. Zeller, *An efficient numerical method to calculate shape truncation functions for Wigner-Seitz atomic polyhedra*, Computer Physics Communications, **60**, 2, 231 (1990).
- [86] N. Stefanou and R. Zeller, *Calculation of shape-truncation functions for Voronoi polyhedra*, Journal of Physics: Condensed Matter, **3**, 39, 7599 (1991).

-
- [87] O. K. Andersen and O. Jepsen, *Explicit, First-Principles Tight-Binding Theory*, Physical Review Letters, **53**, 2571 (1984).
- [88] J. P. Perdew, A. Ruzsinszky, G. I. Csonka, O. A. Vydrov, G. E. Scuseria, L. A. Constantin, X. Zhou, and K. Burke, *Restoring the Density-Gradient Expansion for Exchange in Solids and Surfaces*, Physical Review Letters, **100**, 136406 (2008).
- [89] M. A. Marques, M. J. Oliveira, and T. Burnus, *Libxc: A library of exchange and correlation functionals for density functional theory*, Computer Physics Communications, **183**, 10, 2272 (2012).
- [90] G. Kresse and J. Furthmüller, *Software VASP, vienna (1999)*, Physical Review B, **54**, 11, 169 (1996).
- [91] M. S. Sathyanarayana, *Combined first-principles and model Hamiltonian study of $RMnO_3$ ($R = La, Pr, Nd, Sm, Eu, Gd$)*, Ph.D. thesis, Universität Wien (2013).
- [92] W. H. Press, S. A. Teukolsky, W. T. Vetterling, and B. P. Flannery, *Numerical recipes in FORTRAN 77, Vol. 1*, New York, NY: Press Syndicate of the University of Cambridge (1992).
- [93] R. Sopracase, G. Gruener, C. Autret-Lambert, V. T. Phuoc, V. Brizé, and J. Soret, *Optical response to magnetic ordering in $PrMnO_3$: the relevance of the double exchange interaction*, arXiv:0609451 (2006).
- [94] N. N. Loshkareva, L. V. Nomerovannaya, E. V. Mostovshchikova, A. A. Makhnev, Y. P. Sukhorukov, N. I. Solin, T. I. Arbuzova, S. V. Naumov, N. V. Kostromitina, A. M. Balbashov, and L. N. Rybina, *Electronic structure and polarons in $CaMnO_{3-\delta}$ single crystals: Optical data*, Physical Review B, **70**, 224406 (2004).
- [95] T. Elovaara, H. Huhtinen, S. Majumdar, P. Paturi, T. Elovaara, H. Huhtinen, S. Majumdar, and P. Paturi, *Irreversible metamagnetic transition and magnetic memory in small-bandwidth manganite $Pr_{1-x}Ca_xMnO_3$ ($x=0-0.5$)*, Journal of Physics: Condensed Matter, **24**, 21, 216002 (2012).
- [96] Z. Jiráček, S. Krupička, Z. Šimša, M. Dlouhá, and S. Vratislav, *Neutron diffraction study of $Pr_{1-x}Ca_xMnO_3$ perovskites*, Journal of Magnetism and Magnetic Materials, **53**, 1–2, 153 (1985).
- [97] J. Tikkanen, *private communication* (2015).

- [98] L. Udvardi, L. Szunyogh, K. Palotás, and P. Weinberger, *First-principles relativistic study of spin waves in thin magnetic films*, Physical Review B, **68**, 104436 (2003).
- [99] E. O. Wollan and W. C. Koehler, *Neutron Diffraction Study of the Magnetic Properties of the Series of Perovskite-Type Compounds $[(1-x) \text{La}, x\text{Ca}]\text{MnO}_3$* , Physical Review, **100**, 545 (1955).
- [100] D. Speliotis, *Magnetic recording beyond the first 100 years*, Journal of Magnetism and Magnetic Materials, **193**, 1, 29 (1999).
- [101] P. Gambardella, S. Rusponi, M. Veronese, S. Dhési, C. Grazioli, A. Dallmeyer, I. Cabria, R. Zeller, P. Dederichs, K. Kern, *et al.*, *Giant magnetic anisotropy of single cobalt atoms and nanoparticles*, Science, **300**, 5622, 1130 (2003).
- [102] J. V. Barth, G. Costantini, and K. Kern, *Engineering atomic and molecular nanostructures at surfaces*, Nature, **437**, 7059, 671 (2005).
- [103] T. Balashov, T. Schuh, A. F. Takács, A. Ernst, S. Ostanin, J. Henk, I. Mertig, P. Bruno, T. Miyamachi, S. Suga, and W. Wulfhekel, *Magnetic Anisotropy and Magnetization Dynamics of Individual Atoms and Clusters of Fe and Co on Pt(111)*, Physical Review Letters, **102**, 257203 (2009).
- [104] C. F. Hirjibehedin, C.-Y. Lin, A. F. Otte, M. Ternes, C. P. Lutz, B. A. Jones, and A. J. Heinrich, *Large Magnetic Anisotropy of a Single Atomic Spin Embedded in a Surface Molecular Network*, Science, **317**, 5842, 1199 (2007).
- [105] S. Lebègue, A. Svane, M. Katsnelson, A. Lichtenstein, and O. Eriksson, *Triplet effects in the electronic structure of heavy rare-earth metals*, Journal of Physics: Condensed Matter, **18**, 27, 6329 (2006).
- [106] S. Stepanow, *Relativistische Quantentheorie: Für Bachelor: Mit Einführung in die Quantentheorie der Vielteilchensysteme*, Springer-Lehrbuch, Springer (2010).
- [107] J. Cornwell, *Group Theory and Electronic Energy Bands in Solids*, North-Holland Publishing Company (1969).
- [108] D. F. Holt, B. Eick, and E. A. O'Brien, *Handbook of computational group theory*, CRC Press (2005).
- [109] *Report on Notation for the Spectra of Polyatomic Molecules*, The Journal of Chemical Physics, **23**, 11, 1997 (1955).
- [110] R. S. Mulliken, *Erratum: Report on Notation for the Spectra of Polyatomic Molecules*, The Journal of Chemical Physics, **24**, 5, 1118 (1956).

-
- [111] F. Schwabl, *Quantum Mechanics*, Springer (2010).
- [112] K. W. H. Stevens, *Matrix Elements and Operator Equivalents Connected with the Magnetic Properties of Rare Earth Ions*, Proceedings of the Physical Society. Section A, **65**, 3, 209 (1952).
- [113] C. Rudowicz and C. Y. Chung, *The generalization of the extended Stevens operators to higher ranks and spins, and a systematic review of the tables of the tensor operators and their matrix elements*, Journal of Physics: Condensed Matter, **16**, 32, 5825 (2004).
- [114] I. Ryabov, *On the generation of operator equivalents and the calculation of their matrix elements*, Journal of Magnetic Resonance, **140**, 1, 141 (1999).
- [115] M. Hoffmann, *Multiple scattering theory for the description of defects in metallic alloys and oxidic systems*, Ph.D. thesis, Martin-Luther-Universität Halle-Wittenberg (2015).
- [116] E. Schrödinger, *Quantisierung als Eigenwertproblem*, Annalen der Physik, **384**, 4, 361 (1926).
- [117] E. Schrödinger, *Quantisierung als Eigenwertproblem*, Annalen der Physik, **384**, 6, 489 (1926).
- [118] E. Schrödinger, *Quantisierung als Eigenwertproblem*, Annalen der Physik, **385**, 13, 437 (1926).
- [119] E. Schrödinger, *Quantisierung als Eigenwertproblem*, Annalen der Physik, **386**, 18, 109 (1926).
- [120] P. A. Dirac, *The quantum theory of the electron*, Proceedings of the Royal Society of London. Series A, **117**, 778, 610 (1928).
- [121] P. B. Pal, *Dirac, Majorana, and Weyl fermions*, American Journal of Physics, **79**, 485 (2011).
- [122] E. Majorana, *Teoria relativistica di particelle con momento intrinseco arbitrario*, Il Nuovo Cimento (1924-1942), **9**, 10, 335 (1932).
- [123] F. Wilczek, *Majorana returns*, Nature Physics, **5**, 614 (2009).
- [124] C. Beenakker, *Search for Majorana fermions in superconductors*, arXiv:1112.1950 (2011).
- [125] X.-L. Qi and S.-C. Zhang, *Topological insulators and superconductors*, Reviews of Modern Physics, **83**, 1057 (2011).

- [126] J. Alicea, *Majorana fermions in a tunable semiconductor device*, Physical Review B, **81**, 125318 (2010).
- [127] M. Reed and B. Simon, *Methods of modern mathematical physics. I: Functional analysis*, volume 2, Academic press New York (1980).
- [128] G. Teschl, *Mathematical methods in quantum mechanics: with applications to Schrödinger operators*, volume 99, American Mathematical Soc. (2009).
- [129] B. Thaller, *The Dirac Equation*, Texts and monographs in physics, Springer (2010).
- [130] P. Strange, *Relativistic quantum mechanics: with applications in condensed matter and atomic physics*, Cambridge University Press (1998).
- [131] A. H. MacDonald and S. H. Vosko, *A relativistic density functional formalism*, Journal of Physics C: Solid State Physics, **12**, 15, 2977 (1979).
- [132] M. Ramana and A. Rajagopal, *Relativistic spin-polarised electron gas*, Journal of Physics C: Solid State Physics, **12**, 22, L845 (1979).
- [133] E. Tamura, *Relativistic single-site Green function for general potentials*, Physical Review B, **45**, 7, 3271 (1992).
- [134] A. Crépieux and P. Bruno, *Relativistic corrections in magnetic systems*, Physical Review B, **64**, 094434 (2001).
- [135] W. M. Temmerman, B. L. Gyorffy, and G. M. Stocks, *The atomic sphere approximation to the KKR-CPA: electronic structure of paramagnetic Cu_cNi_{1-c} alloys*, Journal of Physics F: Metal Physics, **8**, 12, 2461 (1978).
- [136] O. K. Andersen, *Linear methods in band theory*, Physical Review B, **12**, 3060 (1975).
- [137] M. Ogura, *Electric Field Gradients Calculated by the Full Potential KKR Green's Function Method*, Ph.D. thesis, Department of Physics, Graduate School of Science, Osaka University (2004).
- [138] E. W. Weisstein, *Wigner 3j-Symbol.*, From MathWorld - A Wolfram Web Resource. <http://mathworld.wolfram.com/Wigner3j-Symbol.html> (2015).
- [139] V. Lebedev, *Quadratures on a sphere*, USSR Computational Mathematics and Mathematical Physics, **16**, 2, 10 (1976).
- [140] D. Zaharioudakis, *Calculation of shape-truncation functions for cubic cells*, Computer Physics Communications, **130**, 1-2, 22 (2000).

-
- [141] D. Zaharioudakis, *Calculation of shape-truncation functions for hexagonal cells*, Computer Physics Communications, **140**, 3, 323 (2001).
- [142] L. M. Sandratskii, *Noncollinear magnetism in itinerant-electron systems: Theory and applications*, Advances in Physics, **47**, 1, 91 (1998).
- [143] M. Uhl, L. Sandratskii, and J. Kübler, *Electronic and magnetic states of γ -Fe*, Journal of Magnetism and Magnetic Materials, **103**, 3, 314 (1992).
- [144] B. Y. Yavorsky, P. Zahn, and I. Mertig, *Ab initio study of the magnetic structure of fcc Fe grown on a Cu(001) substrate*, Physical Review B, **70**, 014413 (2004).
- [145] S. Lounis, P. Mavropoulos, P. H. Dederichs, and S. Blügel, *Noncollinear Korringa-Kohn-Rostoker Green function method: Application to 3d nanostructures on Ni(001)*, Physical Review B, **72**, 224437 (2005).
- [146] P. M. Morse and H. Feshbach, *Methods of theoretical physics*, McGraw-Hill (1953).
- [147] J. S. Faulkner and G. M. Stocks, *Calculating properties with the coherent-potential approximation*, Physical Review B, **21**, 3222 (1980).
- [148] B. Drittler, M. Weinert, R. Zeller, and P. H. Dederichs, *First-principles calculation of impurity-solution energies in Cu and Ni*, Physical Review B, **39**, 930 (1989).
- [149] W. Kaballo, *Grundkurs Funktionalanalysis*, Springer DE (2011).
- [150] A. Nickel, *Fixpunktsatz von Banach und Anwendungen*, Bachelor's thesis, Universität Bielefeld (2010).
- [151] W. S. Wladimirow, *Gleichungen der mathematischen Physik*, VEB Deutscher Verlag der Wissenschaften (1972).
- [152] R. Zeller, *An elementary derivation of Lloyd's formula valid for full-potential multiple-scattering theory*, Journal of Physics: Condensed Matter, **16**, 36, 6453 (2004).
- [153] M. Ogura and H. Akai, *The full potential Korringa-Kohn-Rostoker method and its application in electric field gradient calculations*, Journal of Physics: Condensed Matter, **17**, 37, 5741 (2005).
- [154] R. Zeller, *Large scale supercell calculations for forces around substitutional defects in NiTi*, Physica Status Solidi (b), **251**, 10, 2048 (2014).

-
- [155] Å. Björck, *Numerical Methods in Matrix Computations*, volume 59 of *Texts in Applied Mathematics*, Springer International Publishing (2015).
- [156] J. H. Wilkinson, *Rounding errors in algebraic processes*, Courier Corporation (1994).
- [157] H. J. Oberle, *Numerik gewöhnlicher Differentialgleichungen (WS 2008/2009)*.
- [158] L. F. Shampine and M. W. Reichelt, *The MATLAB ode suite*, SIAM Journal on Scientific Computing, **18**, 1, 1 (1997).
- [159] R. Ashino, M. Nagase, and R. Vaillancourt, *Behind and beyond the MATLAB ODE suite*, Computers & Mathematics with Applications, **40**, 4, 491 (2000).
- [160] J. R. Dormand and P. J. Prince, *A family of embedded Runge-Kutta formulae*, Journal of Computational and Applied Mathematics, **6**, 1, 19 (1980).
- [161] P. Bogacki and L. F. Shampine, *A 3 (2) pair of Runge-Kutta formulas*, Applied Mathematics Letters, **2**, 4, 321 (1989).
- [162] R. Bulirsch and J. Stoer, *Numerical treatment of ordinary differential equations by extrapolation methods*, Numerische Mathematik, **8**, 1, 1 (1966).
- [163] R. Fiedler, *Extrapolationsmethoden mit Ordnungs- und Schrittweitensteuerung*, Master's thesis, Martin-Luther-Universität Halle-Wittenberg (2010).
- [164] E. U. Condon and G. H. Shortley, *The theory of atomic spectra*, Cambridge University Press (1951).
- [165] P. Strange, H. Ebert, J. B. Staunton, and B. L. Gyorffy, *A relativistic spin-polarised multiple-scattering theory, with applications to the calculation of the electronic structure of condensed matter*, Journal of Physics: Condensed Matter, **1**, 18, 2959 (1989).
- [166] P. Lloyd, *Wave propagation through an assembly of spheres: II. The density of single-particle eigenstates*, Proceedings of the Physical Society, **90**, 1, 207 (1967).
- [167] P. Lloyd and P. Smith, *Multiple scattering theory in condensed materials*, Advances in Physics, **21**, 89, 69 (1972).
- [168] K. Gunkel, *Gesamtenergieberechnung mit Lloydscher Formel für den Idealkristall*, Ph.D. thesis, Rheinisch-Westfälisch Technische Hochschule Aachen (1993).

- [169] E. Arola, *The Relativistic KKR-CPA Method: A Study of Electronic Structures of $Cu_{75}Au_{25}$, $Au_{70}Pd_{30}$ and $Cu_{75}Pt_{25}$ Disordered Alloys*, Ph.D. thesis, Tampere University of Technology (1991).
- [170] J. Staunton, P. Strange, B. Gyorffy, M. Matsumoto, J. Poulter, H. Ebert, and N. Archibald, *Theory of Magnetocrystalline Anisotropy*, in S. Wilson, I. P. Grant, and B. L. Gyorffy, eds., *The Effects of Relativity in Atoms, Molecules, and the Solid State*, Springer, 295–317 (1991).
- [171] W. Greiner, *Theoretische Physik 06. Relativistische Quantenmechanik. Wellengleichungen: Ein Lehr- und Übungsbuch*, Wissenschaftlicher Verlag Harri Deutsch GmbH (2002).
- [172] M. Rose, *Relativistic electron theory*, Wiley (1961).
- [173] R. A. Swainson and G. W. Drake, *A unified treatment of the non-relativistic and relativistic hydrogen atom II: the Green functions*, Journal of Physics A: Mathematical and General, **24**, 1, 95 (1991).
- [174] R. A. Swainson and G. W. F. Drake, *A unified treatment of the non-relativistic and relativistic hydrogen atom: III. The reduced Green functions*, Journal of Physics A: Mathematical and General, **24**, 8, 1801 (1991).
- [175] P. Rennert, A. Chassé, and W. Hergert, *Einführung in die Quantenphysik: Experimentelle und theoretische Grundlagen mit Aufgaben, Lösungen und Mathematica-Notebooks*, Springer-Verlag (2013).
- [176] E. W. Weisstein, *Whittaker function*, From MathWorld - A Wolfram Web Resource. <http://mathworld.wolfram.com/WhittakerFunction.html> (2014).
- [177] F. W. J. Olver, *and National Institute of Standards and Technology (U.S.), NIST Handbook of Mathematical Functions*, Cambridge University Press (2010).
- [178] G. Söderlind, L. Jay, and M. Calvo, *Stiffness 1952-2012: Sixty years in search of a definition*, BIT Numerical Mathematics, 1–28 (2014).
- [179] C.-Y. Yeh, A.-B. Chen, D. M. Nicholson, and W. H. Butler, *Full-potential Korringa-Kohn-Rostoker band theory applied to the Mathieu potential*, Physical Review B, **42**, 10976 (1990).
- [180] S. Achilles, *private communication* (2015).
- [181] D. A. Varshalovich, A. N. Moskalev, and V. K. Khersonskii, *Quantum theory of angular momentum*, World Scientific (1988).

- [182] H.-R. Schwarz and N. Köckler, *Numerische Mathematik*, Springer-Verlag (2011).
- [183] H. Zogg, C. Maissen, J. Masek, T. Hoshino, S. Blunier, and A. N. Tiwari, *Photovoltaic infrared sensor arrays in monolithic lead chalcogenides on silicon*, *Semiconductor Science and Technology*, **6**, 12C, C36 (1991).
- [184] A. V. Dmitriev and I. P. Zvyagin, *Current trends in the physics of thermoelectric materials*, *Physics-Uspekhi*, **53**, 8, 789 (2010).
- [185] G. J. Snyder and E. S. Toberer, *Complex thermoelectric materials*, *Nature Materials*, **7**, 2, 105 (2008).
- [186] S. K. Nayak, *private communication* (2014).
- [187] P. Bauer Pereira, I. Sergueev, S. Gorsse, J. Dadda, E. Müller, and R. P. Hermann, *Lattice dynamics and structure of GeTe, SnTe and PbTe*, *Physica Status Solidi (b)*, **250**, 7, 1300 (2013).
- [188] J. P. Perdew, K. Burke, and M. Ernzerhof, *Generalized Gradient Approximation Made Simple*, *Physical Review Letters*, **77**, 3865 (1996).
- [189] G. M. T. Foley and D. N. Langenberg, *Electronic structure of PbTe near the band gap*, *Physical Review B*, **15**, 4850 (1977).
- [190] W. Scanlon, *Recent advances in the optical and electronic properties of PbS, PbSe, PbTe and their alloys*, *Journal of Physics and Chemistry of Solids*, **8**, 0, 423 (1959).
- [191] R. Tsu, W. E. Howard, and L. Esaki, *Optical and Electrical Properties and Band Structure of GeTe and SnTe*, *Physical Review*, **172**, 779 (1968).
- [192] E. W. Weisstein, *Lorentzian function*, From MathWorld - A Wolfram Web Resource. <http://mathworld.wolfram.com/LorentzianFunction.html> (2014).
- [193] L. Vegard, *Die Konstitution der Mischkristalle und die Raumfüllung der Atome*, *Zeitschrift für Physik*, **5**, 1, 17 (1921).
- [194] J. Dimmock, I. Melngailis, and A. Strauss, *Band structure and laser action in $Pb_xSn_{1-x}Te$* , *Physical Review Letters*, **16**, 26, 1193 (1966).
- [195] J. R. Dixon and R. F. Bis, *Band Inversion and the Electrical Properties of $Pb_xSn_{1-x}Te$* , *Physical Review*, **176**, 942 (1968).

- [196] M. Hoffmann, A. Marmodoro, E. Nurmi, K. Kokko, L. Vitos, A. Ernst, and W. Hergert, *Elastic anomalies and long/short-range ordering effects: A first-principles investigation of the $\text{Ag}_c\text{Pd}_{1-c}$ solid solution*, *Physical Review B*, **86**, 094106 (2012).
- [197] M. Born and R. Oppenheimer, *Zur Quantentheorie der Molekeln*, *Annalen der Physik*, **389**, 20, 457 (1927).
- [198] P. Hohenberg and W. Kohn, *Inhomogeneous Electron Gas*, *Physical Review*, **136**, B864 (1964).
- [199] E. Runge and E. K. U. Gross, *Density-Functional Theory for Time-Dependent Systems*, *Physical Review Letters*, **52**, 997 (1984).
- [200] G. Vignale and M. Rasolt, *Density-functional theory in strong magnetic fields*, *Physical Review Letters*, **59**, 2360 (1987).
- [201] E. Engel, *Chapter 10 Relativistic density functional theory: Foundations and basic formalism*, in P. Schwerdtfeger, ed., *Relativistic Electronic Structure Theory*, Elsevier, volume 11 of *Theoretical and Computational Chemistry*, 523–621 (2002).
- [202] A. K. Rajagopal, *Time-dependent functional theory of coupled electron and electromagnetic fields in condensed-matter systems*, *Physical Review A*, **50**, 3759 (1994).
- [203] W. Kohn and L. J. Sham, *Self-Consistent Equations Including Exchange and Correlation Effects*, *Physical Review*, **140**, A1133 (1965).
- [204] D. M. Ceperley and B. J. Alder, *Ground State of the Electron Gas by a Stochastic Method*, *Physical Review Letters*, **45**, 566 (1980).
- [205] J. P. Perdew and Y. Wang, *Accurate and simple analytic representation of the electron-gas correlation energy*, *Physical Review B*, **45**, 13244 (1992).
- [206] J. P. Perdew, S. Kurth, A. c. v. Zupan, and P. Blaha, *Accurate Density Functional with Correct Formal Properties: A Step Beyond the Generalized Gradient Approximation*, *Physical Review Letters*, **82**, 2544 (1999).
- [207] I. C. Gerber and J. G. Ángyán, *Hybrid functional with separated range*, *Chemical Physics Letters*, **415**, 1–3, 100 (2005).
- [208] S. Flodmark and E. Blokker, *A computer program for calculation of irreducible representations of finite groups*, *International Journal of Quantum Chemistry*, **1**, S1, 703 (1967).

-
- [209] P. M. Vandenbroek and J. F. Cornwell, *Clebsch-Gordan Coefficients of Symmetry Groups*, Physica Status Solidi (b), **90**, 1, 211 (1978).
- [210] A. V. Podolskiy and P. Vogl, *Compact expression for the angular dependence of tight-binding Hamiltonian matrix elements*, Physical Review B, **69**, 233101 (2004).
- [211] R. F. Egorov, B. I. Reser, and V. P. Shirokovskii, *Consistent Treatment of Symmetry in the Tight Binding Approximation*, Physica Status Solidi (b), **26**, 391 (1968).
- [212] J. C. Slater and G. F. Koster, *Simplified LCAO Method for the Periodic Potential Problem*, Physical Review, **94**, 1498 (1954).
- [213] D. Fritsch, H. Schmidt, and M. Grundmann, *Band-structure pseudopotential calculation of zinc-blende and wurtzite AlN, GaN, and InN*, Physical Review B, **67**, 235205 (2003).
- [214] R. Dirl, K. Payer, and B. L. Davies, *Symmetrized plane waves .1. Symmorphic space groups*, Computer Physics Communications, **98**, 1-2, 52 (1996), v1414
Times Cited:2 Cited References Count:26.
- [215] T. Damhus, *Double groups as symmetry groups for spin-orbit coupling Hamiltonians*, MATCH Communications in Mathematical and in Computer Chemistry (1984).

Acknowledgements

At this point I would like to acknowledge the support of several collaborators and colleagues which played an important role during the past years.

First and foremost, I would like to thank DR. ARTHUR ERNST for the supervision of this thesis. Under his guidance I had the possibility to learn a lot. I am especially grateful for his support in my interest to participate in various conferences and graduate workshops.

I would also like to acknowledge the help of PROF. WOLFRAM HERGERT who has supported and supervised my scientific work for many years. Within this time he provided me with a lot of insights and knowledge about physics. Moreover, I am very grateful for learning group theoretical methods for the application in theoretical physics from him.

Special thanks go to DR. STEVEN ACHILLES for countless discussions about the relativistic KKR method and his collaboration within our project about the underlying numerics. Furthermore, I would like to thank him and DR. GUNTRAM FISCHER for giving helpful remarks for this thesis.

I would also like to thank DR. SANJEEV KUMAR NAYAK for our collaboration in the $\text{Pb}_x\text{Sn}_{1-x}\text{Te}$ project. Moreover, I would like to thank him and all colleagues of our research group, especially, MARTIN HOFFMANN, DR. WAHEED ADEAGBO, DR. PAWEŁ BUCZEK and STEFAN THOMAS for their help and support in several scientific or computational problems.

Additionally, I would like to take the opportunity to thank my colleagues from the Turku university. I very much appreciate the hospitality of PROF. KALEVI KOKKO who provided a quiet and inspiring working atmosphere during several visits. I am also grateful for the collaboration with PROF. PETRIINA PATURI and JUSSI TIKKANEN in the project regarding the magnetic structure of $\text{Pr}_{1-x}\text{Ca}_x\text{MnO}_3$.

I very much acknowledge the collaboration with PROF. MARTIN ARNOLD and MARKUS ARTHUR KÖBIS from the research group numerical mathematics and their help concerning the numerical solution of the relativistic single-site scattering problem. In this context, I also want thank DR. RUDOLF ZELLER for his invitation to Forschungszentrum Jülich and the comprehensive discussions about the relativistic KKR method. Also, I want to thank PROF. WULF WULFHEKEL from the KIT Karlsruhe for the ongoing collaboration on the investigation of single rare-earth atoms on highly conducting surfaces. For her help concerning all organizational problems and her continuous friendly and helpful support I would like to thank INA GOFFIN.

Last but not least, I would like to thank my friends and fellow students CHRISTIAN HERSCHBACH and KILIAN STUMPF for their steady support.

Eidesstattliche Erklärung / Declaration under oath

Ich erkläre an Eides statt, dass ich die Arbeit selbstständig und ohne fremde Hilfe verfasst, keine anderen als die von mir angegebenen Quellen und Hilfsmittel benutzt und die den benutzten Werken wörtlich oder inhaltlich entnommenen Stellen als solche kenntlich gemacht habe. Ich erkläre weiterhin, die Angaben wahrheitsgemäß gemacht und weder diese noch eine andere Dissertation an einer anderen wissenschaftlichen Einrichtung vorgelegt zu haben.

I declare under penalty of perjury that this thesis is my own work entirely and has been written without any help from other people. I used only the sources mentioned and included all the citations correctly both in word or content. Neither this thesis nor any other thesis has been submitted to another scientific institution.

Matthias Geilhufe
Halle, July 28, 2015

Curriculum vitae

Personal Details

Name **Matthias Geilhufe**
Date of birth **15/11/1986**
Place of birth **Halle (Saale), Germany**

Education

2012–Present **PhD Student**, *Max Planck Institute of Microstructure Physics*, Halle (Saale)

Thesis *Complex structures, disorder and low dimensionality - Treatment of oxides and semiconductors by a relativistic KKR Green function method*

Supervisor PD. Dr. Arthur Ernst

2009–2012 **M. Sc.**, *Martin Luther University Halle-Wittenberg*, Halle (Saale)

Thesis *Ab initio electronic structure of oxides: Towards a fully relativistic description and investigation of the localisation failure of the local density approximation*

Supervisor Prof. Dr. Wolfram Hergert

2006–2009 **B. Sc.**, *Martin Luther University Halle-Wittenberg*, Halle (Saale)

Thesis *Investigation of the electronic structure of vacancies in oxides*

Supervisor Prof. Dr. Wolfram Hergert

2000–2006 **Grammar School**, *Südstadt-Gymnasium*, Halle (Saale)

1998–2000 **Secondary School**, *Sekundarschule Adam Ries*, Halle (Saale)

1993–1998 **Elementary School**, *Grundschule Bertold Brecht*, Halle (Saale)

Matthias Geilhufe
Halle, July 28, 2015